Advanced nanomechanical test techniques

Ben D. Beake[1], Adrian J. Harris[1] and Tomasz W. Liskiewicz[2]

1 Micro Materials Ltd., Willow House, Ellice Way, Yale Business Village, Wrexham, LL13 7YL, UK
2 Institute of Engineering Thermofluids, Surfaces & Interfaces, School of Mechanical Engineering, University of Leeds, Woodhouse Lane, Leeds, LS2 9JT, UK

Contents

1. Introduction
2. Nanoindentation
2.1 Contact mechanics theory
2.2 Practical considerations
2.2.1 Reference materials for calibration
2.2.2 Choice of loading ramp
2.2.3 Thermal drift
2.2.4 The international standard for depth-sensing indentation - ISO14577
2.2.5 Surface roughness
2.2.6 Determination of frame compliance
2.2.7 Determination of area function
2.2.8 Zero point correction
2.3 Indentation size effects
2.4 Choice of indenter geometry and stress-strain curves
2.5 Plasticity index and H/E
2.6 Hardness and elastic modulus of coatings
2.7 Ultra-hard coatings
2.8 Depth profiling
2.9 Mapping and positioning
2.10 Fracture toughness
2.11 Micro-pillar compression, micro-cantilever bending and push-out tests
3. Nanotribology: nano-scratch and nano-wear
3.1 Critical load sensitivity to intrinsic and extrinsic factors
3.2 Topography-progressive load scratch-topography multi-pass scratch tests
3.3 Influence of probe radius and geometry
3.4 Contact pressure
3.5 Influence of film stress and thickness
3.6 Repetitive nano-wear
3.7 Surface roughness
3.8 Friction
4. Nano-fretting
5. Nano-impact
5.1 Single impact
5.2 Repetitive impact
6. Environmental considerations
6.1 Influence of moisture and electrochemical potential on nanoindentation behaviour
6.2 Nano-scratch and nano-impact testing in liquid
6.3 Measuring high temperature mechanical properties by nanoindentation
6.4 Non-ambient nano-scratch and nano-impact testing
6.4.1 High temperature nano-scratch and friction testing
6.4.2 Sub-ambient temperature nanoindentation, nano-scratch and nano-wear testing
6.4.3 High temperature nano-impact testing
7. Summary and Outlook
8. References

1. Introduction

For many years hardness of bulk materials and thick coatings has been determined by optical analysis of indentation marks. The development of thin coatings deposited by techniques such as PVD and CVD, to improve wear resistance, led to the requirement to measure their properties at smaller scale. Initially such coatings were typically relatively thick (e.g. ~10 μm) and microhardness measurements could be performed to determine their hardness. However, as the thickness of the films reduced the reliable determination of their hardness by conventional optical means became impossible. Depth-sensing indentation (DSI) instruments have been developed to address this need and have become increasingly popular. The test technique is also called instrumented indentation testing (IIT) or nanoindentation and has progressed sufficiently for standardisation to be required with the first international standard for depth sensing indentation being released in 2002 and is currently in revision [1]. Provided instruments are well-calibrated the data from nanoindentation tests are routinely analysed by well-established contact mechanics treatments to provide the reduced elastic modulus and the hardness (or more strictly the mean contact pressure) of the test sample [2-3]. Conversion between nanoindentation hardness and Vickers hardness requires a little care. In addition to knowledge of the indenter geometry the actual contact areas used in the two definitions of hardness are slightly different necessitating the need for a geometric correction factor.

Over the last 25 years commercial nanoindentation test instruments (also called nanoindenters) have improved their resolution, their calibrations and their ability to very precisely position where the indentations are made to obtain highly localised and accurate mechanical property information. Additionally, they have expanded the range of test techniques beyond simple nanoindentation, with several including some capability for nanotribological measurements (e.g. nano-scratch and nano-wear testing) which has consequently greatly expanded their range of applications. There are a range of commercial nanoindenter designs, including electrostatic or capacitive actuation, and vertical or horizontal loading configurations. The design of one popular commercial test instrument, the NanoTest from Micro Materials, combines electrostatic actuation with horizontal loading and an open test platform that has enabled its further development into a true multifunctional nanomechanical/nanotribological test instrument where tests can be performed with a range of contact geometries (figure 1) and environmental conditions (figure 2 illustrates the temperature and strain rate test envelope) [4]. The various tests provide complementary information and the data obtained can often more usefully map onto the actual conditions that the materials experience in use. It is becoming possible to move beyond basic characterisation to the development of increasingly accurate prediction of the surface behaviour.

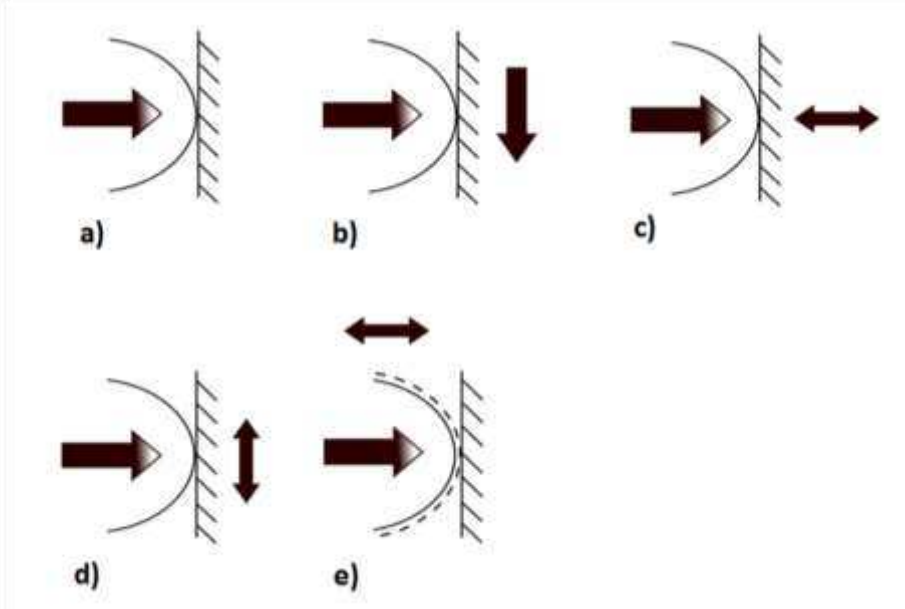

Figure 1: Range of nanomechanical testing capability in a commercial instrument (NanoTest)

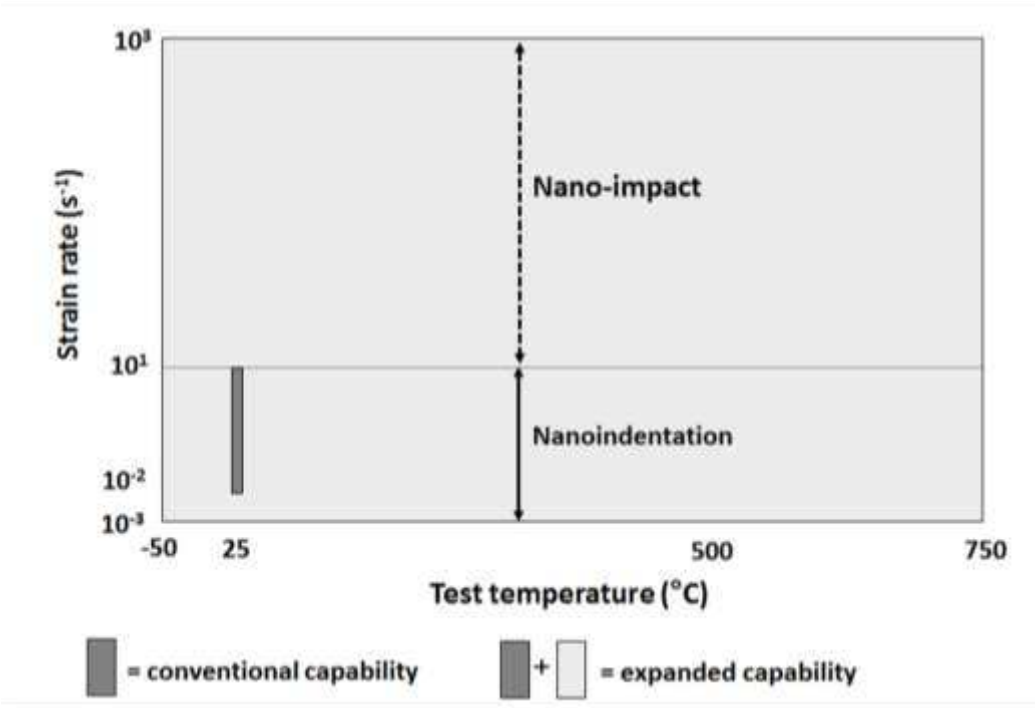

Figure 2: Temperature and strain rate test capability in a commercial instrument (NanoTest)

2. Nanoindentation

2.1 Contact mechanics theory

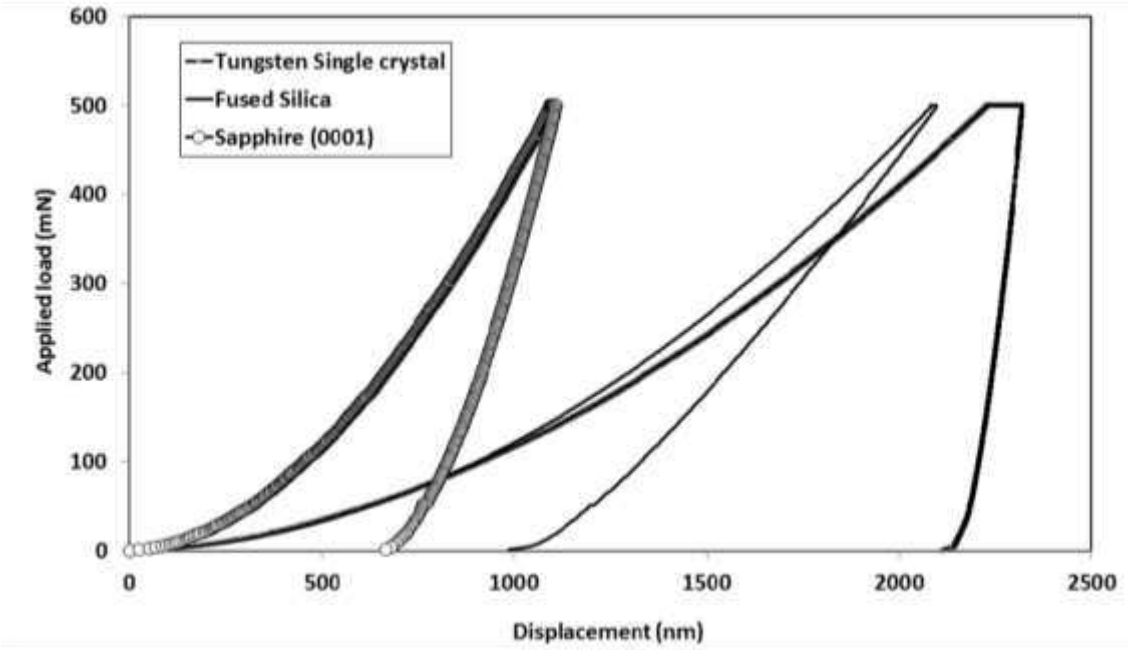

Figure 3: Nanoindentation curves on fused silica, single crystal tungsten and sapphire (0001)

Illustrative nanoindentation curves on fused silica, single crystal tungsten and sapphire (0001) with a sharp pyramidal Berkovich diamond indenter are shown in figure 3. For a given indenter geometry the load-displacement curve recorded in a nanoindentation test can be thought of a "fingerprint" for a material as it contains information about the elastic and plastic properties of the sample under test. The slope of the unloading curve at any point is called the contact stiffness. In this analysis, the reduced modulus, E_r, is calculated from the stiffness at the onset of the unloading S and the projected area of contact between the probe and the material A_c as

$$E_r = \frac{\sqrt{\pi}}{2\beta} \cdot \frac{S}{\sqrt{A_c}} \qquad (1)$$

where β is the correction factor for the shape of the indenter. There is some on-going debate over the exact value though β is commonly taken as 1.034 for the Berkovich indenter geometry. The reduced indentation modulus, E_r, is directly determined in a nanoindentation test (also referred to as E'). However, the plane strain modulus, $E^* = E/(1-\nu^2)$, can also be quoted (e.g. in ISO14577 [1]) and when reporting nanoindentation data it is therefore necessary to specify clearly which modulus is being reported (E_r, E^* or E). Conversion of the directly measured reduced modulus to the Elastic (Young's) modulus of the sample requires that its Poisson's ratio be known or can be reliably estimated. As elastic displacements occur both in the specimen and in the indenter (the indenter is not completely rigid), the elastic modulus of the sample is calculated from E_r using

$$\frac{1}{E_r} = \frac{1-\nu^2}{E} + \frac{1-\nu_i^2}{E_i} \qquad (2)$$

where E and E_i, ν and ν_i are the elastic modulus and the Poisson ratio of the tested material and indenter, respectively. For diamond indenters, E_i and ν_i are 1141 GPa and 0.07, respectively. When a diamond indenter is used (i) on fused silica with $\nu = 0.17$, a reduced modulus of 69.6 GPa gives E = 72 GPa (ii) for ceramics and hard coatings ν is typically 0.2-0.25. For sapphire with $\nu = 0.235$, an E_r of 314 GPa is equivalent to E = 410 GPa. (iii) For tungsten with Poisson ratio = 0.28, E_r = 320 GPa converts to E = 409 GPa. The mean pressure or hardness (H) can be calculated as

$$H = \frac{P}{A_c} \qquad (3)$$

where P is the applied load. Nanoindentation hardness is defined as the load divided by the projected contact area. However, in the definition of Vickers hardness the actual rather than projected area is used resulting in a geometric scaling factor of 0.927 [5] and after correction for units a final relation of

$$HV = 0.094545\ H_{IT} \qquad (4)$$

where HV = Vickers hardness and H_{IT} is the depth-sensing indentation hardness.

2.2 Practical considerations

2.2.1 Reference materials for calibration

Fused silica has proved the most popular material for calibrating nanoindentation instruments and the test probes (indenters) they use. It is inexpensive, highly polished, mechanically homogeneous and has relatively little time-dependent behaviour due to its high melting point (~1650 °C). Typically its mechanical properties are quoted as H ~9.2 GPa, E = (72 +/- 1) GPa and Poisson ratio = 0.17. In practice actual values may vary slightly from different suppliers. For example, a recent certified reference sample obtained from the UK National Physical Laboratory was supplied with E = 73 GPa and Poisson ratio = 0.16.

Despite being a default a reference sample popularly used for both area function and frame compliance calibration, its mechanical behaviour in indentation is actually complex. Kermouche and co-workers noted that whilst normal glasses exhibit little densification on indentation anomalous glasses exhibit large densification and different fracture behaviour, and fused silica, which is the most anomalous silicate glass of industrial interest, can achieve 20% densification after indentation [6]. Its behaviour is more complex than is generally supposed since (i) its near surface properties may be reduced by hydration (ii) it is an anomalous glass whose elastic modulus increases with temperature [7] (iii) contact area determination can be influenced by radial dilation due to its high H/E [8] (iv) densification occurs under the indenter (v) cracking occurs at high load, dependent on the acuity of the indenter [9] (v) by having a very high H/E ratio its sensitivity to small errors in frame stiffness was rather low.

Calibrations of test instruments can be more robust if supplemented by measurements into a metallic reference material with lower H/E such as Aluminium or Tungsten. ISO145577 recommends the use of two materials of dissimilar E. An example of a successful calibration is shown below [10].

Table 1 multiple reference sample calibration (after [10])

Reference sample	E Experimental (GPa)	E Expected (GPa)
Fused Silica	71.8 ± 0.4	72
Tungsten	417.5 ± 4.6	410
Steel	220.5 ± 1.5	220

2.2.2 Choice of loading ramp

The standard contact mechanics treatment of the unloading curve data used to determine H and E is essentially based on elastic contact mechanics with no provision for time-dependency. It is important that time-dependent behaviour does not influence the accuracy of the elastic modulus so the experimental conditions (load history) should be modified accordingly. Chudoba and Richter have detailed the problems that can occur when the holding period at peak load is too short [11]. For soft metals, the combination of slow loading, a long hold at peak load and a fast unload ensures that the contribution of non-elastic behaviour during unloading is minimized, or negligible in most cases. An alternative approach currently beginning to find favour is to develop more complex analytical treatments that can handle the time-dependency.

2.2.3 Instrumental (thermal) drift

Since nanoindenters measure very small displacements high accuracy is required, i.e. data should not be influenced by any thermal or mechanical drift during the test duration. For less thermally stable instrument designs, a practical solution has been to indent as fast as possible, although as mentioned above this fast loading and low hold time at peak load may result in some anelastic deformation during unloading for highly creeping materials. For all instrument designs it is important that when holding for a thermal drift correction (typically on the surface under the contact load immediately prior to the loading ramp and/or at 90% unloading) that deformation due to creep or creep recovery is not erroneously thought to be due to thermal drift. An excellent example of this is the continuing extensive creep recovery that occurs on all polymeric materials. For highly stable nanoindenters this can be x100 greater than the real thermal drift so mistakenly correcting data for it introduces error. Similarly if the sample is very soft (e.g. solder) then the initial load for thermal drift should not be used as deformation during this period is likely to be dominated by creep rather than drift.

2.2.4 The international standard for depth-sensing indentation - ISO 14577 parts 1-4

The International Organisation for Standardisation (ISO) has released an international standard ISO 14577 parts 1-3 entitled “Metallic materials – Instrumented indentation test for hardness and materials parameters” in 2002, with Part 1 Test method, Part 2 Verification and calibration of machines, Part 3 Calibration of reference blocks. The recent extension to the ISO indentation standard (ISO14577 Part 4 - Test Method for metallic and non-metallic coatings) is also concerned with experimental best practice for the determination of accurate hardness and elastic modulus of coatings independently of the influence of substrate. This is discussed further below.

Continuing time-dependent deformation during unloading affects the accuracy of the analysis of the unloading curve which assumes elastic behaviour. In general a reliable strategy for minimising/eliminating any influence of time-dependency is a combination of (1) slow loading (2) suitable hold period at peak load (3) fast unloading. This is illustrated schematically in figure 4 (a). During the hold period the creep rate decreases sufficiently that the continuing anelastic deformation during the faster unload is minimal greatly increasing the accuracy of the elastic assumption in the unloading analysis. Figure 4 (b) shows continuing creep during 30s hold at peak load at 500 mN on single crystal Al and figure 4 (c) shows nanoindentation curves from 100-500 mN on single crystal Al.

4(a)

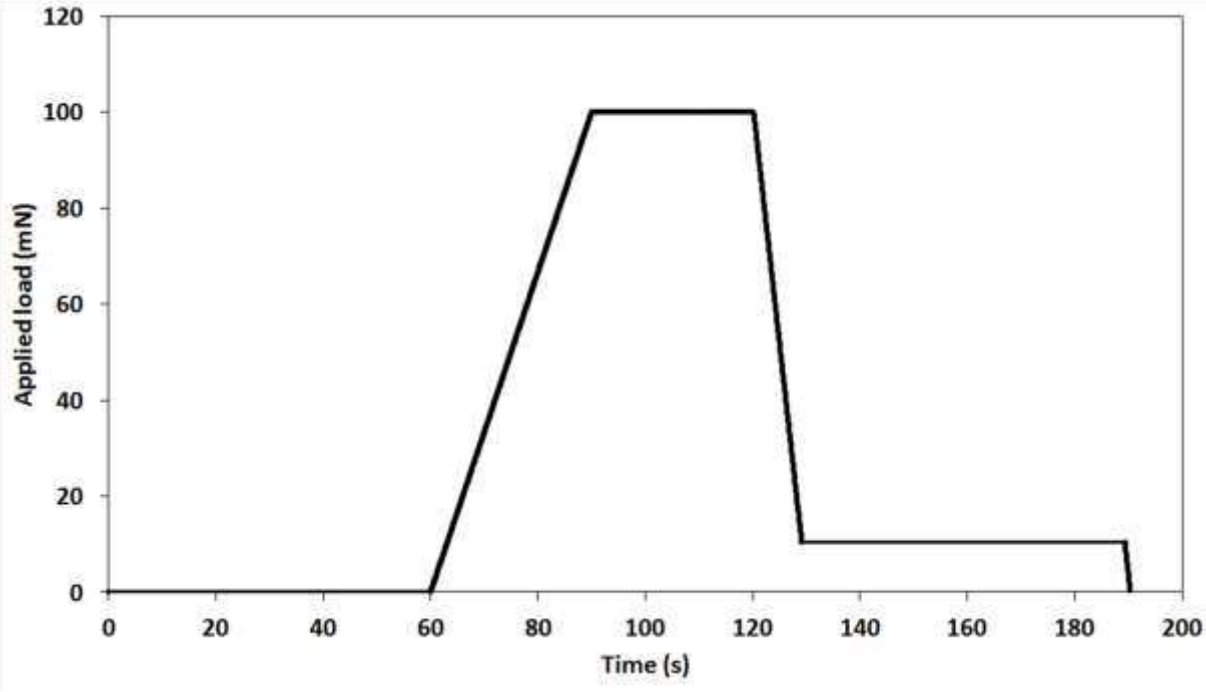
Applied load (mN)
120
100
80
60
40
20
0
0
20
40
60
80
100
120
140
160
180
200
Time (s)

4(b)

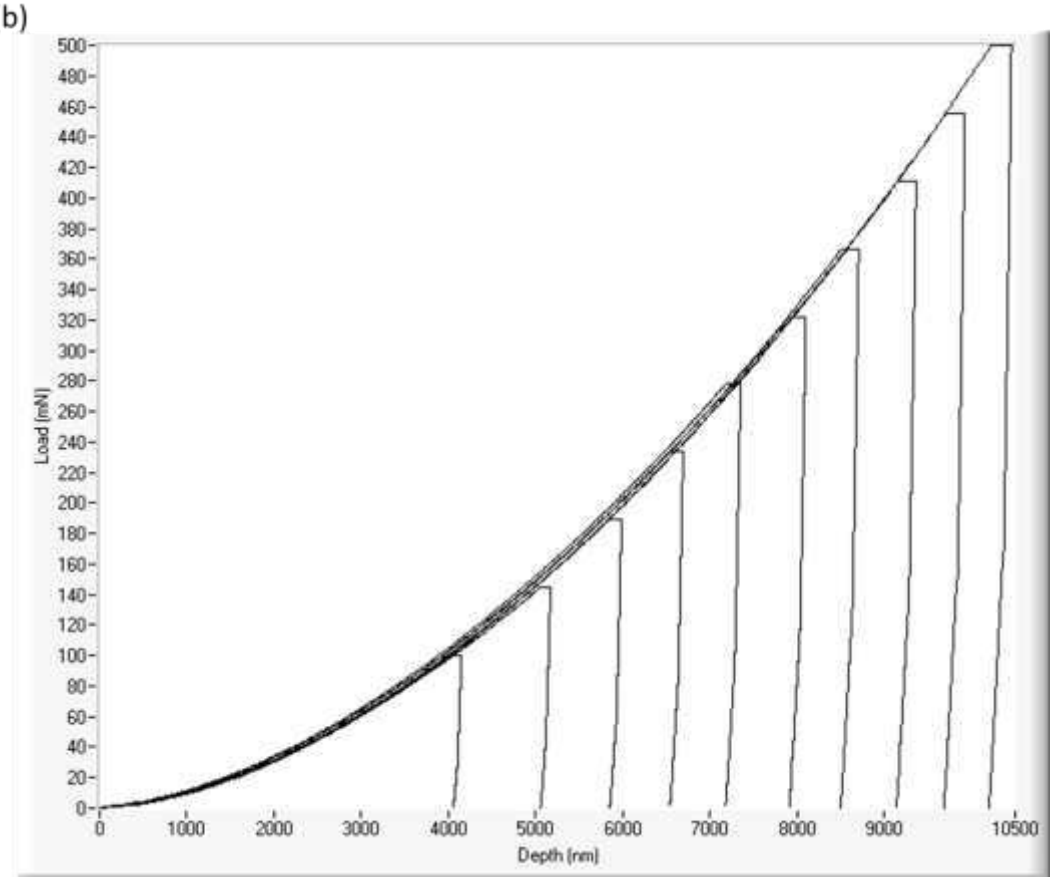
Load (mN)
500
480
460
440
420
400
380
360
340
320
300
280
260
240
220
200
180
160
140
120
100
80
60
40
20
0
0
1000
2000
3000
4000
5000
6000
7000
8000
9000
10500
Depth (nm)

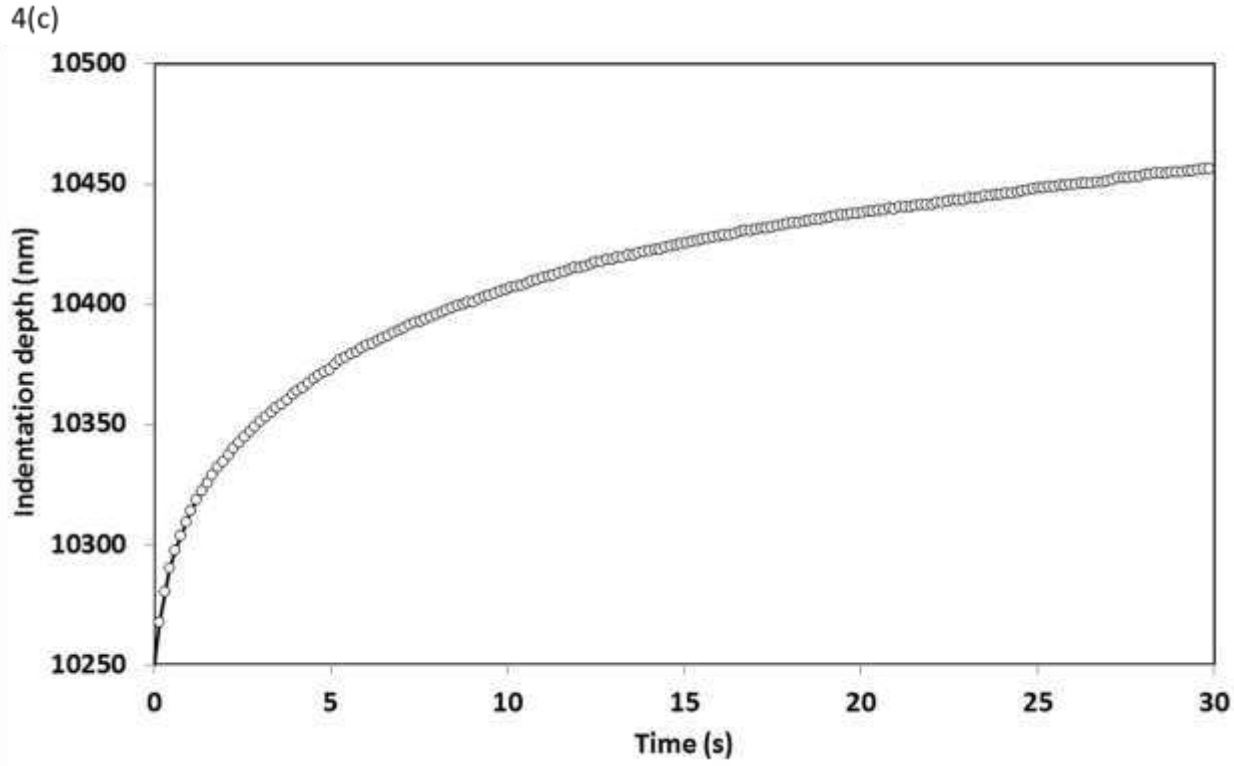

Figure 4: (a) Illustrative nanoindentation loading history for a metallic sample (b) indentation creep during 30s hold at peak load at 500 mN on single crystal Al (c) nanoindentation behaviour at 100-500 mN on single crystal Al

The suitability of the elastic unloading analysis for polymeric materials that show pronounced viscoelastic behaviour has been questioned for the same reasons. Nevertheless, a similar approach to that recommended above for metals has recently been applied to a range of commercial polymers by Young and co-workers at NPL [12]. The elastic modulus measurements showed reasonably good agreement with supplier quoted values (presumably from bulk methods) and a new atomic force microscopy technique using Hertzian contact mechanics. Dub and co-workers found non-constant elastic modulus vs. load for copper samples when following the ISO14577 approach [13]. The complex non-linear behaviour found was considered to arise from limitations to this method. Whilst the ISO standard does have some deficiencies and simplifications, in this case it is not clear that at least some of the experimental trend observed might have been due to the load history employed (constant loading and unloading time, in conjunction with no obvious hold at peak load for creep).

2.2.5 Surface roughness

It can be beneficial to make measurements over a wide load range, and instrumentation with a restricted load range has limitations for (1) testing on rougher surfaces (2) the accuracy of the extrapolation for coating-only modulus determination (3) investigating fracture behaviour. For results to be completely free of surface roughness the ISO standard recommends that the indentation depth be x20 greater than the R_a surface roughness [1]. Therefore, provided the coating is sufficiently thick that the plastic stress field does not extend into the substrate, measurements at larger load will show smaller scatter due to roughness. If roughness is high then confidence can be increased by performing a much larger number of measurements. For arc-deposited PVD wear resistant coatings designed for cutting tools the surface roughness can be typically R_a = 0.1 μm or more requiring 30-40 indentations. The use of a calibrated contact load which can be increased for rougher samples (as in the NanoTest) is an additional way to mitigate the effects of high roughness. Some nanoindenter designs use a reference ring method to subtract out some thermal drift but such approaches can prove problematic for rough samples and/or complex sample geometries. Schwarzer and co-workers commented that it was impossible to repeatably test thick (Ti,Al)N and CrN coatings with such an instrument due to high surface roughness [14].

2.2.6 Determination of frame compliance

Removal of the contribution of elastic bending of the nanoindentation instrument from the raw data is required before analysis to determine H and E. Frame compliance is the inverse of stiffness. It is common to use compliance rather than stiffness as the relationship is simply

$$C_t = C_s + C_f \quad (5)$$

Accurate determination of this frame compliance of the instrument is therefore essential, particularly for reliable modulus measurement. This can be done by direct or indirect methods. ISO 14577 describes both. The direct approach is less well-established but assumes nothing about the elastic properties of a reference material or the reliability of the contact mechanics and may prove increasingly popular in future. In principle a rigid contact is made between the load application part of the instrument and the rest of the frame so that all the measured deformation results from the compliance of the frame with a zero contribution from sample compliance [15]. The indirect method is much more common and relies on the sensitivity of the reference material(s) to the instrument stiffness and to the accuracy of the indenter area function used.

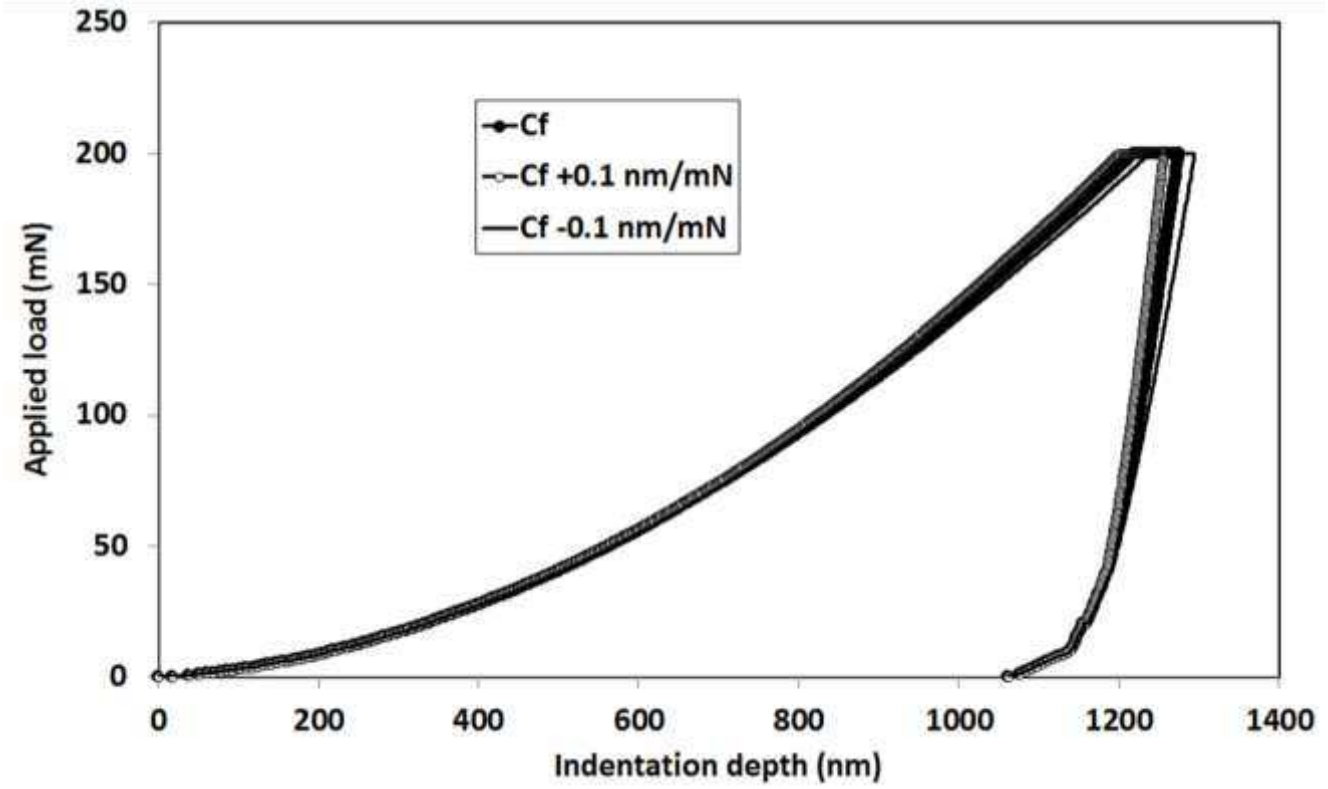

Figure 5: Indentation curve on single crystal tungsten after correction of frame compliance together with simulated curves with the frame compliance incorrectly determined

As an illustration of this, figure 5 (a) shows the indentation curve on a tungsten reference sample analysed with the correct frame compliance of 0.38 nm/mN for the instrument used. Figure 5(b) shows the true indentation behaviour together with simulated curves corrected for frame compliance of (0.36 + 0.1) and (0.36 – 0.1) nm/mN rather than the correct value. The high sensitivity of the tungsten reference sample to the value of the frame compliance used in the calculation is due to its low H/E ratio. Since accurate frame compliance also requires an actual area function, the use of multiple reference samples is attractive. ISO 14577 recommends the use of two reference samples with widely differing elastic modulus. Accurate frame compliance calibration is even more important as the load increases into the micro-range since the proportion of sample compliance to frame compliance decreases.

2.2.7 Determination of the area function

This can be done directly or indirectly. In common practice the area function is determined indirectly by indentations over a wide depth range into a homogeneous material with known elastic modulus (e.g. fused silica), with more measurements at the lower loads. A function is then generated which relates the projected contact area and the contact depth so that a constant reference value of elastic modulus is returned over the fit range. The relationship between area and depth for an ideal Berkovich indenter is $A_c = 24.56h^2$. In

practice all indenters are slightly rounded at the very apex and area functions are usually improved by the use of more measurements at lower load in the fit so that the relationship is accurate in this range. Area functions can be simple or apparently complicated relationships. On the simpler side, a function of the type $A_c = Ah + Bh^2$ is a reasonably robust approach which can often deliver modulus measurements to within about 2% of literature values across a wide depth range. It has the advantage of being able to be used to estimate the shape for depths above which calibration data exist so that measurements can be made on very soft materials. Nevertheless, not all pyramidal indenters are well fitted by such a simple relationship and polynomial fits (e.g. from 2^{nd} order to 5^{th} or more) or spline fits can be preferable in many cases. However, higher order polynomials should not be used outside of their fit range as they will diverge strongly. Another limitation of using fused silica is that above a threshold load (ISO14577 suggests 75 mN for a Berkovich indenter but the exact value will depend on indenter sharpness) it cracks. Although such cracking is relatively minor for the Berkovich geometry compared to indenter geometries with more acute angles where discontinuities can clearly be seen in the loading curves, the cracks are clear in SEM images of indentations and there will presumably be some subtle effect on the load-displacement curve even if obvious pop-in type features are absent.

ISO also notes the possibility of more directly measuring the area function with a traceable (metrological) AFM. This has the potential advantage that any issues concerning the accuracy of the contact mechanics used in the analysis such as radial dilation on fused silica [8] are eliminated but the AFM measurement itself may be subject to some uncertainty, particularly at shallow depths. Dub and co-workers have suggested that AFM measurements are typically subject to up to 7% error [13]. Nevertheless, in future the AFM-based calibration may become more popular, particularly for certifying the geometry of master indenters for cross-calibration purposes. For day-to-day calibration the indirect method is expected to continue to remain popular as the most convenient way to assess any changes in geometry of an indenter, e.g. after continued indentations into a hard tool coating or steel. In practice the area functions of new indenters can change significantly but often approach a quite stable, but not very sharp, geometry after a period of sustained usage.

2.2.8 Zero point correction

Precise surface detection and assignment of the exact point at which the initial contact was made are important requirements for accurate hardness and elastic modulus measurements, particularly at shallow depths. There are different strategies for doing this, based on whether pre-contact data are acquired or not. In one commercial instrument the zero point is defined by default at the position where the contact stiffness exceeds 200 N/m (~ x2 instrument spring stiffness). Moseson and co-workers have criticised this as being insufficiently reliable since they found it can lead to a false zero several hundred nm away from the actual point [16] although it is in widespread usage. The other main approach does not require pre-contact data, with surface detected when a pre-set contact force is reached. In the NanoTest, for example, the spring stiffness is typically x10 lower than in other nanoindenters and the initial contact force can be varied over a wide range (e.g. 0.5-50 µN) if required (minimised for accurate measurements in low-vibration environments, or significantly higher to combat high roughness and/or vibration levels). Since there is always some elastic deformation occurring before this point it is then necessary to correct the displacement data for the missing depth either assuming Hertzian (since even sharp indenters always have some rounding at the tip) elastic loading, or more generally power-law or linear extrapolation, as suggested in the ISO standard. An example of a Hertzian correction is given by equation 6 [5].

$$F = C(h - h_0)^{1.5} \qquad (6)$$

When indenting into a bulk material with well-known elastic properties it is therefore possible to back-calculate the radius of curvature at the tip, provided the data used are only to a small fraction of the radius, using equation 7. Chiang and co-workers have noted that for the Berkovich the transition between the spherical end cap and the pyramidal shape occurs at h_c = indenter radius/4 [17].

$$P = 4/3E_r\sqrt{(Rh^{3/2})} \qquad (7)$$

2.3 Indentation size effects

The onset of non-elastic deformation and the associated critical load can be marked by a displacement excursion (a "pop-in") or change in slope but this is not often the case, particularly for sharper indenters. Below this point the indentation behaviour is fully elastic. It is often called the elastic-plastic transition and it marks the onset of dislocation motion in metallic materials, but in semiconductors pop-ins may be caused or complicated by phase transformation events occurring once a critical pressure is reached (e.g. pop-ins on Si usually occur when the contact pressure rises to about 12 GPa [18]). Sapphire is another material that can show well defined pop-in behaviour [19]. Dub and co-workers observed clear pop-ins of >50 nm on Cu (111) and Cu(100) at around 0.5 mN when using a 407 nm tip radius (blunt) Berkovich [13]. They reported mean pressure values at the moment of homogeneous nucleation of dislocations (i.e. at the pop-in load) for Cu (111) and Cu (100) surfaces of 16.8 and 9.3 GPa respectively. Before yield metallic materials can support much higher contact pressure than their hardness post-yield.

Various indentation size effects (ISEs) can be observed, with hardness either increasing or decreasing as a function of depth. Several theories have been proposed to explain the most common ISE where hardness increases with decreasing indenter load, as in the example on tungsten shown in figure 6.

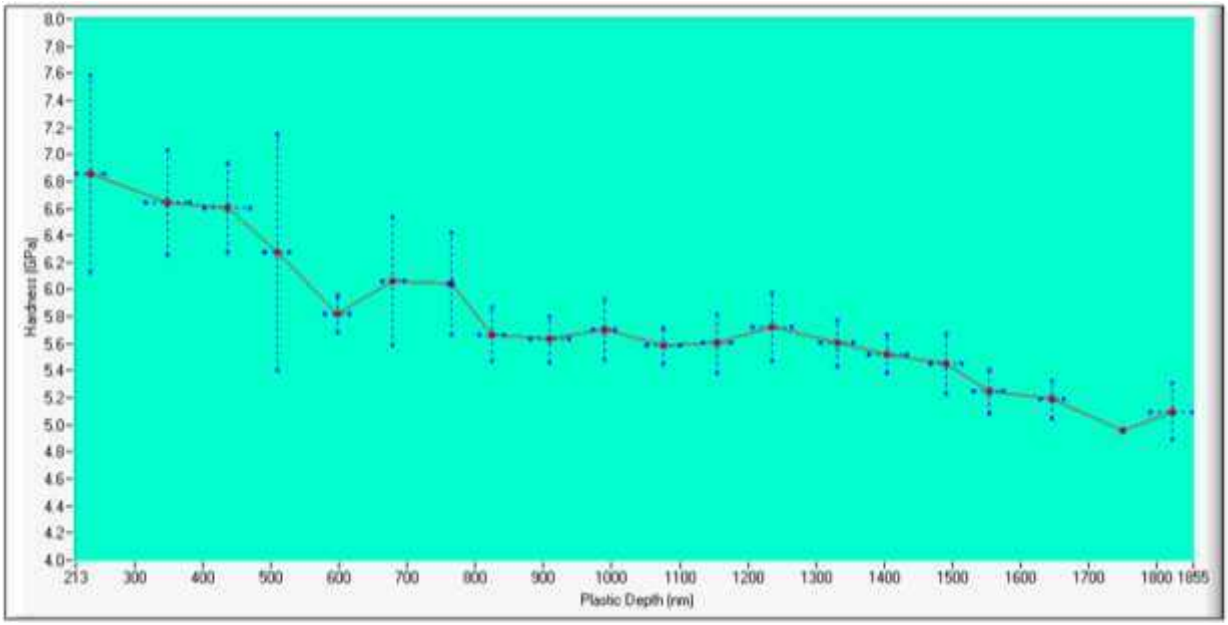

Figure 6: Polycrystalline tungsten shows a strong indentation size effect in hardness.

Arguably the most popular is gradient plasticity theory where geometrically necessary dislocations (GNDs) are generated under the indenter due to strain gradients. Decreasing the indentation size results in a greater density of GNDs and hence to higher measured hardness. The theory predicts that the total dislocation density within the plastically deformed volume varies as $1/h_c$, so that $H^2 \propto 1/h_c$. Nix and Gao fitted the hardness vs. depth dependence with a two parameter model, finding good agreement on a range of metals above indentation depths of 150 nm [20]. The two parameter model is shown in equation 8

$$H/H_0 = \sqrt{[1 + (h^*/h)]} \qquad (8)$$

where H_0 and h^* are constants obtained by fitting. Starink and co-workers have recently shown improved agreement at low depths by taking into account the rounding of the indenter [21]. They were able to apply their model to predict (i) the hardness of UFG Al-1050, a material with previously unknown ISE, to below 150 nm and (ii) dislocation densities from indentation data, finding good agreement with published dislocation density data for single crystal copper. In an interesting and as yet unvalidated idea Milman and co-workers have recently proposed a phenomenological approach to the problem of ISEs [22]. They noted that in general an empirical power law dependence is found; i.e. $P \sim h^m$ where $m \approx$ constant. Plotting log P vs. log h provides the exponent m. Alternatively, $H = Ah^i$ where A and i are constants and $i = m - 2$. These authors propose recalculating hardness of metals to a fixed depth of 1000 nm to enable comparison of studies at different loads.

2.4 Choice of indenter geometry and stress-strain curves

Sharp indenters induce full plasticity at low load so that the mean pressure measured in the test is the hardness of the material. In general for a conical indenter the strain is proportional to the tangent of the cone angle and so is constant at different indentation depths (for a pyramidal indenter there is an equivalent angle). Blunt indenters, or spherical geometries, do not always generate full plasticity immediately and more force may be required. The strain induced by a spherical indenter is proportional to a/R and is a function of depth. This suggests the possibility to generate stress-strain curves by indentation, with the load partial unload technique being able to generate the entire stress-strain curve in a single test. The stress-strain curve in a tensile test can provide the following information for structural design: (i) Young's modulus (ii) yield stress (iii) work hardening exponent (iv) ultimate tensile stress (v) strain at failure. Tensile tests suffer from limitations in specimen size and reproducibility and the possibility to obtain equivalent information from indentation is being actively investigated by several research groups. With FEA it is possible to generate the indentation curve from tensile stress-strain data but it is more challenging to uniquely solve the inverse problem and generate a tensile stress-strain curve from indentation data. Three main methods are (i) representative stress and strain (ii) inverse analysis by FEA (iii) neural networks. Residual stress is an added complexity, with the indentation force required to reach a given depth under tensile stress being lower than in the stress-free state and under compressive stress the force required is greater.

2.5 Plasticity index and H/E

Plasticity in contact is governed by the roughness and elastoplastic properties of the contacting surfaces. In an indentation contact plasticity is directly correlated with the ratio of hardness (H) and elastic modulus (E) [23,24]. For a given indenter geometry the load-displacement curve recorded in a nanoindentation test can be thought of a "fingerprint" for a material as it contains information about the elastic and plastic properties of the sample under test. A useful dimensionless property is the plasticity index (PI) which is the plastic work done during indentation (W_p) divided by the total elastic (W_e) and plastic work done during the indentation, over a wide range of H/E values, with the relationship taking the apparent form

$$PI = W_p/(W_p + W_e) = 1 - x(H/E_r) \qquad (9)$$

where x is a constant and E_r is the reduced indentation modulus. Prior to the development of nanoindentation, a plasticity index was proposed that related the deformation in rough contacts to the ratio of E_r/H multiplied by a geometric factor [25]. This original plasticity index is a general surface texture parameter that combines material and topographic properties of solids in contact. The equation originally developed by Greenwood and Williamson [25] is shown in Eqn. 10.

$$\psi = (E_r/H)\sqrt{(\sigma/\beta)} \qquad (10)$$

where ψ = a plasticity index, σ = standard deviation of the height of the contacting asperities and β = their average radius. Plastic deformation of asperities occurs even at minimal contact pressure when $\psi >> 1$ but when $\psi < 0.6$ deformation is largely elastic and plastic contact can only be caused if surfaces are forced together under very large nominal pressure. Although equations 1 and 2 differ in form both these plasticity indices reflect essentially the same behaviour with varying mechanical properties i.e. increasing H/E results in a lower plasticity index and more elastic contact [26]. Provided H/E_r is not greater than about 0.1 a good approximation to experimental data is given by Equation x although there is significant non-linearity above that and Chudoba and Jennett have noted that it should not be possible to produce plasticity with a Berkovich beyond H/E = 0.18 [8]. FEA gives x ~5 [15]. Beake and co-workers have reported that with several different Berkovich indenters values around 6-7 were found over a wide range of indentation peak forces for coatings and bulk materials such as copper, aluminium, tungsten, bearing steel, stainless steel and WC-Co, whilst only fused silica and K7 glass show lower x values very close to those predicted by Cheng and Cheng [26, 27]. H/E is well correlated with how elastic the contact is in other related mechanical contact situations such as scratching/sliding [28-30] or impact/erosion [31, 32]. Higher values result in higher critical loads for the onset of yield (non-elastic deformation) in indentation or scratch testing.

2.6 Hardness and elastic modulus of coatings

An often quoted rule of thumb is the so-called 1/10 rule where the relative indentation depth (RID = indentation depth/coating thickness) should be less than 0.1 to determine coating-only properties independently of the substrate [1,5]. In practice this usually works well for hardness but less well for elastic modulus. The ISO standard recommends Berkovich indenters should be sharper than 250 nm end radius for hardness measurement. Whilst this may not be really necessary for thicker coatings, sharper indenters are preferable for hardness measurements on very thin films. Accurate hardness measurement of a coating relies on development of a fully plastic zone within the coating. If the applied load is too small then the results can be influenced by surface roughness and the plastic zone may not be fully developed. If the applied load is too large then the plastic stress field may extend beyond the coating-substrate boundary and the measured response is therefore a composite of the plastic properties of both the coating and the substrate. Theoretical models based on approaches such as weighted area or volume law-of-mixtures have been developed to estimate the coating-only hardness from this composite response, with later work focussing on energy-based (work of indentation) models that have been adapted to include the effects of both plasticity and cracking [33].

As mentioned above, the elastic modulus measured at RID = 0.1 can be a poor estimate of the coating modulus, especially when there is a large elastic mismatch between coating and substrate. For example, Korsunsky and Constantinescu have predicted that when a coated system of E_c = 500 GPa, E_s = 100 GPa, ν_c = 0.2, ν_s = 0.3 (i.e. approximating to a stiff ceramic coating deposited on a much less stiff metallic substrate) is indented with a conical indenter the modulus is 25 % lower at a RID of 0.1 than the true coating value [33]. ISO14577 part 4 recommends making measurements over a range of indentation depths, provided that a/t_c is less than 2.5, and extrapolating to zero depth to obtain a value of the coating modulus independent of substrate. In practice a linear extrapolation is a fairly robust approach which usually yields improved values from those determined from measurements to a RID of 0.1, although measurements to RID of 0.03-0.05 can also work well.

2.7 Ultra-hard coatings

Accurate and traceable calibration by methods such as ISO14577 can help validate or question the mechanical properties of new coatings. Veprek and co-workers have claimed deposition of ultra-hard nanocomposite coatings with hardness of ≥100 GPa (i.e. higher than diamond) [34]. This highly contentious claim has been the subject of an excellent critical review by Fischer-Cripps, Bull and Schwarzer [35]. These authors have provided compelling evidence for these reported hardness values to be over-estimated by a factor of ≈2. They were able to show that the analysis approach taken by Veprek and co-workers that obtained the correct hardness of a ultra-hard sample of known properties (industrial diamond) nevertheless under-estimated the elastic modulus by a factor of ≈3 proving that the calibration and analysis method was not accurate. Additionally, since the elastic modulus of the nanocomposite coatings in question was only in the region of 450 GPa, it should theoretically not be possible to produce coatings with hardness over ≈65 GPa due to the limit in H/E with a conical indenter.

2.8 Depth profiling

There are three popular methods for obtaining properties such as hardness, modulus and contact stiffness as a function of depth. These are (i) performing indentations to differing peak loads (ii) dynamic indentation (otherwise known as continuous stiffness measurement, or CSM) (iii) multi-cycle loading (or load-partial unload testing). The most obvious, although quite time-consuming, is simply to perform indentations at different locations with different peak loads and consequently stress fields. The CSM method has recently been called into question by Cordill and co-workers who noted that the oscillation used with dynamic indentation techniques alters the measured hardness value of ductile metallic materials, especially at depths less than 200 nm [36]. The alteration in the hardness is due to the added energy associated with the oscillation which assists dislocation nucleation. In other words, there is inherent risk in trying to determine properties by oscillation as you are completely changing the dislocation density of the material you are trying to measure.

However, provided the test instrument has good thermal stability nanoindentation experiments can easily be performed over longer duration as multi-cycle tests, enabling effective hardness and modulus determination as a function of depth without risk of altering the surface of soft materials by imposing an

oscillation. Figure 7 shows an illustrative load-partial unload test result for a hard diamond like carbon (DLC) film deposited on silicon. The inflexion in the curve marks the point at which the plastic stress field is no longer completely within the coating and the measured hardness becomes a composite response of the coating and the softer substrate.

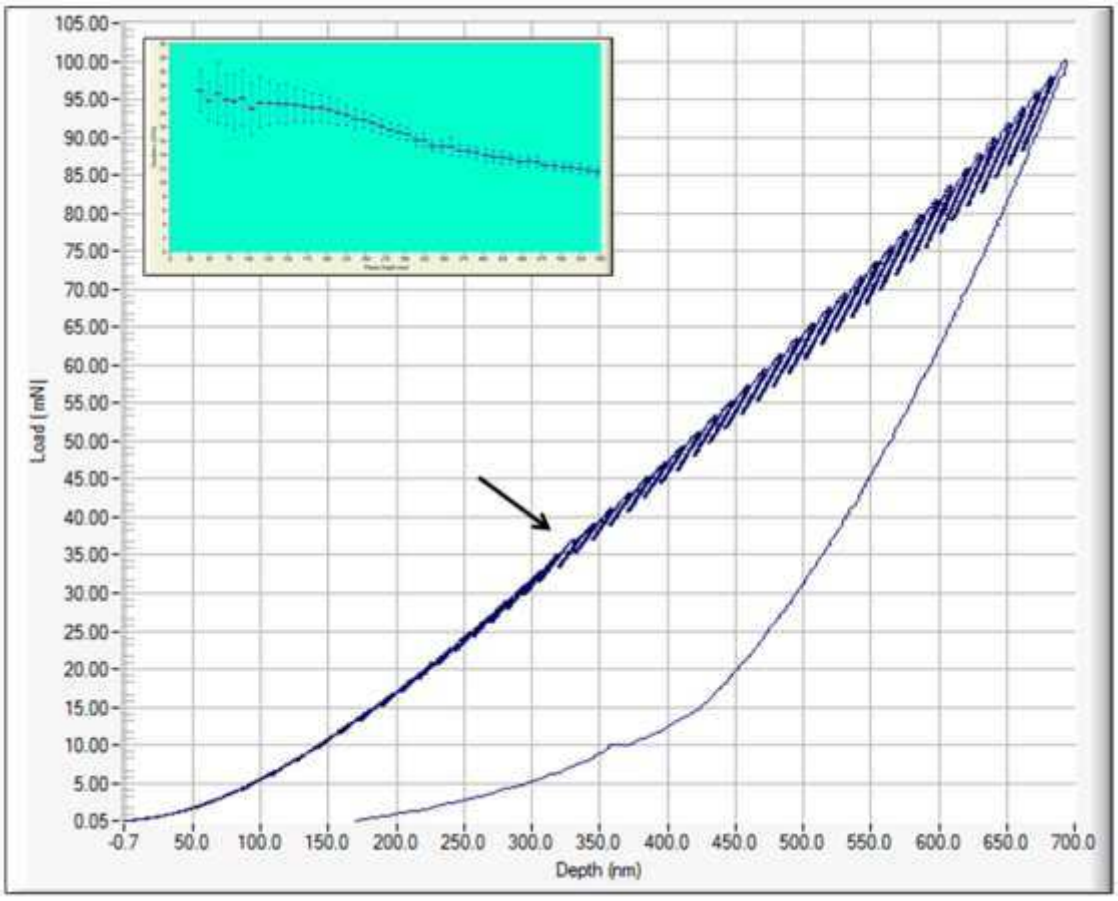

Figure 7: A 50-cycle load-partial unload test on a 2 μm DLC film on Si. The inset shows variation in hardness with depth from repeat tests

2.9 Mapping and positioning

Nanoindentation instruments have precision stages enabling accurate positioning in discrete phases to obtain highly localised mechanical property information. Experiments are typically performed as large automated arrays (e.g. 10 x 10 or 20 x20 grids of indentations) or more focussed tests involving a smaller number of indentations precisely positioned in the phases of interest.

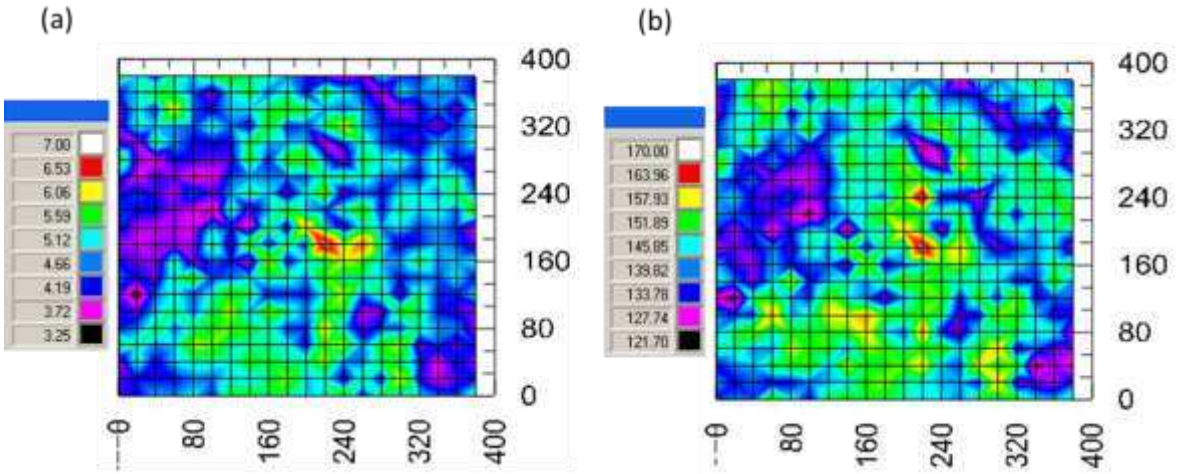

Figure 8: A grid of 400 indentations into Ti6Al4V reveals subtle mechanical property variations across the surface

An example of grid mapping is shown in figure 8. Here 400 indentations have been made into a Ti6Al4V aerospace alloy as a 20 x 20 grid. Average values of hardness and reduced elastic modulus were (4.5 ± 0.5) GPa and (139.7 ± 7.5) GPa respectively. More information is revealed in the hardness and modulus maps, with distinct areas of lower mechanical properties. Indentations can be placed closer together (e.g. 1-2 μm pitch) to obtain higher resolution maps. In the example below inclusions of an Al_7Cu_2Fe intermetallic phase can be seen to have completely different mechanical properties to the bulk matrix.

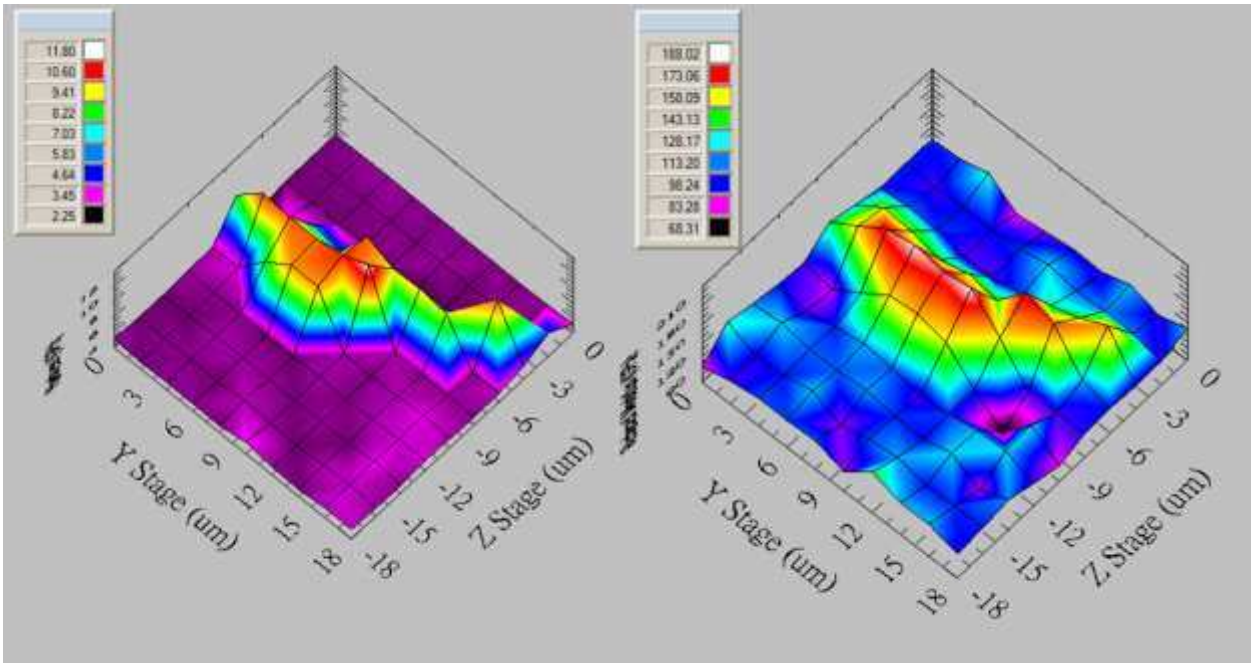

Figure 9: Mapping the mechanical properties of an intermetallic inclusion in a 7000 series Al alloy

2.10 Fracture toughness

Depending on load, material, indenter geometry and environment, five major types of cracks occur in the indentation of brittle bulk materials or thick coatings [37]. These are: (a) cone cracks (b) palmqvist radial cracks (c) median cracks (d) lateral cracks (e) half-penny radial cracks. Fracture toughness can be determined from the crack systems by either stress-analysis-based or energy-based models. The application of these to the determination of the fracture toughness of thin coatings has been well summarized in an excellent recent review by Chen [38]. Lawn and co-workers showed that for a well-developed radial/median crack system i.e. half-penny like cracking caused by indentation that the K_c fracture toughness of the material was proportional to the applied load multiplied by the average crack length c raised to the power of -3/2 [39] (equation 11).

$$K_c = C(E/H)^{1/2}P/c^{3/2} \quad (11)$$

where C is a geometry constant commonly taken as 0.016 for Berkovich or Vickers and 0.032 for cube corner indenter geometries. However, as the thickness of the coating is reduced it becomes more difficult to apply this equation due to the interference of the substrate and interface with the coating crack system. If the load is reduced to avoid this complication then the crack system is not sufficiently well developed to apply the analysis. For thinner coatings the energy-based models refined by Bull and Chen can be more applicable [40].

2.11 Micro-pillar compression, micro-cantilever bending and push-out tests

Introducing an indenter into a sample surface produces a complex stress field which can make determination of mechanical properties more challenging. A sharp indenter such as a Berkovich will drive plasticity almost immediately on contact. Whilst this is required in order to measure hardness it does present limitations when material behaviour within the elastic limit is to be investigated. Additionally, as an indenter continues to penetrate a sample surface, an exponentially increasing volume of material becomes involved in the deformation. As the indentation progresses, there will constantly be new material entering progressively advanced stages of deformation and this can create difficulties in understanding the

deformation mechanisms at work. In macro-scale experiments such problems are obviated by using tensile or compressive load application to a sample of a known cross-sectional area. This produces a constant stress at any given point along the specimen (at least until plasticity is initiated locally). Modern sample preparation techniques, in particular Focussed Ion Beam (FIB) milling, now allow the manufacture of microscopic equivalents of the samples used in the conventional macro-scale techniques. The most popular sample geometry used is the micro-pillar [41-43]. There is also growing interest in Micro-cantilevers (or "bend bars") which may be produced using the same technique.

Micro-pillar Compression

For almost a decade now interest has been growing in the field of micropillar compression experiments. Uchic et al used the technique to demonstrate size effects on the measured strength of Ni and three Ni based alloys [41]. They demonstrated that micro-pillars of practically manageable dimensions (0.5 to 40 µm diameter) were sufficiently small to show the relationship between strength and volume based phenomena such as dislocation nucleation and movement. Once the pillars have been produced they are carefully positioned in front of a flat topped indenter commonly known as a flat punch. This is achieved by positioning the sample precisely in the crosshair of the nanoindenter's microscope then moving to the indenter position (the vector from microscope cross hair to indenter centre is calibratable and automatically executable on most nanoindenters to better than 1 µm precision). Once in position the load is applied to the micropillar using the flat punch indenter. The example below shows a load vs. displacement trace from a micropillar compression experiment. As can be seen, the data are easily converted to engineering stress and engineering strain due to the dimensions of the micropillar being well characterised and there being no constraining material surrounding that being tested.

Although pillars are the most common geometry for microcompression experiments, other structures have been tested. By compressing of variously shaped wall-like structures with differing length-to-width ratio Jennett and co-workers provided evidence that yield strength is determined by the smallest dimension of the structure ("thinness") [44]. Their results showed that yield stress was determined by wall width with length playing little or no effect.

Micro-cantilevers

Micro-cantilevers are produced in a similar manner as micro pillars. A FIB is used to cut out an elongated three sided trough leaving and island of material of the length and width of the required cantilever. The FIB is then re-orientated such that it can be used to undercut the cantilevers, allowing them room to deform as the load is applied.

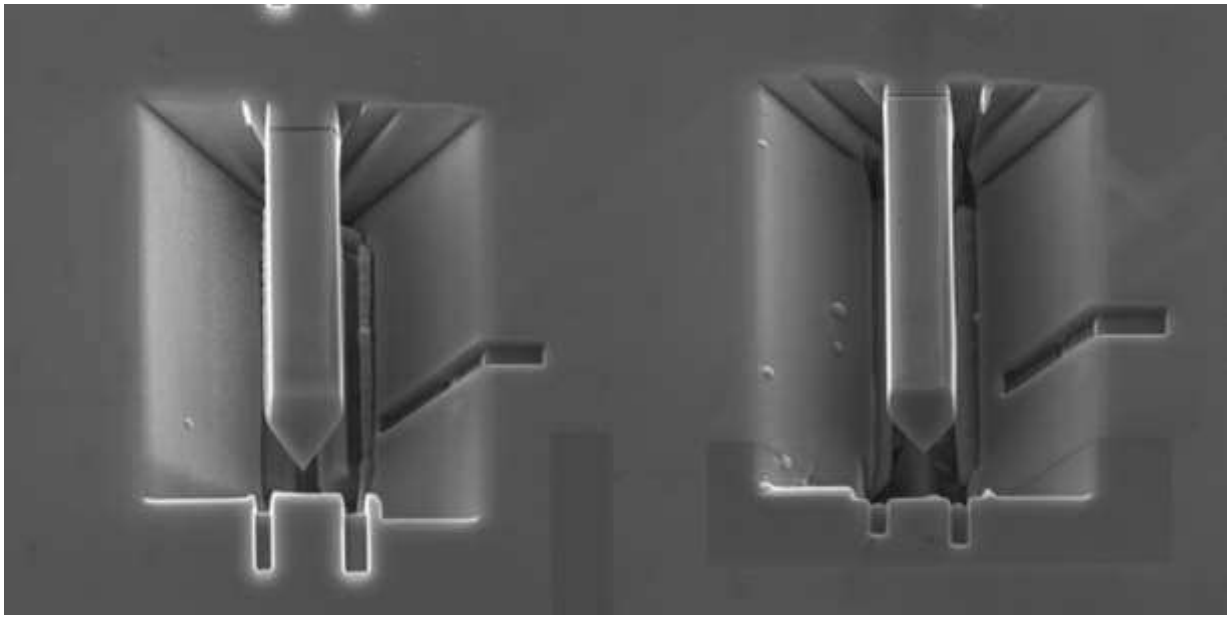

Figure 11: SEM image of two micro-cantilevers cut into a silicon wafer. These samples have been prepared for brittle to ductile transition experiments over a range of temperatures and as such have had a crack initiation notch machined into them near their roots. These cantilevers are 4 µm wide and 15 µm long. Image courtesy of Dr David Armstrong, University of Oxford.

Similarly to micropillars, micro-cantilevers may be targeted using an integrated optical microscope but more commonly a 3D imaging stage is used. This allows the cantilever to be imaged whilst mounted on the nanoindenter. The sample is mounted on a high precision feedback controlled piezoelectric stage. The sample is either raster or bi-directionally scanned whilst the indenter is held on the sample surface under a very low load (~1 µN). The scan parameters are defined by the user, these include the dimensions of the imaged area and the resolution of the image (number of scanned lines). A 3D image of the sample is produced from a combination two sets of coordinates from the piezoelectric stage and the third set of coordinates from the indenter depth sensor.

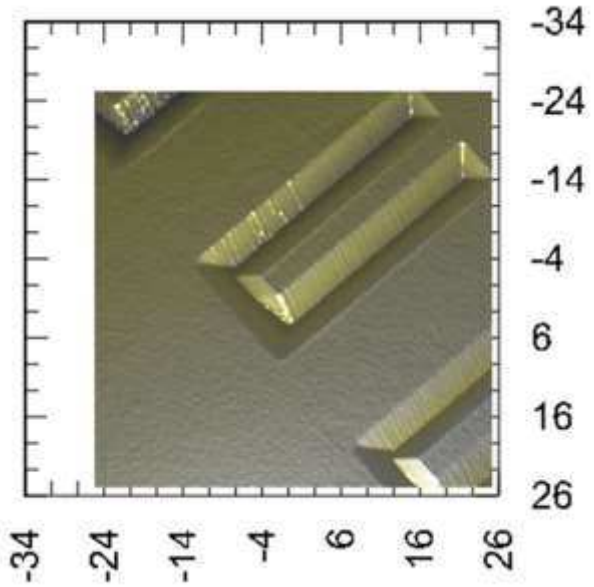

Figure 12: *3D "nanopositioner" i*mage of cantilevers machined into W. Note that the true cross-section of the cantilevers is not see due to the geometry of the Berkovich indenter used for imaging. Image size is 50 µm x 50 µm

The resultant image may then be used to select the point(s) at which the indenter is applied to the cantilever to apply the bending load. The distance between the root of the cantilever and the chosen contact point(s) are easily determined from the 3D image and as such the stiffness of the cantilever may be determined once the bend test has been completed. The stiffness value may then be used to determine the elastic modulus of the sample material using beam theory. This approach is well documented by Armstrong et al. [45] where cantilevers were FIB machined into selected copper crystals whose orientations had been previously characterised by Electron Back Scatter Diffraction (EBSD). The combination of the data from both techniques demonstrated the anisotropic nature of mechanical properties as a function of crystal orientation.

Fibre push-out

The most performance critical aspect of a fibre reinforced composite material is the strength of the bond between the matrix and the reinforcing fibres. It is therefore desirable to be able to measure the strength of this interface. One technique for making such a measurement is the fibre push-out test. These tests are undertaken using a nanoindenter fitted with a flat punch indenter. The target fibre is selected under the instrument microscope and the sample moved to the indenter position such that the indenter contacts concentrically on the selected fibre. Jouannigot et al [46] have used this technique to mechanically characterise the fibre/matrix interface of carbon/carbon composites.

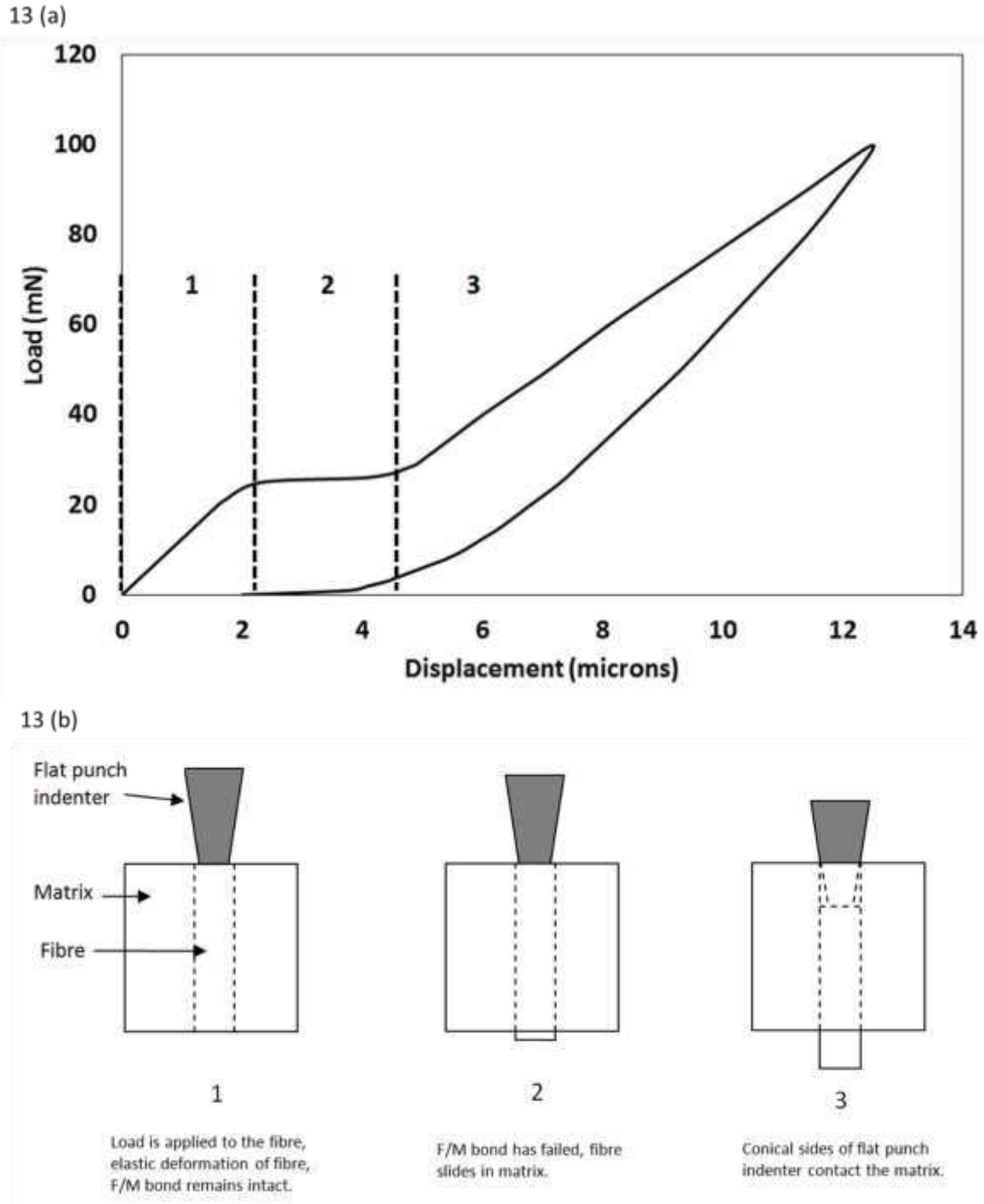

Figure 13: (a) and (b)

3. Nanotribology (nano-scratch and wear)

Increasing use of thin films and coatings from a few nm to about 1 micron thickness for improved wear resistance in MEMS and general thin film applications requires their mechanical properties and tribological performance are optimised. Since the test conditions in the conventional macro-scale scratch test (R = 200 μm) were specifically chosen for fairly thick (≥3 μm) coatings they are not appropriate for much thinner films and nano-scratch and nano-wear tests are needed. These tests typically use considerably lower load combined with a smaller probe radius than macroscale tests to achieve the required combination of surface (and lateral) sensitivity and high contact pressure to drive film failure.

Integrated precision control of the movement of the sample stage independently of the load application during the test enables various topographic, scratch and wear tests to be performed. In the NanoTest, for example, there are four distinct types of test:-

(i) Topographical scan – where the sample is scanned under a light (no wear) load to obtain a line-profile of the surface and quantitative roughness statistics

(ii) Progressive (ramped) load scratch – either initially or after a set levelling distance a linear load ramp
(iii) Topography-scratch-topography (3-scan) test
(iv) Multi-pass wear tests - involving various combinations of topography and either ramped or constant load scans

The tangential (frictional) force can be recorded simultaneously, which provides valuable confirmatory information on the location of failure relative to the moving test probe.

3.1 Critical load sensitivity to intrinsic and extrinsic factors

Steinmann and co-workers showed that the critical load in the scratch test can be influenced by a range of extrinsic and intrinsic factors [47]. The influence of the scan parameters of loading rate and scan speed on the critical load has been investigated for a range of Si-doped DLC coatings on glass that show clear film failure in nanoscratch tests [48]. There was considerably less sensitivity to these scan parameters than has observed in macro-scale scratch testing. At the macro-scale the dL/dx ratio, where L = normal load and x = scratch distance, was found to be an important parameter, with the critical load decreasing when dL/dx decreases. Steinmann and co-workers recommended tests be done with a fixed dL/dx of 10 N/mm, suggesting that when dL/dx decreases, the probability of encountering defective adhesion within a certain load range increases resulting in a decreased critical load. This explanation may not be true for highly homogeneous coatings that do not fail by selective failure of poorly adhering regions and so exhibit very consistent L_c values, and also does not consider the possibility of cohesive failure.

In contrast at the nano-scale, no dependence on critical load was found for Si-doped DLC coatings on glass on either (1) scratch speed, (2) loading rate, or (3) increase in load per unit scratch distance (dL/dx) when dL/dx is much less than 1 N/mm, whilst critical loads only slightly increase at higher dL/dx (1-5 N/mm). More recently Beake and co-workers have investigated the variation in critical load for failure of a 80 nm ta-C film on Si over a 100 fold range of dL/dx without finding any clear dependence [48]. These results suggest that nano-scratch tests under significantly different loading conditions can be compared directly.

3.2 Topography-progressive load scratch-topography multi-pass scratch tests

An improvement on the basic nano-scratch test is the 3-scan procedure (with residual scan) that enables identification of failure mechanisms, the role of stress in particular, in more detail. All the major nanoindenter manufacturers offer this as part of their nano-scratch testing capability. The first reported multi-pass test of this type was described in detail by Wu and co-workers from IBM in 1989 [50]. Although common thereafter, it was not until after it was realised that it was possible to remove instrument compliance from the measured deformation that true nano-scratch and nano-wear depth data could be displayed [30]. The example below shows similarity in the low load response of Si(100) to indentation and scratch testing with the same spherical probe.

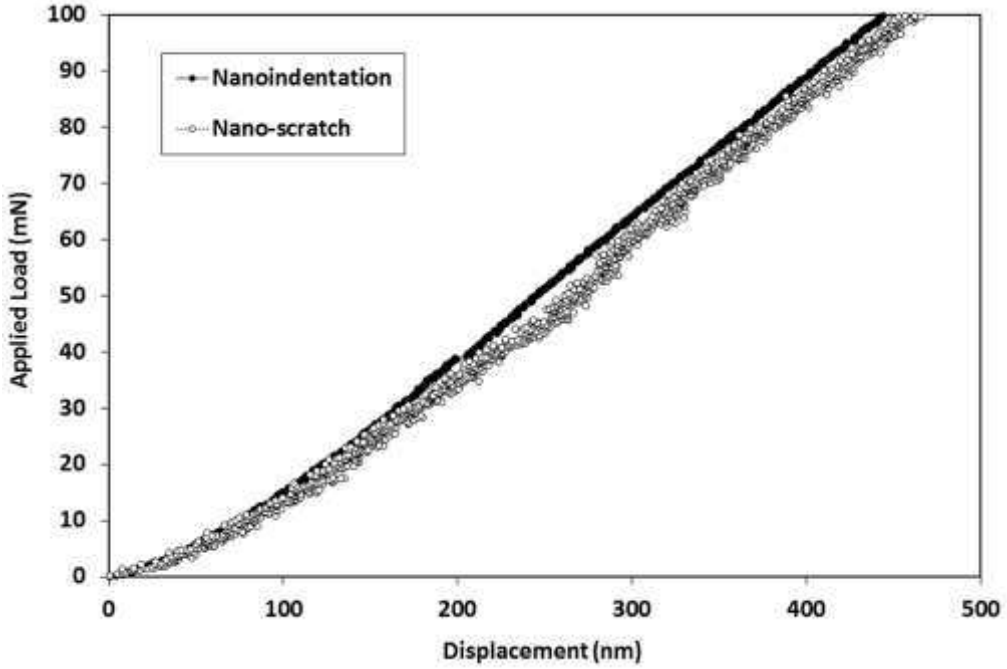

Figure 14: Load vs. depth curves in nanoindentation and nano-scratch tests on Si(100) with a 4.6 μm spherical probe

By performing three-scan progressive load nano-scratch tests it is possible to determine the critical load for the onset of non-elastic deformation since this is the load at which the residual scratch depth is no longer zero. The mean pressure at this point can be used as an estimate of the yield pressure. By increasing the load further it is possible to identify the critical loads for transitions for cracking and delamination events and converting these to mean pressures.

3.3 Influence of probe radius and geometry

The choice of probe radius in the nano-scratch test should be considered carefully. Spherical probes with end radii typically 1-10 μm are commonly used for nano-scratch testing. If probes are too blunt or the instrument used has a relatively small maximum load then it is not possible to scratch the coatings to failure. Sphero-conical probes with ~5 μm end radius represent an effective choice ensuring that coating failure is observed within the force range of the instrument but without risking rapid blunting of the indenter due to repeat scanning that can be observed when sharper probes are used (such as Berkovich indenters), especially when scratching hard and rough coatings. The use of the spherical indenters has the additional advantage that the contact pressure analysis described below can be directly applied to the nano-scratch data, provided the instrument software has the capability to remove the contribution of instrument compliance, sample slope and roughness from the measured deformation data so that true nano-scratch and nano-wear depth data is displayed. Pre-calibration of the indenter radius by nanoindentation is necessary.

Nevertheless, other geometries such as Berkovich [51] and cube corner have been used [52]. The latter combines a small end radius with high acuity and contact strain and so it particularly suited to the scratch testing of very thin films. Klocke and co-workers have used cube corner indenters to perform nano-scratch tests of 250 nm Pt-Ir coatings on cemented carbide tools used for precision glass molding [52]. They compared the scratch behaviour of the Pt-Ir coating without interlayers and the same coating with 15 and 50 nm thick Ni or Cr adhesive interlayers. Without an interlayer the coating failed at 25 mN but the critical load was much higher (x2-x8) on the coatings with the thin interlayers (figure 15). For a given thickness the coatings with the Cr interlayer out performed those with the Ni interlayer and for a given interlayer composition, the critical load for coatings with thicker interlayers was greater.

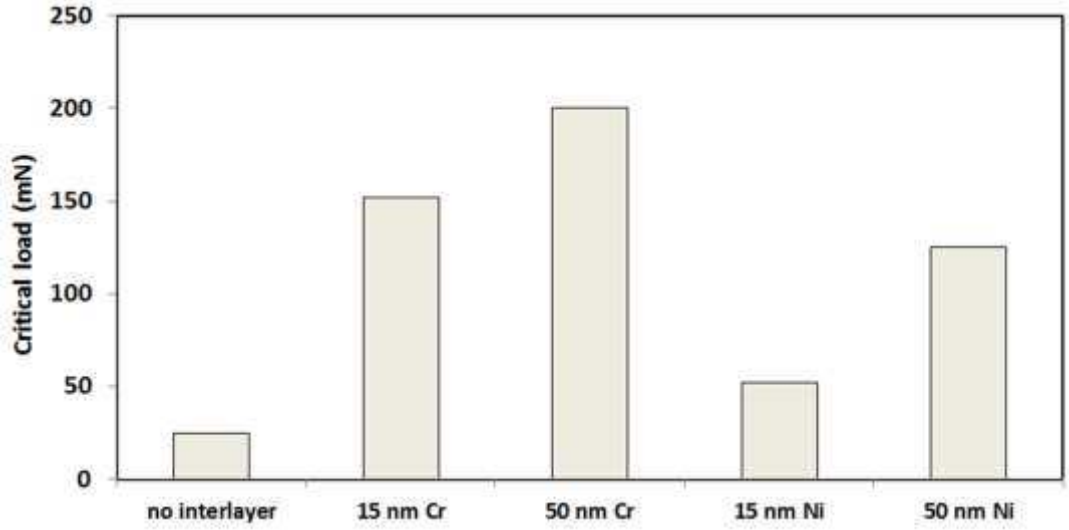

Figure 15: Influence of interlayer composition and thickness on critical load for Pt-Ir coatings

This appears to be a good example of dimensioning, where the probe sharpness was increased to improve the sensitivity to the adhesion at the interface. Schwarzer and co-workers have used advanced simulation tools to "dimension" macro-scale scratch tests of thick multi-layered cutting tool coatings [14]. By adjusting the scratch probe radius and applied load they were able to show the possibility to adjust the position of the depth of the maximum von Mises stress in multilayer coatings. By appropriate "tuning" they could position the maximum stress near the different interfaces in the coating-substrate system.

There have been occasional reports that the scratch depth under load may be greater for constant load than in progressive load testing but this does not appear to be the case in general. Beake and co-workers reported that for TiN on tool steel the deformation in constant load and ramped load tests was almost identical at the same load [53]. This implies that the critical load obtained in a progressive load scratch test is a reliable choice of determining a fractional sub-critical load to assess the film resistance to low cycling fatigue in a nano-wear test.

3.4 Contact pressure

Recently the capability of the progressive load multi-pass scratch technique has been extended by the development of a novel analytical treatment to obtain accurate scratch depth data after correction of the raw data for the contribution from instrument compliance, sample topography and sample slope [54]. The method described in reference 54 enables the yield stresses and the pressure required for the failure of the film to be estimated from contact mechanics, assuming the geometry of indentation, provided spherical indenters are used. By using spherical probes the contact depth (h_p) in an indentation contact is given by

$$h_p = (h_t + h_r)/2 \qquad \text{[Eqn. 12]}$$

where h_p is the contact depth, h_t is the on-load scratch depth and h_r is the residual depth from the final scan. The contact radius (a) is determined from Equation 13, where R is the indenter radius.

$$a = \sqrt{(2Rh_p - h_p^2)} \qquad \text{[Eqn. 13]}$$

$$P_m = L/\pi a^2 \qquad \text{[Eqn. 14]}$$

The contact pressure, P_m, at any point along the scratch track is given by equation 14, where L is the Applied load. To apply this approach to the nano-scratch data it is necessary to assume that:

(1) the presence of a tangential load does not influence the pressure distribution too greatly (i.e. that the measured friction coefficient is well below 0.3)
(2) the radius of the indenter is constant
(3) the sliding speed is sufficiently slow and contact sufficiently close to elastic that the load is supported on the rear of the indenter
(4) the indenter can reach the bottom of the scratch track in the final topographic scan.

In practice it appears that these conditions can often be met in the nano-scratch test [54, 55], although the approximation becomes less valid as the geometry moves away from Hertzian. The methodology has been validated for thin films on Silicon wafers with good agreement between (i) scratch hardness independently determined from optical measurements of scratch widths (ii) contact pressures for film and substrate yield events.

3.5 Influence of film stress and thickness

Beake and co-workers have reported nanomechanical and nanotribological (nano-scratch and nano-wear) characterisation of a wide range of thin films on Si, with thicknesses from 5 nm (ta-C) to 1500 nm (TiN) performing nanoindentation with Berkovich indenters combined with nano-scratch testing with spherical indenters [49, 54-57]. A key motivation for studying several of these was to understand the interplay between film thickness and interfacial toughness for MEMS and protective thin film applications. The reliability of Si-based MEMS devices is limited by stiction forces when contact occurs. Applying very thin, low surface energy and low stress coatings can alleviate this problem but it is critical that they are deposited optimally.

The film thickness is a key parameter influencing the critical load in the nano-scratch test. In principle, film thickness can have two opposing effects:- 1) thicker films that are harder than the underlying substrate provide more load support and so delay the onset of the substrate deformation that is often the precursor of film failure (higher critical load) 2) thicker films can be more highly stressed and more easily through-thickness crack and delaminate when deformed (lower critical load) since the driving force for spallation to reduce stored elastic energy is greater. The relationship between film thickness and critical load can be quite complex in practice.

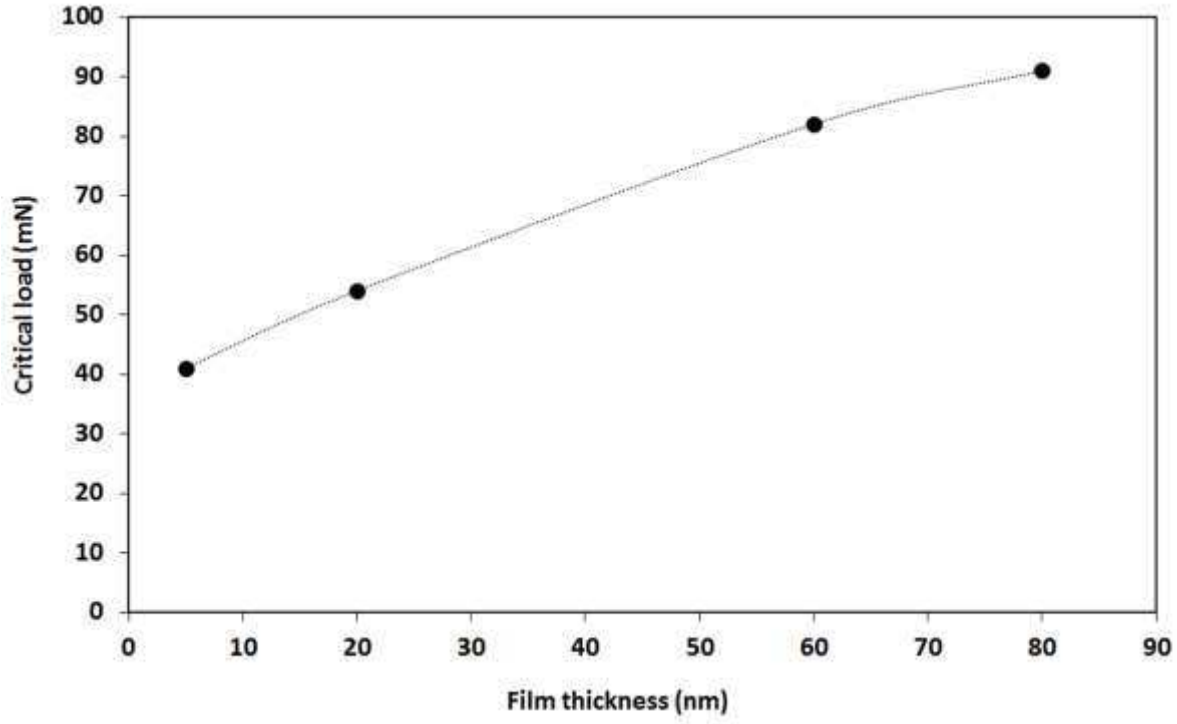

Figure 16: Variation in the critical load of 5-80 nm ta-C films on Si with thickness

Nano-scratch studies on 200-1000 nm CFUBMS a-C [57], 150-600 nm plasma enhanced chemical vapour deposited (PECVD) Si:a-C:H [48] and 5-80 nm ta-C [56] have reported that the critical load for total film failure in the nano-scratch test can be a strong function (often close to proportional) with film thickness reflecting enhanced load support and substrate protection. Figure 16 illustrates the dependence for ta-C films when using a 3.1 μm spherical probe. Provided the films are not too stressed it has been reported that the ratio L_c/t_f is approximately constant.

Shi and co-workers reported nano-scratch data for 200 nm and 1000 nm a-C films deposited with varying substrate bias voltage (-20 to -140V) by closed field unbalanced magnetron sputtering (CFUBMS) [57]. They found that on wear resistance grounds a suitable strategy for optimising wear resistance for MEMS applications was to maximise H/E. For 200 nm films the highest H/E materials performed best since the intrinsic stress in the film was relatively low (no recovery spallation and low H/E). For ~1 μm a-C films they observed a general relationship between H/E and the scratch test critical loads. When H/E_r is ~0.09-0.1 there was a tendency of the films to delaminate behind the moving probe at low critical load. Beake and co-workers previously reported a similar correlation for ~0.8 μm Ti-Si-N nanocomposites films on Si [50]. Higher H/E led to higher critical loads for elastic-plastic transition and also for the total film failure occurring in front of the probe. However, when H/E_r was >0.09 film failure was always by tensile failure behind the probe (also described as unloading failure). The high tensile stress behind the probe in the nanoscale scratch test can lead to complete failure for hard films on silicon. More information can be provided by nano-wear tests.

3.6 Repetitive nano-wear

Constant load, unidirectional multi-pass scratch testing was first described by Bull and Rickerby in 1989 [58] and has been shown to be an effective low cycle fatigue test. The same approach can be applied to micro- and nano-scratch testing. Constant load nanowear tests are often used to determine rates of sliding/abrasive wear and investigate the role of fatigue. The low-cycle nanowear experiments can often be much more informative regarding the influence of thin film stress leading to poor adhesion than single scratch tests. When compared to progressive load nano-scratch testing, nano-wear testing has the advantage that the load can be varied to tune the maximum von Mises stress to be close to the coating-substrate interface. The friction force is sensitive to the onset of coating failure.

Shi and co-workers performed sub-critical load nanowear testing to investigate the performance of 1 μm a-C films that fail in single nano-scratches at ~200 mN [57]. The wear test loads were chosen so that the maximum stresses were either within the film (at 50 mN) or the substrate (at 150 mN) so that the additional stress due to the imposed stress field from the scratch reaches the interface for the higher load test. In the lower load wear test the contact is almost completely elastic with residual wear depths under 100 nm. An approximately inverse correlation between H/E and the residual depth was found, consistent with the work of Matthews and Leyland who have shown that increasing H/E reduces plasticity [28-29]. An increase in residual wear depth and decrease in scratch recovery with each wear cycle confirm that the low load multi-pass wear test is a fatigue process. In marked contrast, the films failed after a few cycles at 150 mN. As $150/L_u = 0.7$ this is perhaps not too surprising, particularly as the load is great than that at which initial edge cracks form (L_{c1}). Nanowear under these conditions is a very low cycle fatigue test where plasticity and micro-fracture dominate and the harder films deposited under high bias perform poorly. The behaviour of 1 μm a-C films with a very high ratio of H/E, deposited under high substrate bias, is very strongly dependent on the test conditions, performing well at low load wear but very poorly in more highly loaded contact. They exhibit low critical loads in progressive load scratch tests and when they fail in the nano-wear test there is extensive delamination outside of the scratch track. The combination of nano-wear tests at different loading levels provides information regarding the suitability of the a-C films for contact applications.

Repetitive scratch tests can also be informative at the micro-scale, typically using 25 μm end radius diamond probes in conjunction with applied load in the range 0.5-5 N. Beake and Ranganathan used this approach to investigate the low cycle fatigue behaviour of mono-, bi- and tri-layer hard coatings deposited on WC-Co by CVD [59]. They found a strong influence of the total coating thickness on the micro-scratch and micro-wear behaviour. The micro-wear behaviour of the trilayer coating system (3 μm TiN on 4 μm Al_2O_3 on 5 μm TiCN) is shown to be superior to the bilayer and monolayer coatings in the figure below.

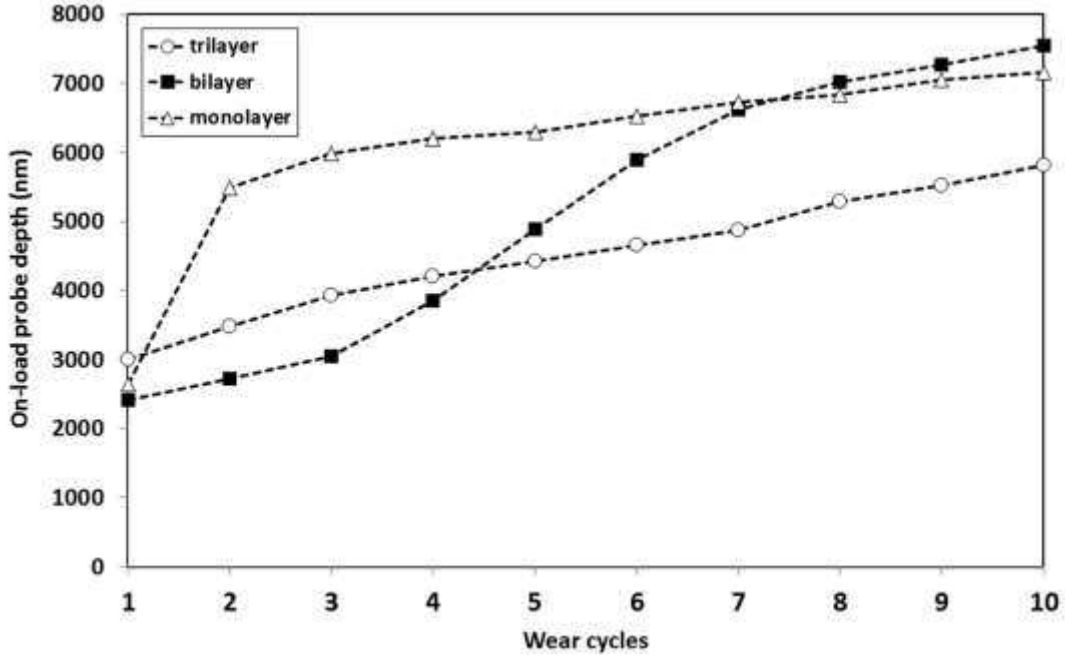

Figure 17: Influence of increased thickness and load support on critical load in the micro-scratch test

3.7 Surface roughness

Beake and co-workers have recently investigated the influence of coating thickness, roughness and the direction of scratching relative to grinding marks on the behaviour of TiN coatings on M42 steel in single and multi-pass nano-scratch (nano-wear) tests [53]. TiN coatings were deposited on M42 steel as this is a model system displaying clear failure with comparative frictional data available from previous macro-scale scratch testing. The critical load for delamination failure was dependent on coating thickness and scratch orientation relative to polishing marks on the surface made prior to coating deposition. High roughness tends to decrease the critical load but the load carrying capability of higher thickness can have a much greater effect. Despite being much smoother, the critical load on 500 nm TiN was only ~50% of the critical load on the 1500 nm TiN. The critical load was 20 % lower when scratching perpendicular to the grinding marks than parallel to them.

3.8 Friction

The friction force in the nano-scratch test can be deconvoluted into its interfacial and ploughing components so that the interfacial friction can be reported:-

$$\mu_{total} = \mu_{interfacial} + \mu_{ploughing}$$

This can be done by different approaches: (1) performing constant load friction test at very low force where contact is completely elastic and the ploughing contribution is zero (2) performing repetitive scratches to eliminate the ploughing contribution (3) performing progressive load scratch and extrapolating the low load friction data to zero load.

The friction force can be very sensitive to the onset of coating failure, depending on the failure location relative to the moving probe. Figure 18 shows the evolution of the friction coefficient with wear cycles at 100-300 mN for 1500 nm TiN on M42 steel being scratched with a 4.4 μm diamond probe. With repeat scratching the friction coefficient initially decreases due to a reduction in the ploughing component. Coating failure was marked by a sudden sharp increase in friction during a single wear cycle (cycle 2 at 300 mN and cycle 3 at 200 mN in figure 18) which is accompanied by an inflexion in the depth vs. wear cycle. After the abrupt increase in friction at film failure the friction decreases with continued scan cycles.

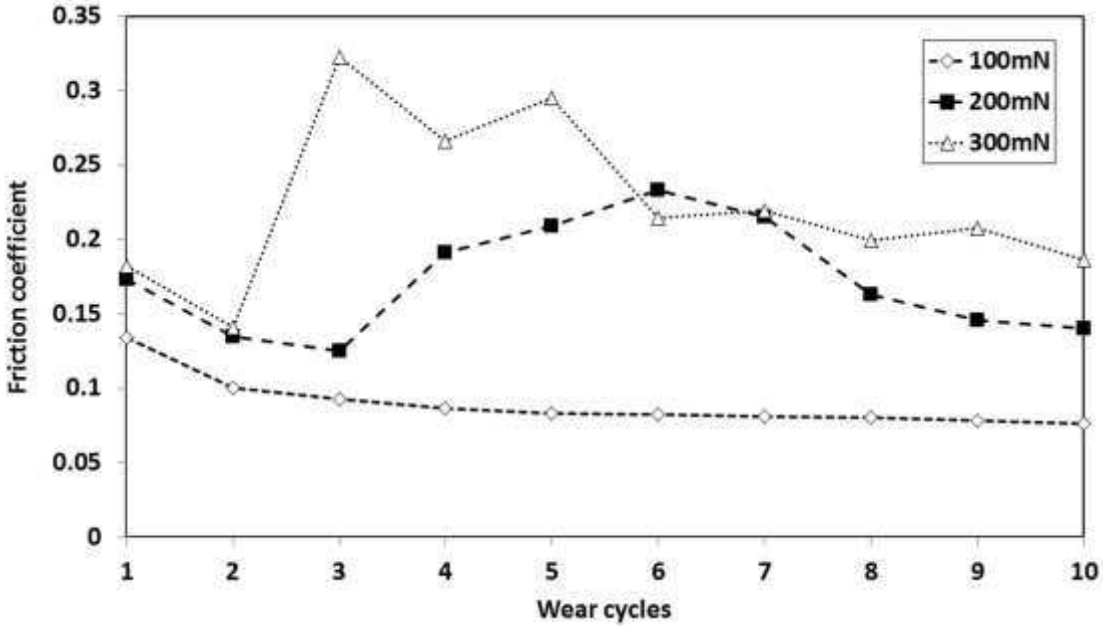

Figure 18: Variation in friction with number of wear cycles

4. Nano-fretting

Miniaturisation of mechanical devices results in severe contact conditions generated by relatively small forces. Performance of materials at small contact scales is a significant challenge and tribology becomes an enabling technology for any small scale devices with moving components. According to the Amontons' law, the friction force is independent of the apparent area of contact, however the law does not hold true when the contact area is dramatically reduced. Fretting experiments performed at small contact scales bring specific challenges including increased importance of surface energy and adhesion, role of wear particles and impact of surface roughness.

Nanotribology research involving nano-fretting investigations tend to focus on two main areas related to (i) fundamental science leading to the understanding of basic principles of friction and asperities contact, and (ii) applied research related to technology of small devices like nano- and micro-electromechanical systems (N/M-EMS) where the standard constructs of classical physics do not always hold true. So far most of the work conducted on reduced contact scales has been focused on friction, however with novel measurement and modelling techniques established in recent years, nano-wear problem has been attracting more attention and interesting results are becoming available.

4.1 Fretting damage

Fretting is considered as a specific type of reciprocating sliding. It is defined as a small displacement amplitude oscillatory motion (usually induced by vibrations) between two nominally stationary solid bodies in contact under normal load. Depending on the loading conditions (displacement amplitudes, normal loading) fretting causes damage by surface fatigue or wear induced by debris formation. Fretting is indeed a complex process and not all the kinetics and mechanisms are well known. Collins defined more than 50 factors that influence fretting [60] and more factors are still being added [61].

Two major test configurations have been developed for fretting experiments (Fig. 19):

- fretting fatigue configuration, derived from a classical fatigue test where two pads are pressed on the fatigue specimen. Relative displacement (δ) and cyclic tangential load (Q) are induced by the strain generated through the fatigue part subjected to external loading. In this configuration crack nucleates and then propagates due to applied external loading.
- fretting wear configuration, where contact load is generated by a relative motion between two bodies induced by electro-dynamic shaker or hydraulic system. This configuration is usually applied to analyse wear process due to micro-displacements in a classical reciprocating wear test.

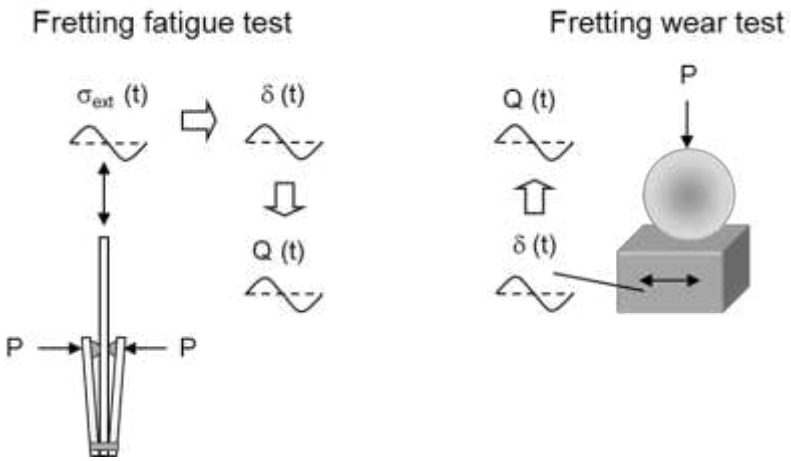

Figure 19: Fretting test configurations

The most established fretting test configuration used in fretting wear experiments is ball-on-flat one. In such configuration, the ball is subjected to normal load (P) or rotational load (Pr), Fig. 20, and three fretting modes can be distinguished [62]:

- linear displacement (mode I)
- radial displacement (mode II)
- circumferential displacement (mode III)

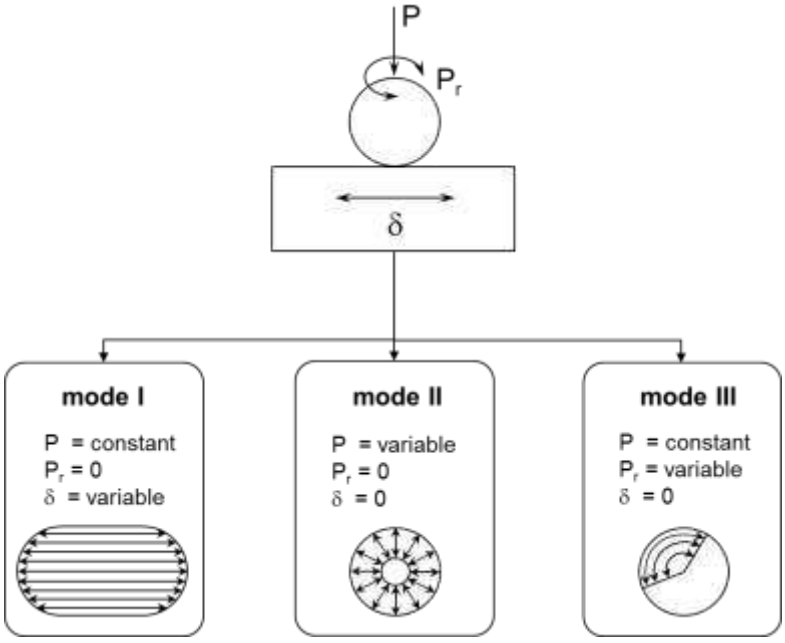

Figure 20: Three basic fretting modes with representative displacement tracks

Most published research is focused on fretting mode I because the wear and friction mechanisms in that case are described by similar laws as sliding friction. However, other modes are also encountered in industrial applications and need to be investigated as well. The fretting mode II occurs in mechanical systems such as ball bearings or electrical contacts while fretting mode III can be observed in the specific areas of heat exchangers or steam generators.

Literature sources quote different values of displacement amplitudes as a border between the fretting process and reciprocating sliding motion. This value is variously interpreted and contained within a wide range of amplitudes, typically between 50 and 300 μm for classical macro-scale experiments [63-66]. Although it is possible to limit the relative displacements between particular elements of mechanical systems by means of engineering measures, it is nearly impossible to eliminate fretting entirely, as this kind of degradation was reported even for displacement amplitudes less than 1 μm [67-68]. The upper limit of fretting regime can be determined using the coefficient introduced by Fouvry S. et al. [69], which is defined as a sliding ratio:

$$e = \delta g / a$$

where:
δg – sliding amplitude, which is different from the displacement amplitude due to the contact and testing device compliance;
a – contact radius.

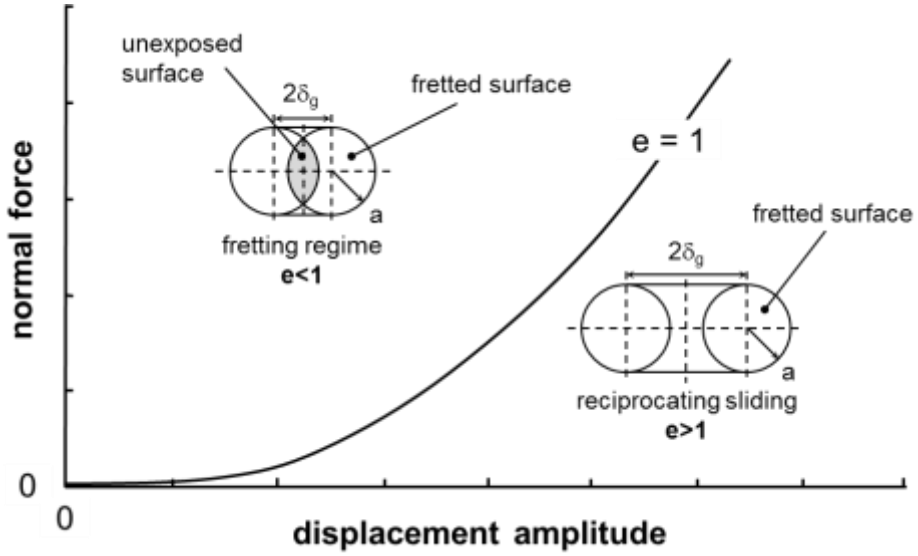

Figure 21: *Definition of sliding ratio "e" and identification of transition between fretting regime and* reciprocating sliding motion (contact sphere/plane), [after 69].

The tribo-system remains in the fretting regime when the unexposed surface is maintained at the centre of the fretted surface (e < 1). The system moves into reciprocating sliding regime when the centre of contact area is becoming exposed to the atmosphere (e > 1).

Small scale fretting

Analytical tools for nanoscale materials have rapidly developed over the last three decades, improving resolution and efficiency of existing techniques and enabling development of new tools. Starting with the invention of the Scanning Tunnelling Microscope in 1981, various experimental methods based on Scanning Probe Microscopy (SPM) have revolutionised many areas of science and engineering by offering a wide range of resolution from the subatomic level up to few hundreds of micrometers. Among various SPM techniques, Atomic Force Microscopy (AFM) has contributed to the opening of a new chapter in the field of study of interaction of surfaces in relative motion at small scales, allowing for precise tests to be carried out under ultra-low loads and minute sliding distances. Nevertheless, it has been also shown [70] that AFM techniques are not fully suitable for testing MEMS applications as they offer much smaller sliding speeds compared to the real MEMS devices. This is where other novel micro-scale mechanical testing methods fill the measurement gap, which has been identified between conventional tribometers and AFM techniques (Fig. 22) [71].

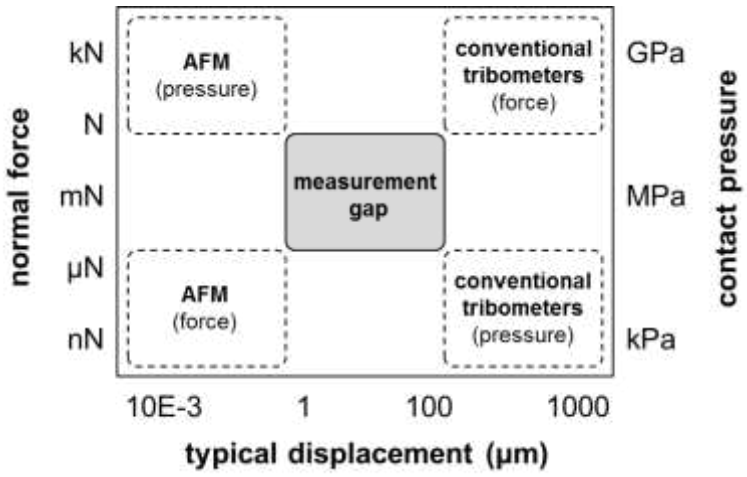

Figure 22: Measurement gap between conventional tribometers and AFM techniques as function of normal force, displacement amplitude and contact pressure [after 71].

Following the nanotechnology definition, nanotribology is typically defined as a branch of tribology that deals with wear dimensions of less than 100 nanometres. Currently, there is no formal nano-fretting definition available, however based on nanotribology description and sliding ratio criterion introduced by Fouvry et al. [10], nano-fretting can be defined as: "Small displacement amplitude oscillatory motion between two nominally stationary solid bodies in contact under normal load, with the unexposed surface maintained at the centre of the fretted surface resulting in wear depth of less than 100 nanometers." This definition is limited to mode I fretting regime, however it can be easily adapted to modes II and III by modifying the aspect of unexposed surface area within the wear track. Although this definition captures the nature of nano-fretting regime clearly, most of the current literature claiming to report nano-fretting results would probably not fit into it. For the purpose of simplicity, these types of experiments are described as small scale fretting in this book chapter although they could also be described as nano/micro-wear for example.

Small scale fretting data have been reported by several research groups carrying out experiments on various, commercially available and purpose-built equipment. Varenberg et al. studied partial and gross slip fretting behaviour of 3.1 μm diameter scanning probe microscopy probes tested against Si wafers [72]. A substantial increase of the coefficient of friction was noted at the transition between partial and gross slip fretting regimes by testing a range of sliding amplitudes from 5 to 500 nm. In collaboration with the same research group, Yoon et al. investigated impact of surface roughness and materials combination on fretting wear in a micro-spherical contact using 200 μm diameter spherical tip under 20 mN load and 6.5 μm displacement amplitude [73]. It was found that the materials combination has a greater effect on fretting wear behaviour than surface roughness in this small scale experiments.

Small scale fretting behaviour of monocrystalline silicon for potential application in MEMS devices operating in vacuum conditions was studied by Yu et al. using AFM tips [74-75]. The energy ratio related to the transition from partial to gross slip regime was measured and compared to the same energy ratio observed in classic macroscale fretting. The authors looked also at 2 nm thick DLC coatings deposited on Si(100) and carried out tests against SiO_2 microspheres under vacuum and air conditions [76]. They found that DLC coating reduced significantly adhesion and friction force in air conditions comparing to Si(100) substrate, however wear behaviour was quite similar to that of Si. Wilson et al. focused on C and Cr doped amorphous C films and carried out small scale fretting experiments using a modified nanoindenter (NanoTest) with 300 μm diameter ruby tip under 10-200 mN applied load and 2-14 μm displacement amplitude [77-79]. The authors identified two distinct fretting wear regimes, with classic W-shaped wear scar under low oscillation amplitude and full U-shaped wear scar at larger amplitudes. Finally, micro-wear behaviour of DLC and TiN coatings using microtribometer setup under reciprocating sliding was investigated by Achanta et al., where the wear mechanism and topographical changes within the wear tracks were investigated using AFM analysis [80-81].

Indentation, scratch and small scale fretting on Si

There has been considerable interest in the mechanical characterisation of silicon for many years, however highly complex mechanical and tribological behaviour of silicon-based MEMS technology remains a main challenge. Nanoindentation of silicon has been the subject of number rigorous studies [82-85], but less is understood about its behaviour under more complex mechanical situations. Small scale tribology experiments require high resolution equipment with ultra-low drift, ideally 0.005 nm/s or less, to allow measurements of wear occurring at low contact pressures over periods of 1h or more. Typically AFM methods have been used for such experiments, however this piezo-based technology cannot provide necessary stability for long duration tests [86]. A number of micro-tribometers have been adapted for small scale tribology experiments but these are usually based on cantilevers to measure forces, which do not provide enough stiffness to carry out tests under very low displacement oscillations [87-88]. Hence, nanoindenter platforms have been recently modified for different types of reciprocating testing under milli-Newton range constant or ramped applied normal loads [88].

In [55] such a modified nanoindenter platform was used to perform small scale indentation, scratch and fretting tests on highly polished Si(100) using a 4.6μm sphero-conical diamond indenter. Fig. 23 shows that loading curves in all three experiments followed the same trend below 40 mN applied load. Above that

load, tangential loading in scratch and fretting experiments promoted yield resulting in higher penetration depths. SEM analysis of silicon samples revealed that pronounced lateral cracking observed under scratch and indentation conditions at high loads was absent in fretting tests, suggesting that the accumulation of strain is reduced by the more dynamic wear process. Critical loads observed in the three types of contact are summarised in Table 2.

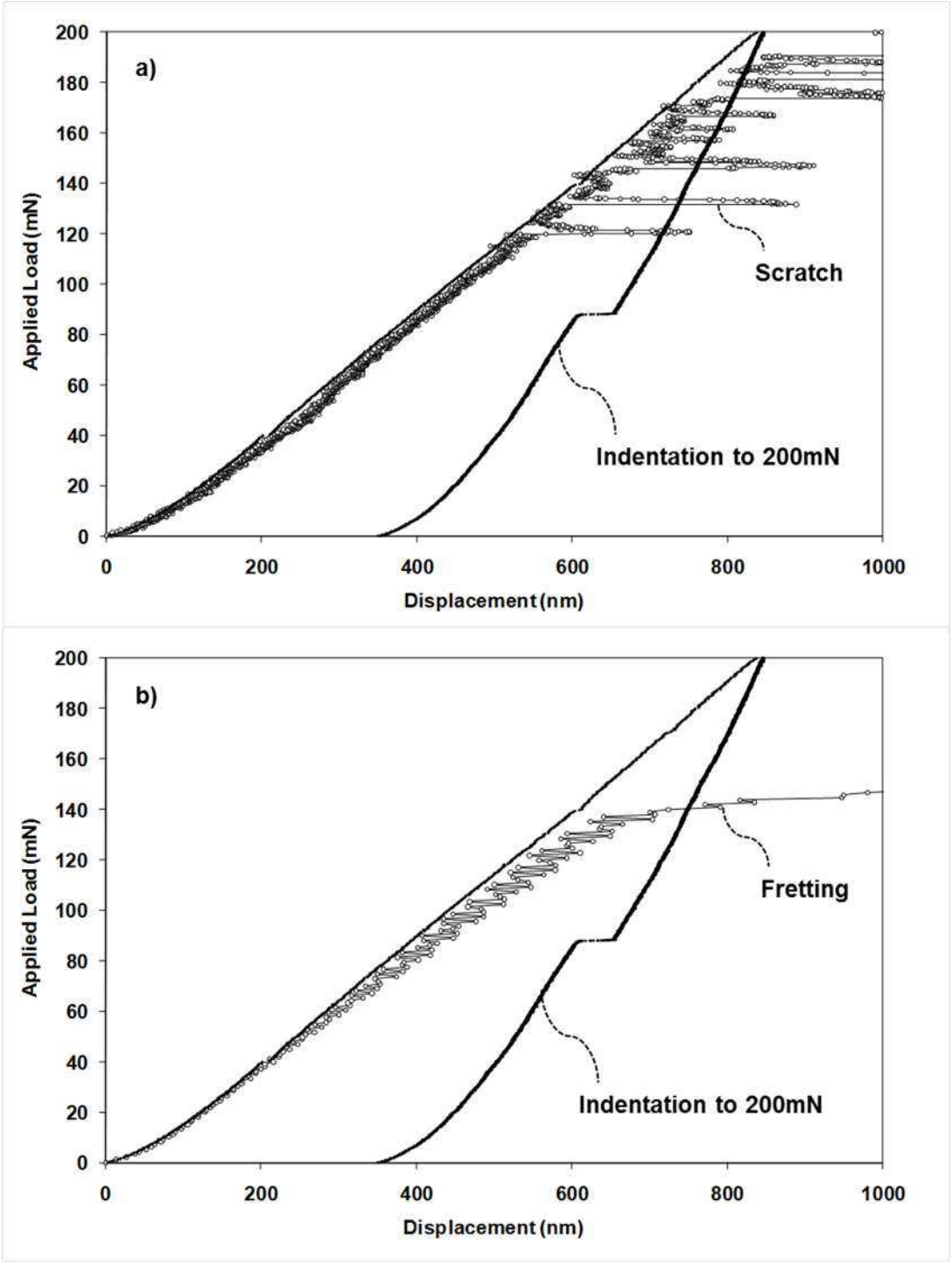

Figure 23: Comparison of loading curves in indentation, scratch and fretting experiments. Test configuration: 4.6 μm sphero-conical diamond indenter against Si(100). [Adapted from 55].

Table 2. Critical loads small scale indentation, scratch and fretting experiments. [After 55].

	Critical load (mN)		
	Indentation	Scratch	Fretting
L_y	40 ± 5	37 ± 5	~30
L_{c1}	~80-95	56 ± 4	*
L_{c2}	>200	106 ± 7	*
L_{c3}	>300	155 ± 16	~100-110

* With the faster speed in the fretting test the L_{c1} and L_{c2} transitions are smeared out and cannot be clearly defined.

In [88] small scale scratch and fretting methods were compared using 10 and 25 μm end radius sphero-conical and Berkovich probes on a range of thin film samples. It was shown that small scale fretting capability is complementary to scratch testing as it offers higher cycle tests with extended duration and significantly lower contact pressure. Table 3 summarizes the key differences between the techniques.

Table 3. Comparison of conditions and contact pressures in small scale scratch and fretting of amorphous carbon films on Si. [After 88].

	Ramped scratch	Repetitive scratch	Fretting
Motion	unidirectional	unidirectional	reciprocating
Probe radius	1-9 μm	1-9 μm	10-25 μm
Wear cycles	1	5-20	To 10000
In situ wear measurement	Yes	Yes	Yes
Contact pressure	8-15 GPa	9-13 GPa	0.1-6 GPa

Small scale fretting of ta-C films on Si

Wear and adhesion limit the practical usability of silicon-based devices and several approaches are being considered to overcome that problem including liquid lubrication [89], solid lubrication with self-assembled monolayers [90] and a variety of thin films [91-93]. In [48] small scale fretting of 5, 20 and 80 nm thickness ta-C films deposited on Si(100) was investigated using spherical indenters. It was found that fretting wear occurred at significantly lower contact pressure than is required for plastic deformation and phase transformation in indentation and scratch experiments. EDX analysis performed across fretting wear scars revealed a reduction in the coating thickness and oxygen incorporation in the worn region. The absence of any abrupt changes in depth or friction showed that deformation proceeded by a fatigue mechanism with a gradual wearing away of the film. SEM analysis also suggested distinctive gross-slip type of damage with scratches generated during sliding present within the fretting wear scar area. The geometry of the wear scars correlated with the loads applied: reduction in wear track length and wider wear tracks were observed with increased load.

Small scale fretting of biomedical materials

Artificial joints are designed as fully lubricated systems, however it has been found that real contact area is only a small fraction of nominal contact area in such devices and asperity-to-asperity contact will occur leading to metallic contacts at microscopic level [94]. Surface scratches observed in retrieved prostheses are typically in the range of few microns wide and less than a micron deep [95], so the mechanical and tribological properties of biomaterials need to be investigated at the relevant contact scale in order to develop reliable artificial joint design. Hence, in [96] small scale fretting experiments were carried out on biomedical grade Ti6Al4V, 316L stainless steel and CoCr alloy samples using 3.7 μm sphero-conical diamond indenter.

Over a wide range of experimental conditions the CoCr alloy exhibited significantly better wear resistance comparing to 316L steel and Ti6Al4V for which wear resistance markedly deteriorated as the fretting load increased. Fig. 24 shows the probe depth under load in the 30 mN small scale fretting experiment during the 290 s at peak load. At the beginning of test 316L steel performed better than Ti6Al4V alloy which was followed by an abrupt increase in probe depth on the stainless steel. This type of behaviour was observed in other tests for Ti alloy and 316L steel but not on the CoCr alloy. Fig. 25 presents the corresponding SEM images, which show that debris on CoCr appeared generally smaller in size while Ti6Al4V and 316L stainless steel showed delamination type of wear. Small scale fretting experiments proved to be a valuable additional tool in this work extending the capability of nanomechanical testing of biomaterials.

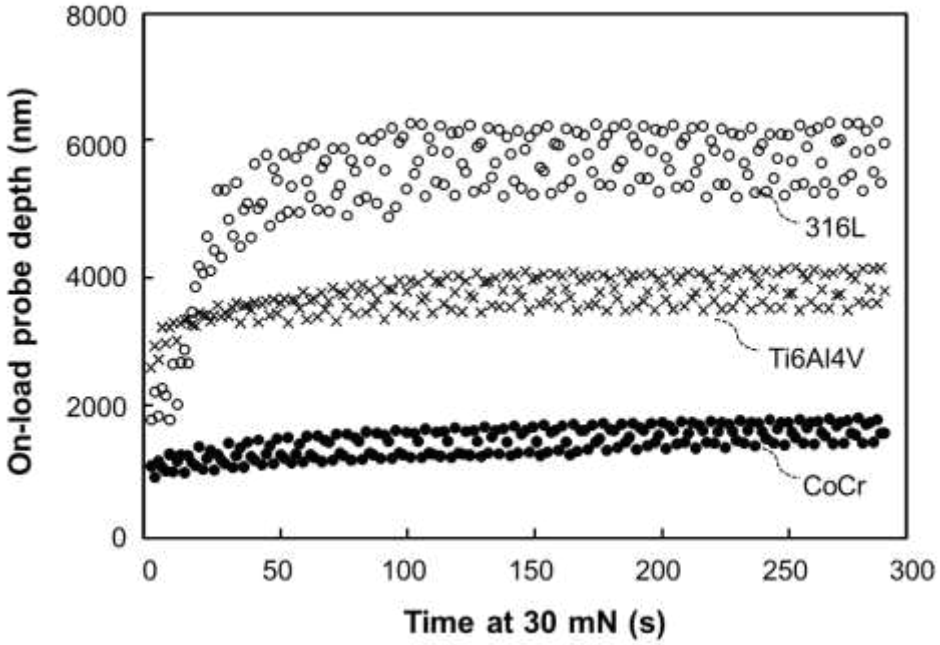

Figure 24: On-load probe depth evolution as a function of 30mN small scale fretting test. [Adapted from 96].

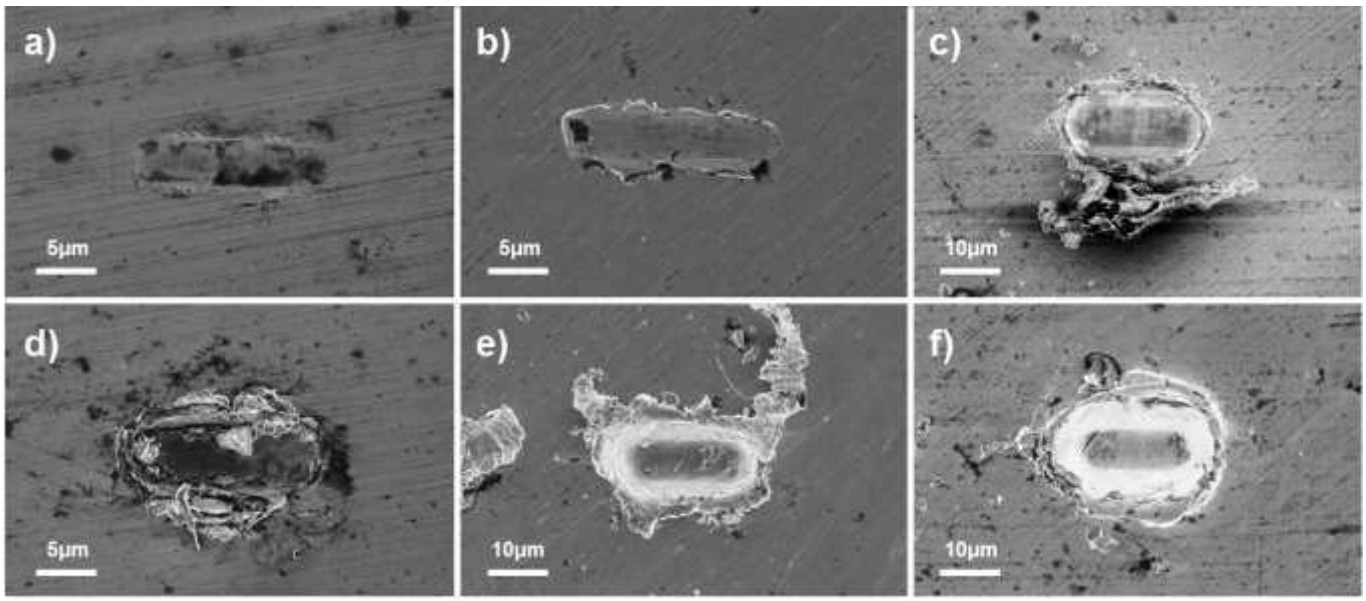

Figure 25: SEM images of small scale fretting scars: a) CoCr alloy under 3mN load, b) Ti6Al4V alloy under 3mN load, c) 316L stainless steel under 3mN load, d) CoCr alloy under 30mN load, e) Ti6Al4V alloy under 30mN load, f) 316L stainless steel under 30mN load. [Adapted from 39].

5. Nano-impact

In many engineering systems materials are subjected to high strain rate deformation. Examples include interrupted cutting (milling), contact between valve-train components in internal combustion engines and collisions between air-borne particulates and gas turbine blades [26,27,52,97-99]. The ability to simulate the relevant in-service contact conditions is highly desirable in the development of materials for these applications and the nano-impact technique is increasingly being used for this purpose.

Nano-impact works by subjecting the sample material to either a single or repetitive high strain rate contact with a test probe. Experiments can be closely defined, the user having control over a wide range of parameters:

- probe material and geometry
- force with which the probe is accelerated towards the sample
- distance over which the probe is accelerated

- either a single or repetitive contact
- if a repetitive contact is used, the frequency of the contacts and the total experiment time may be controlled

5.1 Single impact tests

Single impact experiments are typically used to determine the "dynamic hardness" of a sample [100-101]. This is the effective hardness of the material at a given rate of strain. The dynamic hardness is determined by the quantity of energy absorbed into the deformed material volume at the contact site. The required data for this calculation are provided by a penetration depth vs. time trace which is recorded over a very short time period (typically <0.2 s) as the impact takes place. From these data the incoming and outgoing velocity of the indenter are determined as is the maximum depth reached. A dynamic hardness value will almost always be higher than the quasistatic hardness value for any given material. This is due to the extremely short contact duration between the probe and the sample meaning that minimal time-dependent deformation can take place.

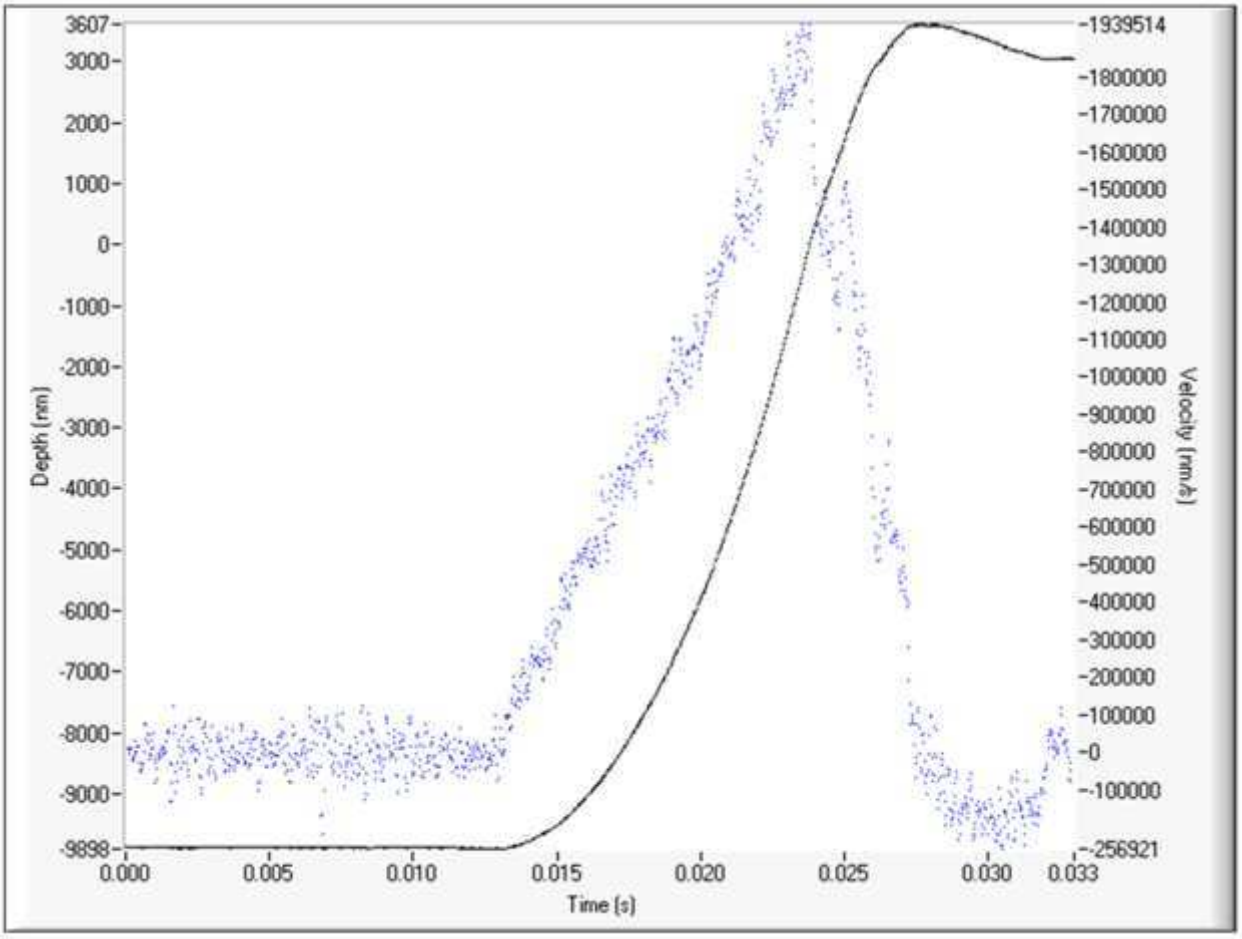

Figure 26: Time–displacement and time–velocity data from a single impact event on Ti6Al4V. The data show the acceleration of the indenter, the contact with the sample, the deceleration of the indenter and the first rebound of the indenter.

The above data were gathered from a single impact experiment on a Ti6Al4V alloy. The dynamic hardness in this test was 8 GPa compared with around 5 GPa under quasi-static conditions. Constantinides and co-workers reported [101] that gold was even more sensitive to strain rate but aluminium was much less so (Table 4).

Sample	Quasi-static H (GPa)	Dynamic H (GPa)
1100 aluminium	0.27	0.29
annealed Au	0.48	1.3
work hardened Au	0.80	2.8

5.2 Repetitive impact

Repetitive impact tests are typically used to assess the ability of a sample to resist failure due to fatigue. The technique is essentially comparative and allows samples to be ranked in terms of their performance under the test conditions. As in the single impact test, the resulting data take the form of a penetration depth vs. time trace, but a typical time frame may be 60-300 seconds. Cross referencing the depth vs. time data with optical or atomic force microscopy of the impact site can reveal a great deal about the cause and mode of failure(s). A popular application of the repetitive nano-impact test is to test coating properties at high strain rates and to investigate surface fatigue and fracture due to repetitive contact, often with the aim of using results to design and optimise the coating properties for improved durability in interrupted contact situations [26,27]. In practice there is usually a direct correlation between increased fracture resistance in the nano-impact test and longer lifetime in the application.

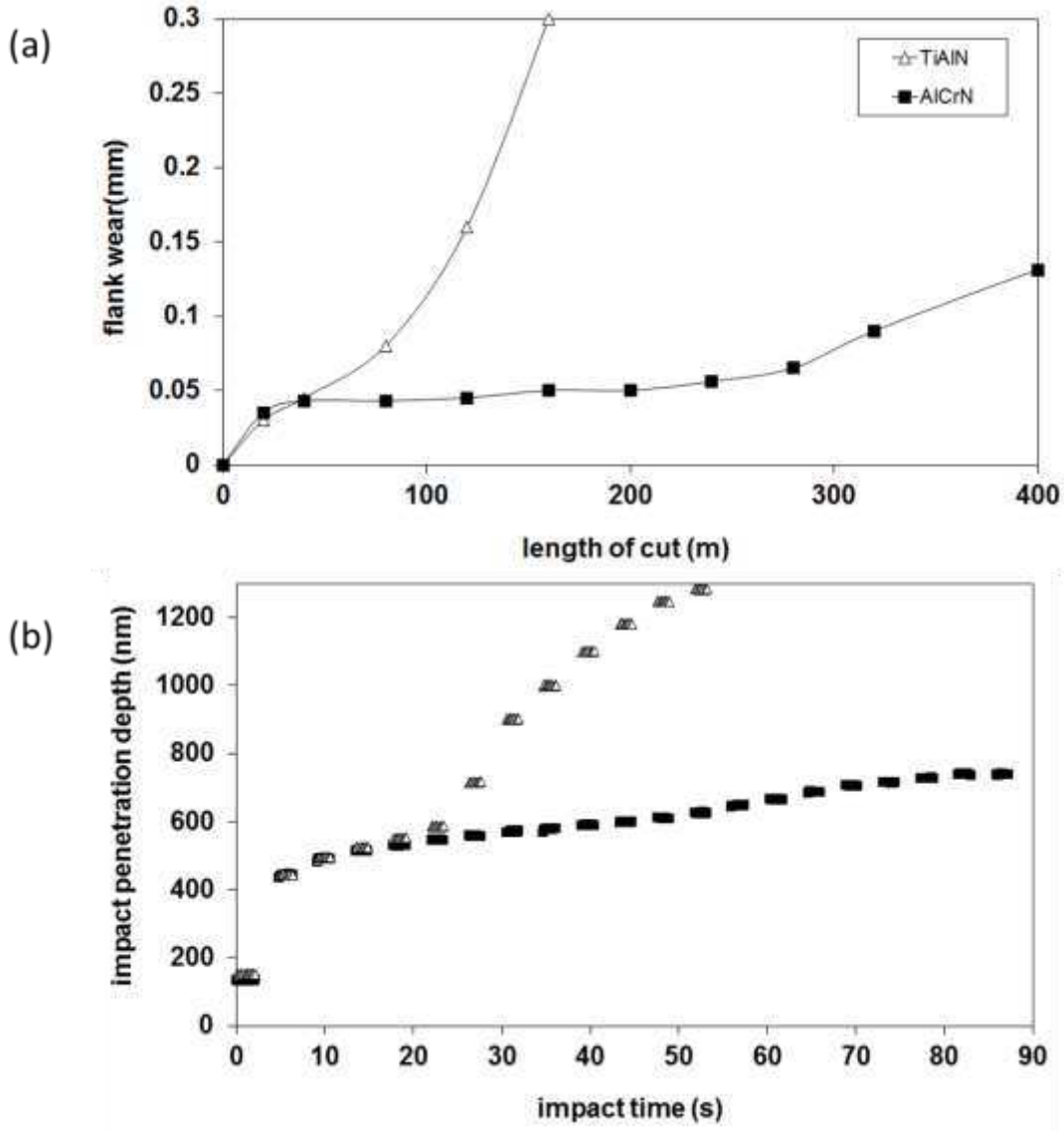

Figure 27: Comparison of the performance of TiAlN and AlCrN coatings in (a) cutting test (b) nano-impact test

This correlation can also extend to the temporal evolution of the impact wear. For example, figure 27 reveals the strong similarity between the evolution of tool wear in cutting of 1040 structural steel and the progression of coating damage on repetitive nano-impact testing. With its lower plasticity index the TiAlN fractures more extensively in the nano-impact test. Plotting data as fracture probabilities allows for the stochastic nature of the impact fracture process to be investigated [102].

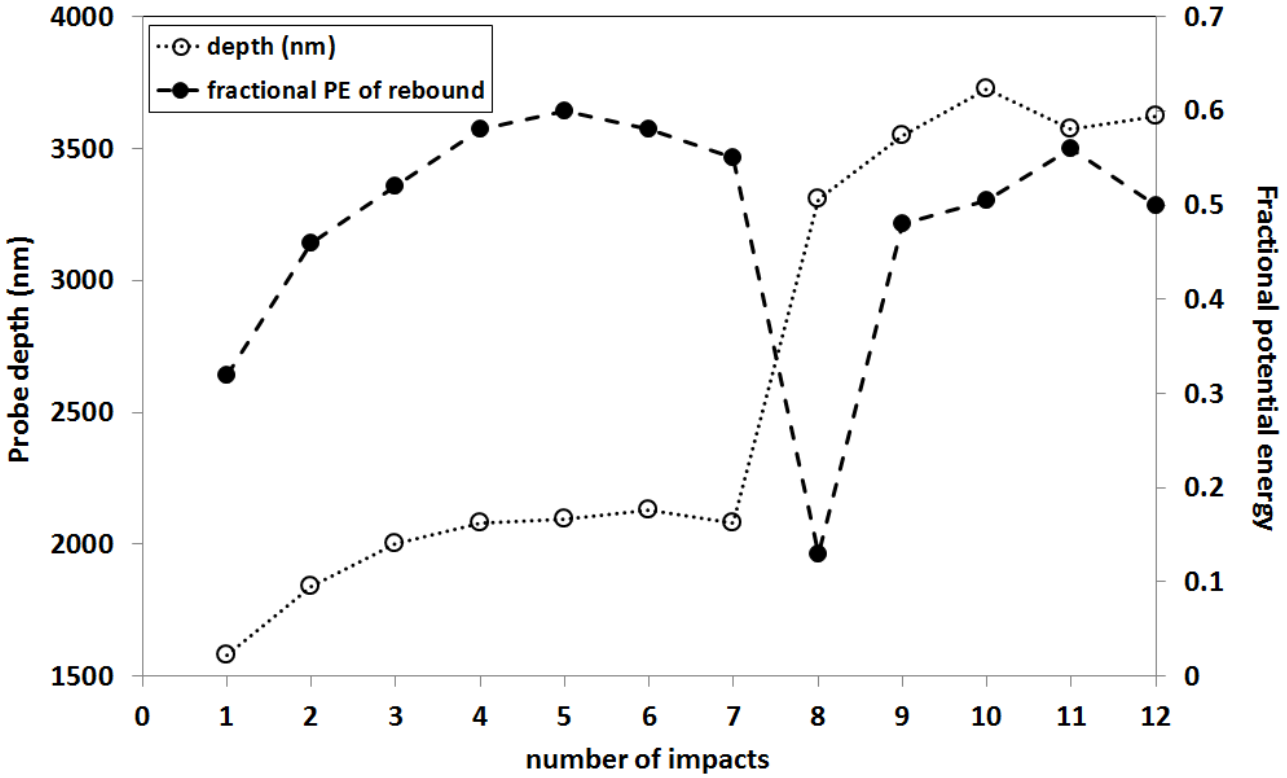

Figure 28: Correlation between fractional potential energy and probe depth in the repetitive impact test [after 103]

Typically the depth evolution is gradual, with periodic abrupt increases in probe depth being due to fracture. Using a NanoTest modified for fast data acquisition Jennett and Nunn showed that there were clear differences in the energy absorbed when fracture occurs [103]. Figure 28 shows repetitive impact data on fused silica at 8 mN with a cube corner diamond indenter. It clearly shows that the impact resulting in a large abrupt change in depth is correlated with enhanced energy absorption. Recently the nano-impact behaviour of a $Ti_{0.4}Al_{0.6}N$ coating was simulated with a three-dimensional finite element model by Bouzakis and co-workers [104]. The model used the failure of constrained tied nodes to simulate crack formation and propagation as the plastic strain develops and exceeds the coating failure strain. The developed nano-impact FEM-simulation was able to predict the film failure initiation and evolution with repetitive impact with a cube corner indenter at 10-50 mN impact force. With spherical probes at low impact forces so that plasticity is suppressed, a backward depth evolution can be observed (i.e. the on-load probe depth decreases with continued impacts) [105,106]. This atypical behaviour has been confirmed by post-test AFM imaging of impact scars showing volume uplift and has been interpreted as due to interfacial delamination without (or before) the accompanying fracture that results in the increase in depth. Faisal and co-workers reported that in the repetitive impact of 100 nm DLC film on Si the geometry of the impact probe influenced the deformation with a conical indenter resulting in delamination but Berkovich resulting in fracture.

The following example shows the relative impact resistance of two TiO_2 coated stainless steel samples. Both stainless steel substrates have been sand-blasted, and one of them was subsequently given a heat treatment process before deposition of the TiO_2. Each test was 5 minutes in duration and during this time 75 repeat contacts were made at 0.25 Hz, the indenter being allowed to contact the sample for 2 s then removed from the sample for 2 s.

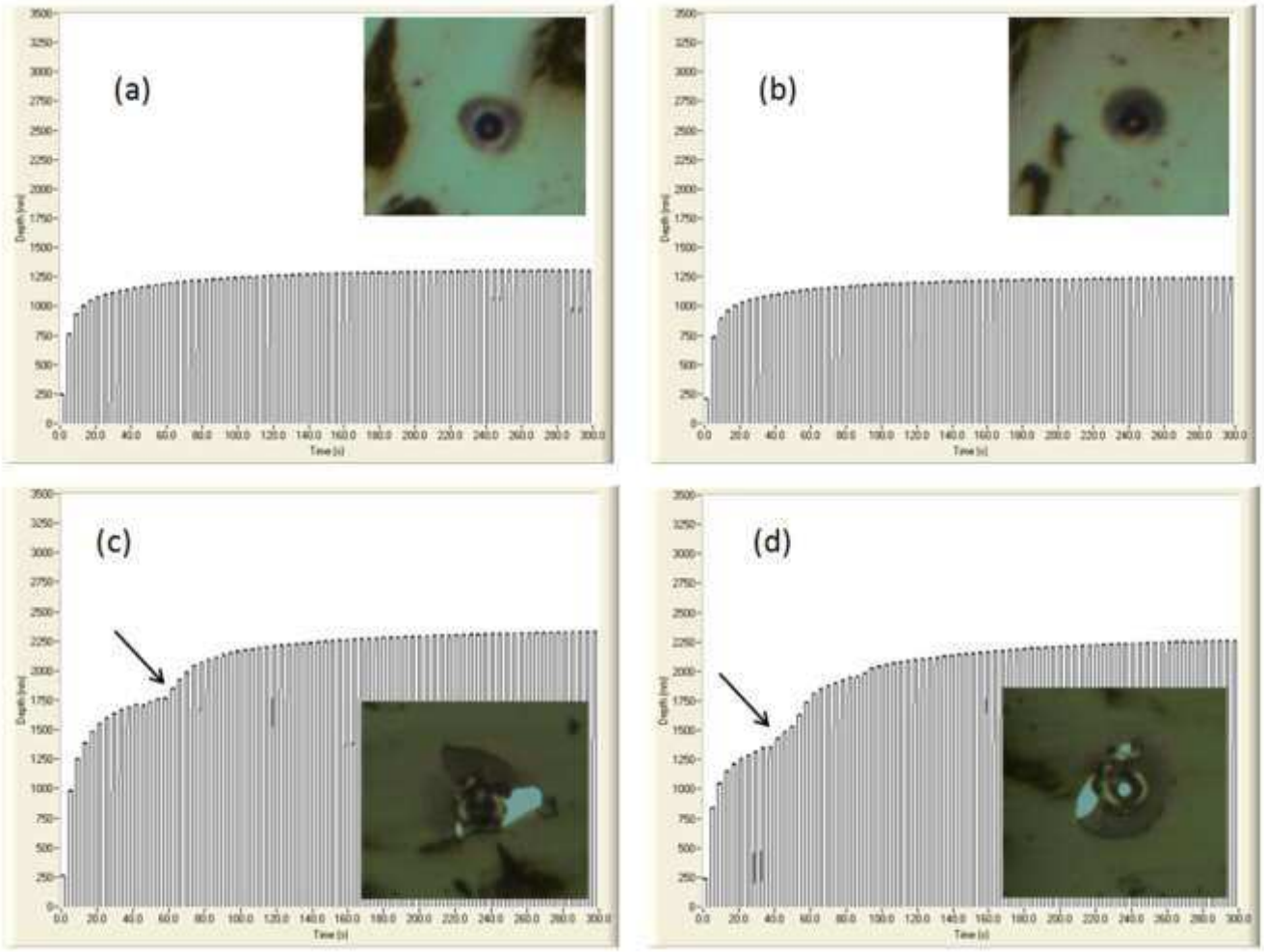

Figure 29: Illustrative repetitive nano-impact depth vs. time traces and optical microscopy of TiO_2 coating on (a and b) heat treated sand-blasted stainless steel substrate and (c and d) and sand-blasted stainless steel substrate without prior heat treatment

The effect of the heat treatment of the substrate is clearly evident in the depth vs. time data and the microscopy. Depth "jumps" and regions of exposed substrate are visible in Fig 29 a,b. The heat treatment was shown to improve the resistance to failure. The smaller maximum depth attained suggests that the improvement was likely to be due to an increased hardness of the substrate helping to provide a better load support for the coating.

The nano-impact test has been used to assess the influence of the deposition of thin interlayers of Ni or Cr (15-50 nm) before depositing 250 nm Pt-Ir coatings on binder-less cemented carbide tools used for precision glass molding [52]. Using a cube corner probe it was found that on coatings without interlayers the probe depth continued to increase dramatically as the repetitive impact test progressed but coatings with interlayers were signficantly more impact resistant. The best impact resistance was shown by a Pt-Ir coating with a 50 nm Cr interlayer where after initial plastic deformation the probe depth remained approximately constant to the end of the test.

Bouzakis and co-workers have performed detailed investigations into the influence of post-deposition wet micro-blasting on cutting performance of PVD coated tools, supporting their tool life data with nanomechanical testing and FEM [107-109]. Micro-blasting induces compressive stresses which can be beneficial in reducing wear although the results are dependent on pressure and the grain size and geometry of the abrasive materials. For the same micro-blasting conditions and abrasive diameter the abrasion with ZrO_2 is less intense than Al_2O_3 due to the spherical nature of the ZrO_2 [107]. To investigate the influence of the developed compressive stresses on the film brittleness they performed nano-impact tests, finding impressive correlation between the results of the nano-impact tests and the cutting performance when milling hardened steel (AISI 4140) [108].

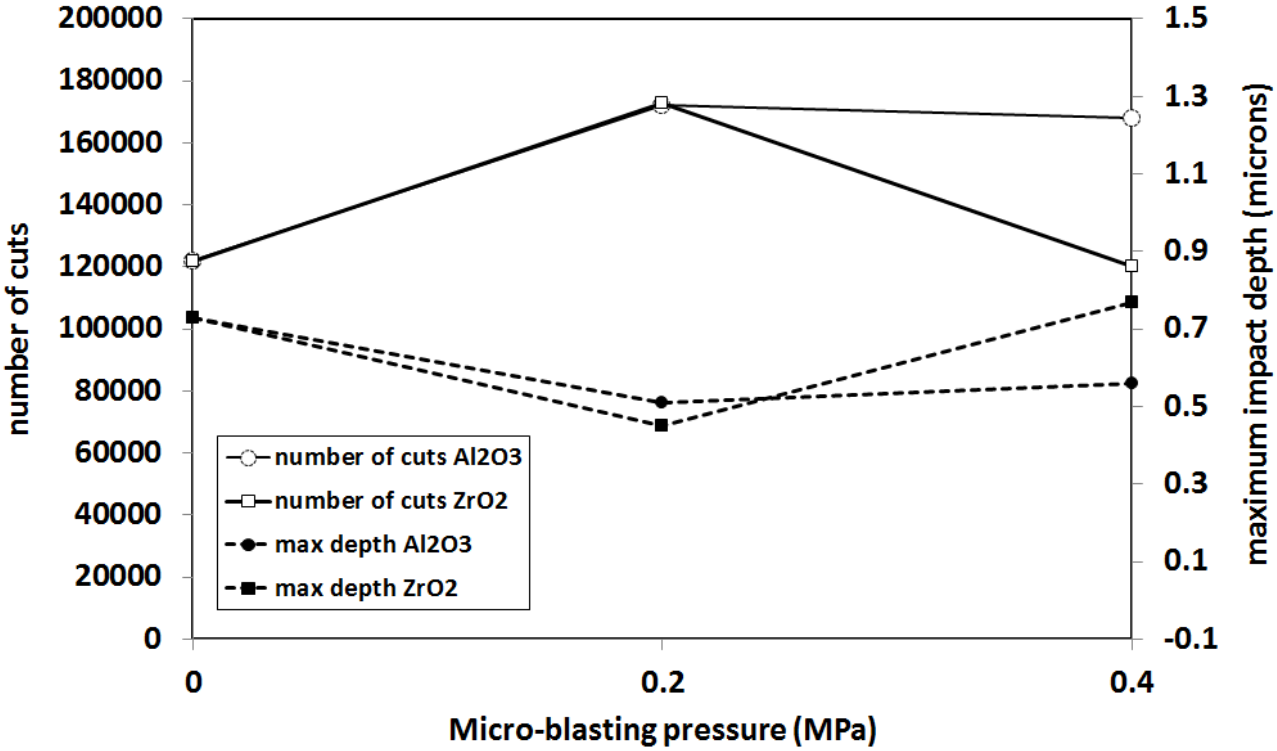

Figure 30: Lower impact depth correlates with greater cutting performance

Figure 30 shows clearly that under these conditions (i) low impact depth (high impact resistance) is strongly correlated with cutting tool life (ii) the trends in tool life with micro-blasting pressure are well reproduced by the nano-impact test (iii) the ranking of micro-blasting with ZrO_2 and Al_2O_3 at a given pressure, and the switch in relative performance between 0.2-0.4 MPa is also shown.

Chen and co-workers highlighted the importance of microstructure on the dynamic impact response in nano-impact of wear-resistant hard TiAlSiN and TiN thin coatings on M2 steel [110]. When the impact load was increased to 10 mN and 30 mN for the monolayer TiN and multilayer TiAlSiN coatings, respectively, cracks started to appear during the tests. At higher loads, spallation was observed in both coatings, although the multilayer TiAlSiN coating showed much less spallation. The improved nano-impact resistance of TiAlSiN coating is considered to be due to its H^3/E_r^2 aiding resistance to crack formation and its multilayer structure helping with crack deflection.

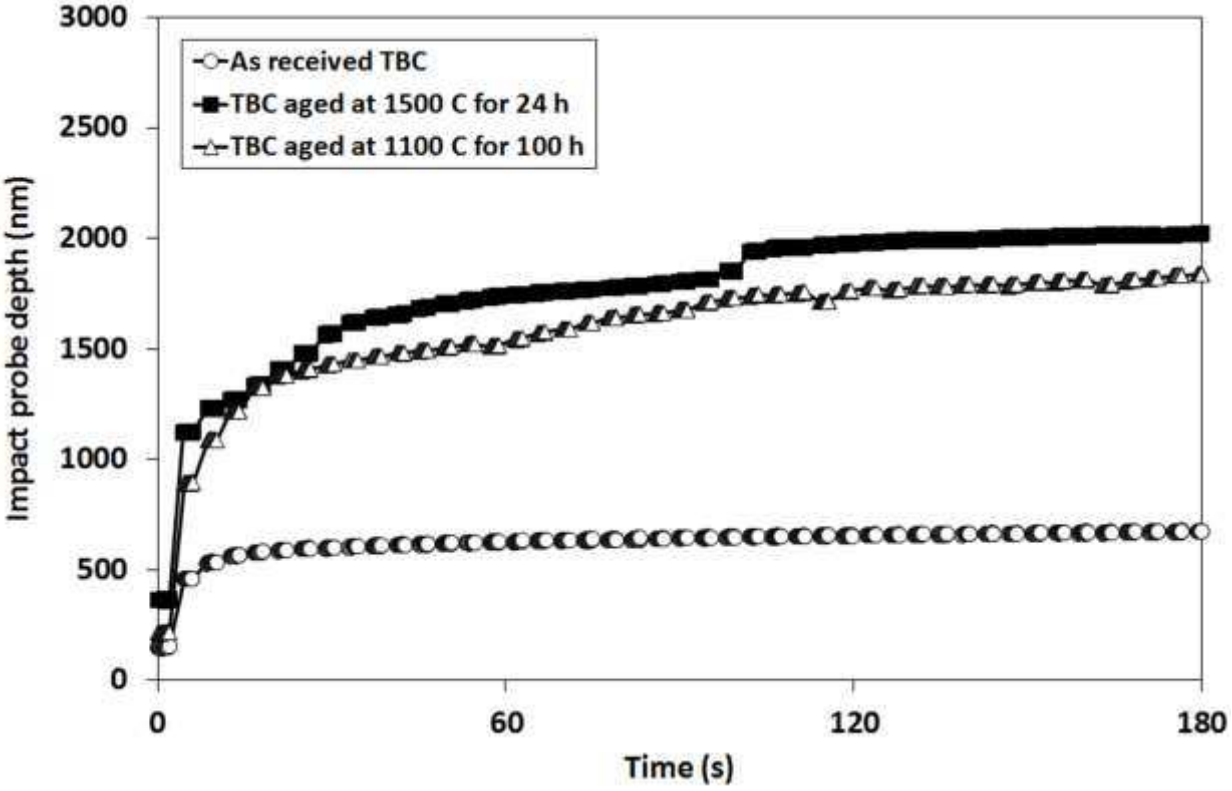

Figure 31: Influence of thermal ageing for 24 h at 1500 °C and 100 h at 1100 °C on the impact resistance of an EB-PVD TBC

Chen et al investigated the role of changing coating microstructure and mechanical properties due to thermal aging at 1100-1500 °C on the repetitive impact and erosion behaviour of 150 µm thick thermal barrier coatings (TBCs) for aero-engines [99]. Thermal aging alters the microstructure and mechanical properties of TBC systems, and there is a clear need to develop a rapid laboratory test method that can assess such changes. Nano-impact provides such a dynamic measurement tool and in this study it has been used to assess erosion resistance. For this application it is superior to conventional nanoindentation as the dynamic strain rates are much higher. Compared to bulk erosion testing it offers the potential advantage of testing on the scale of the individual columns in the TBC, thus measuring individual column and column cluster properties. It is shown that thermal aging resulted in increased hardness and stiffness of the TBC. Nano-impact testing (figure 31) showed the increased wear rate very clearly under these conditions and this correlated well with the measured bulk erosion rate. As repetitive dynamic test producing damage on the correct length scale, the nano-impact test was highly effective in simulating the erosion mechanism and may be used as a rapid screening test to evaluate the erosion resistance. Nanoindentation alone would not be able to predict this.

6. Environmental considerations (hot, cold, fluid, humidity)

Nanoindenters most commonly measure sample mechanical properties within a fairly narrow window of temperature (e.g. 20-25 °C), humidity (RH ~40-50%) and strain rate (~10^{-1}-10^{-3} s^{-1}). However there are many situations where characterisation under these conditions is simply not appropriate and it is more important to measure properties under conditions more reflective of the operating or processing conditions which the test material is to be exposed to. Mechanical and tribological behaviour under these conditions may bear very little relation to that measured at room temperature, quasi-static conditions, and attempting to use data to predict performance under very different conditions can be highly dangerous. Originally nanoindenters could only operate within this confined window of humidity, strain rate and temperature, however, developments over the last 10 years or so have seen rapid progress in expanding the test capability of some commercial instruments. Environmental extremes (high temperature or in liquid) typically act to promote time and temperature dependence which alters the indentation response, taking it either further from or closer to elastic unloading. Careful experimental design is required.

6.1 Influence of moisture and electrochemical potential on nanoindentation behaviour

Performing measurements in controlled humidity conditions requires either placing the entire instrument in an environmental chamber (or modifying its standard operating test enclosure) or designing a small humidity control unit to enclose a much smaller volume immediately in the vicinity of the sample. An example of the former approach was by Altaf and co-workers who recently used a NanoTest with its test enclosure fitted with a humidity control unit to study the effect of moisture on a commercial stereolithography polymer resin, Accura 60, over a wide humidity range (33.5-84.5% RH) [111] (Altaf et al. 2012). Mechanical properties of stereolithography resins such as Accura 60 are affected by the level of moisture in the environment, with hardness and modulus decreasing with increased moisture uptake in the resin. Transport of moisture from the surface to the bulk of the polymer took place sufficiently slowly that a coupled stress-diffusion FEA was required to accurately model the behaviour. Gravimetric tests were performed to calculate the diffusion constants and bulk tensile, compressive and creep tensile tests to generate the mechanical material properties for the model. With appropriate modelling, the variation in hardness with (i) increasing penetration into the interior of the polymer (ii) different environmental conditions could be accurately simulated.

Measurements under fully hydrated conditions require both sample and indenter are fully immersed in a dedicated liquid cell [112-114]. A consideration when measuring a very highly compliant sample in a fluid environment is the buoyancy of the indenter and measurement head components. Any change in buoyancy throughout the measurement, although small can be significant when the sample material is so easily deformed. In the NanoTest the indentation direction is horizontal; as the indenter penetrates the sample surface the submerged volume of the loading head remains constant (due to it moving horizontally in the fluid) and as such constant buoyancy is maintained.

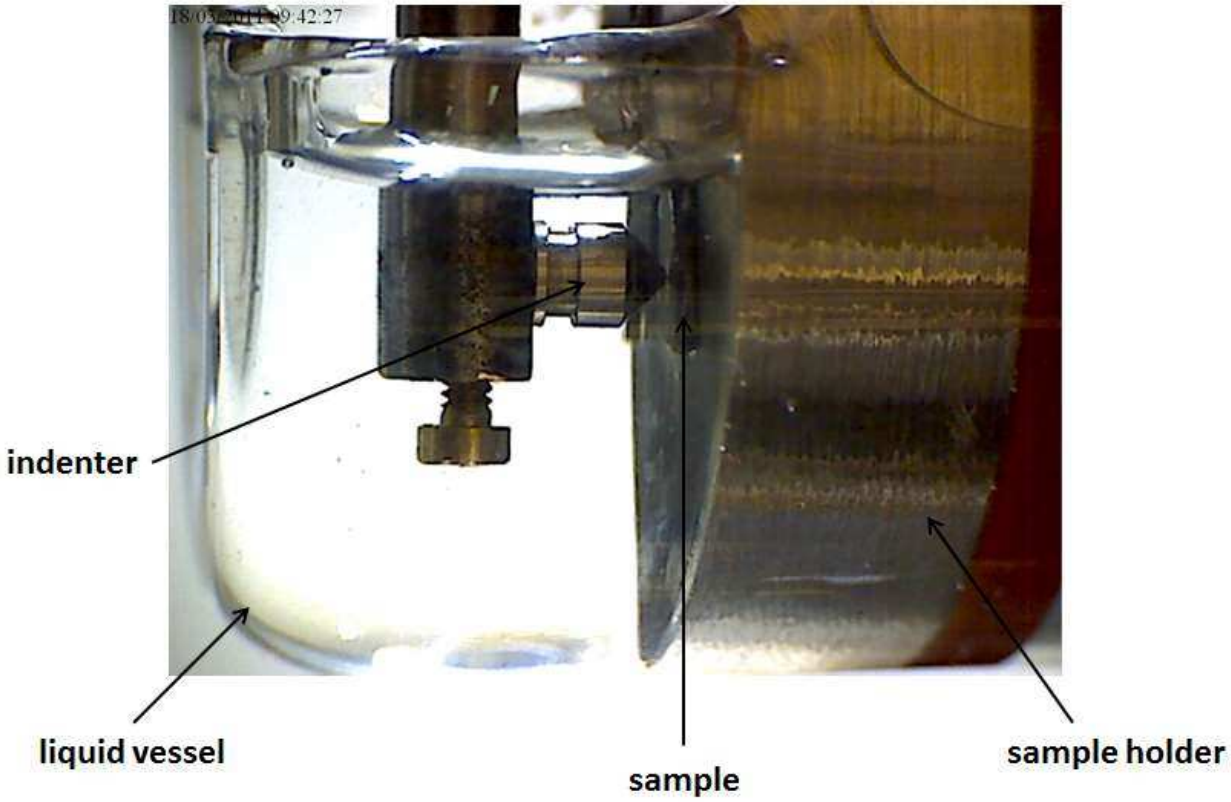

Figure 32: The configuration of a commercial liquid cell (NanoTest)

Nylon-6 samples with ~30-35 % crystallinity were tested by Bell and co-workers in fully hydrated (deionized water) and ambient laboratory (50% RH) conditions using the cell design in figure 32 [113]. After equilibration (>24 h) the hardness and elastic modulus measured in deionized water were significantly lower (50% and 60-70% respectively) than those measured in ambient conditions. The strain rate sensitivity parameter, A/d(0), where A is a constant determined by fitting to experimental data and d(0) is the depth at the start of the hold period at peak load, decreased significantly in water. The reduced proportion of time-dependent deformation in deionized water is consistent with a reduction in the tan delta peak due to a shift in the glass transition temperature when wet. Using a NanoTest fitted with a recently designed humidity cell, Harris and co-workers [115] were able to more rapidly measure the moisture sensitivity of the hardness

and stiffness of a similar nylon sample over the humidity range 20-95 % RH. Figure 33 shows the variation in elastic modulus with humidity.

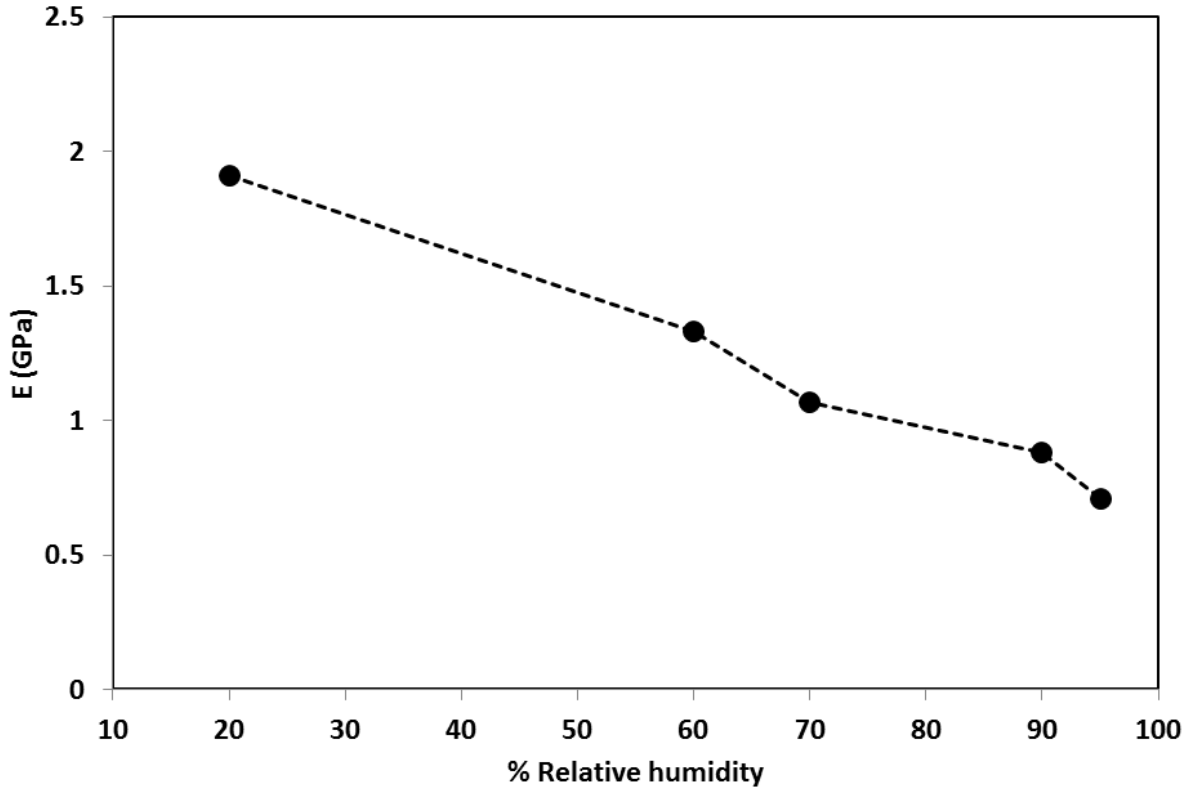

Figure 33: Influence of humidity on the elastic modulus of nylon

Making measurements in fully hydrated conditions is particularly useful in the characterisation of biological materials. Constantinides and co-workers [114] found the stiffness of PAAm-based electrophoresis gels decreased by a factor of about 1000 when hydrated (E(gel, water) = 270 kPa; E(gel, air) = 300 MPa). Even larger changes have been observed for polyethyleneimine hydrogel. When indented in its dry state this polyethyleneimine hydrogel exhibits a reduced modulus of almost 18 GPa, after 30 min water immersion this has fallen by a factor of ~5000 to 3.3 MPa.

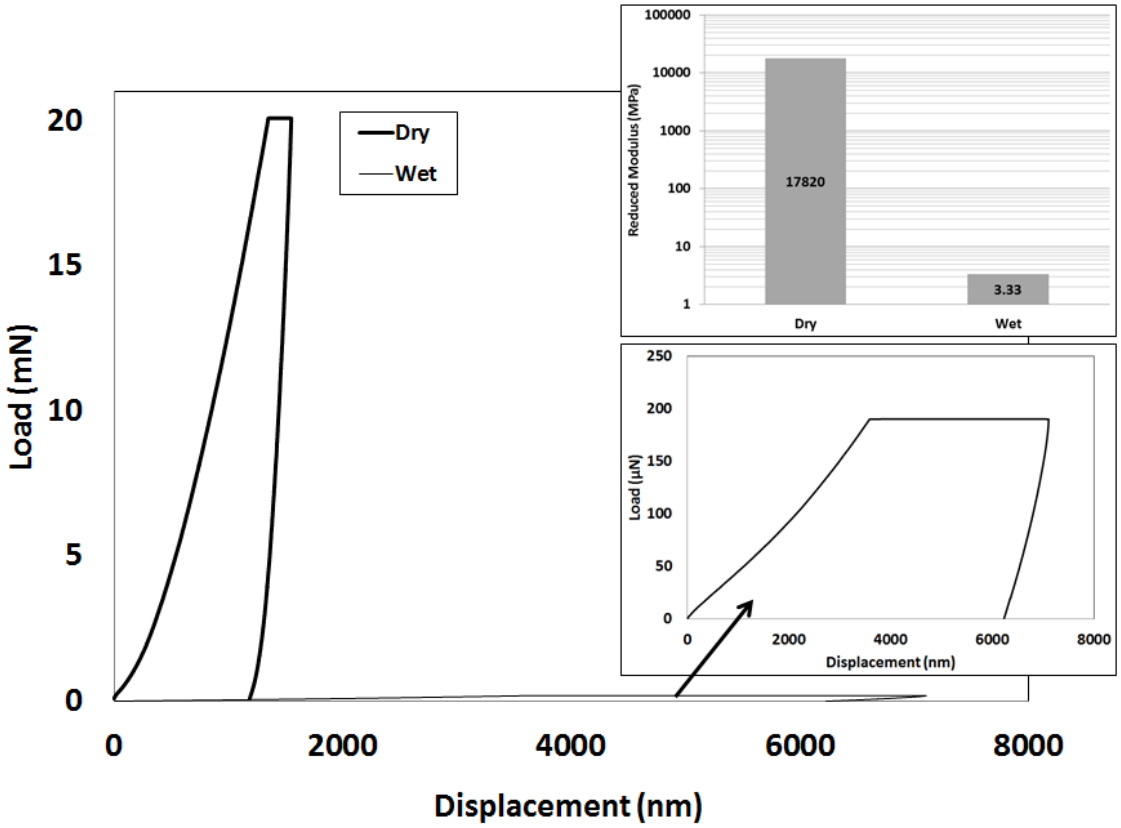

Figure 34: Indentation behaviour of a polyethyleneimine hydrogel in fully hydrated and ambient air.

Schmidt and co-workers used a NanoTest modified to act as a electrochemical cell to study an electroactive polymer nanocomposite thin film containing cationic linear poly(ethyleneimine) and 68 vol % Prussian blue nanoparticles as a candidate stimulus-responsive polymer material [116]. Electrochemical reduction of the Prussian blue particles doubled their negative charge causing an influx of water into the film to maintain electroneutrality. This resulted in swelling and a decrease in elastic modulus. The in situ nanoindentation measurements using a spherical ruby indenter of 5 µm radius showed a reversible decrease in the elastic modulus of the film from 3.4 GPa to 1.75 GPa.

6.2 Nano-scratch and nano-impact testing in liquid

The ability to perform nano-scratch tests under liquid has many biological and biomedical applications. Running nano-scale tribological tests under precisely controlled conditions that in terms of stresses, contact size, test environment are close to those in vivo can provide valuable insight into the underlying deformation mechanisms. As an example, abrasion on retrieved CoCrMo hip joints has been reported to be due to third-body wear by detached hard particles in vivo. The presence of small scratches around 10-20 µm wide suggests contact with sharp asperities. To understand the tribology of the scratch formation it is necessary to perform tests at the relevant scale rather than rely on bulk testing. Sun and co-workers have used nano-scratch testing of cast CoCrMo to simulate single-asperity contact with a small hard carbide particle [117]. Using a NanoTest fitted with a liquid cell they performed tests at 37 °C in 0.9% NaCl using a 10 µm diamond scratch probe at 200 mN. They found that even single scratches could produce significant microstructural changes in both the Co-rich matrix and the hard carbides. They were able to reproduce various features such as slip lines, matrix fracturing and the formation of nanometric and rhombic grains on the periphery of the scratch that have been found on retrieved MoM cups.

Kalcioglu and co-workers at MIT used nano-impact in liquid to evaluate the high strain rate behaviour of fully hydrated tissues from liver and heart and candidate tissue surrogate materials, quantifying their resistance to penetration under energy densities relevant for tissue surrogate applications [118]. The energy strain densities in the tests were 0.4-20 kJ/m^3 which is broadly comparable with macroscale impact tests designed to replicate ballistic conditions (15-60 kJ/m^3). They reported that the energy dissipation capacities of fully hydrated soft tissues were well matched by a 50/50 triblock/diblock gel composition.

6.3 Measuring high temperature mechanical properties by nanoindentation

The ability to measure mechanical properties of materials at in-service temperatures has great value. High speed cutting tools experience temperatures of >500 ˚C in operation due to frictional heating and thermal barrier coatings for turbine blades can be required to operate at 1000 ˚C or higher. The high temperature properties of the materials used in such applications cannot necessarily be predicted from room temperature testing. Elevated temperature nanoindentation can provide the engineer with invaluable information to help to optimise material properties for their applications. Much progress has been made in high temperature nanoindentation over the past 10 years. Understandably the very small depths typically attained in nanoindentation mean that the technique can be susceptible to “thermal drift” as sample and/or instrument components change slightly in temperature and consequently expand or contract during the test.

Reliable high temperature nanoindentation requires that (i) tests can be performed without thermal drift or other instrumental factors influencing the raw data (ii) the elastic contact mechanics at room temperature can successfully be applied to situations where very significant time-dependent non-elastic deformation may occur (iii) oxidative wear of tip and/or sample does not occur (or if it does, is sufficiently small not to complicate interpretation of the results). Despite some potential drawbacks, as described earlier, fused silica is a popular choice as reference material for high temperature nanoindentation since it is mechanically homogeneous, shows relatively little creep at elevated temperature, it is mechanically homogeneous with elastic properties well characterised by other techniques such as resonance ultrasound, and it has quite low thermal conductivity.

Practice has shown that it is not usually sufficient to only heat the sample before indentation as this produces a large thermal gradient between the hot sample and cold indenter which greatly influences the measured data, particularly on more conductive samples. When a non-heated indenter is used to indent a heated sample heat will conduct onto the indenter from the sample causing indenter expansion. Consequently the

instrument measures a combination of the indenter penetrating the sample and the dimensional change of the indenter thus compromising the experiment. The deficiencies of the sample-only heating approach were recently highlighted by Everitt et al on fused silica and gold [119], Tang and Zhang on Si [120], and Zarnetta et al on a TiNiCu shape memory alloy [121]. These studies reported elevated temperature indentation curves dominated by thermal drift when sample-only heating was used. In the latter publication the authors showed that even loading to peak load at 80 °C in 5 s was insufficient on the shape memory alloy and suggested instead loading in 1s. Even at moderately elevated temperatures very rapid loading appears best approach to at least partially counteract the thermal gradient from the sample and indenter being at differing temperatures [122-124]. Franke and co-workers have studied the temperature dependence of the indentation size effect on copper to 200 °C with a sample-only heating [124]. Drift rates increased by a factor of x70 as the temperature was increased reaching 7 nm/s at 200 °C so the tests were performed very rapidly in an attempt to mitigate against this and no modulus information was reported. Nevertheless, they were able to show that the indentation size effect on copper was reduced at higher temperatures implying thermal activation has a major influence on the length scale for plasticity.

The practical solution to this problem is to separately heat both the indenter and the sample to the same temperature to minimise/eliminate the thermal gradient to achieve isothermal contact. The first report of dual active heating on a commercial nanoindentation system (NanoTest) was by Smith and Zheng in 2000 [125]. Subsequently, this approach has been adopted in around ~60% of high temperature nanoindentation publications, including virtually all of those at over 200 °C. The configuration for this is shown schematically in figure 35.

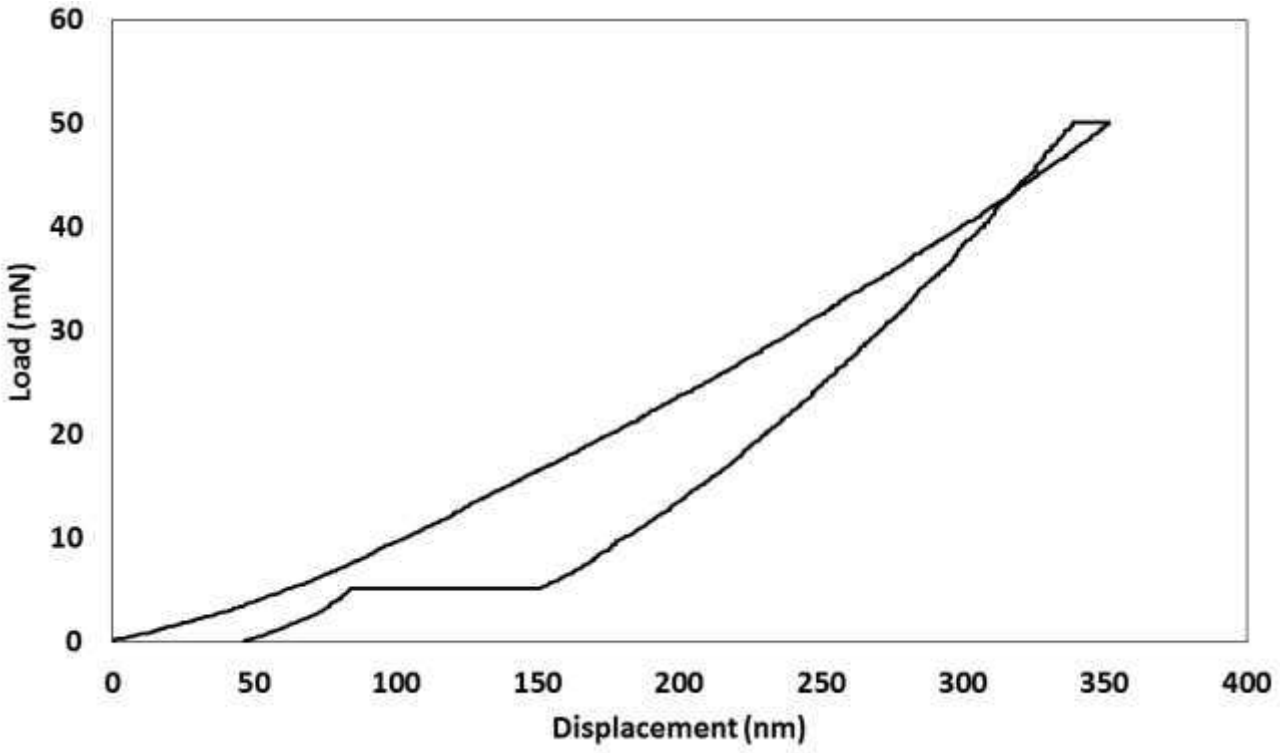

Figure 35: Configuration for dual active indenter and sample heating

Precise temperature control is important. At high temperature even a small thermal differential can compromise the reliability of the experiment. In the example above the indenter was about 5 ˚C cooler than the sample surface (sample temperature 500 ˚C). Heat flow from the sample onto the indenter has caused expansion of the indenter material during the indentation process. The expansion was sufficiently rapid that during the 30 s hold at maximum load we see a reduction in depth rather than the increase we would expect to observe as the material creeps. Unsurprisingly increasing the indenter/sample temperature mismatch increases the drift dramatically. With a difference of about 20˚C initially the depth is seen to increase as the load is applied then, a critical contact area is reached where sufficient heat can flow such that the linear expansion of the indenter is faster than the rate of penetration of the indenter in to the sample material, consequently the measured depth is seen to reduce.

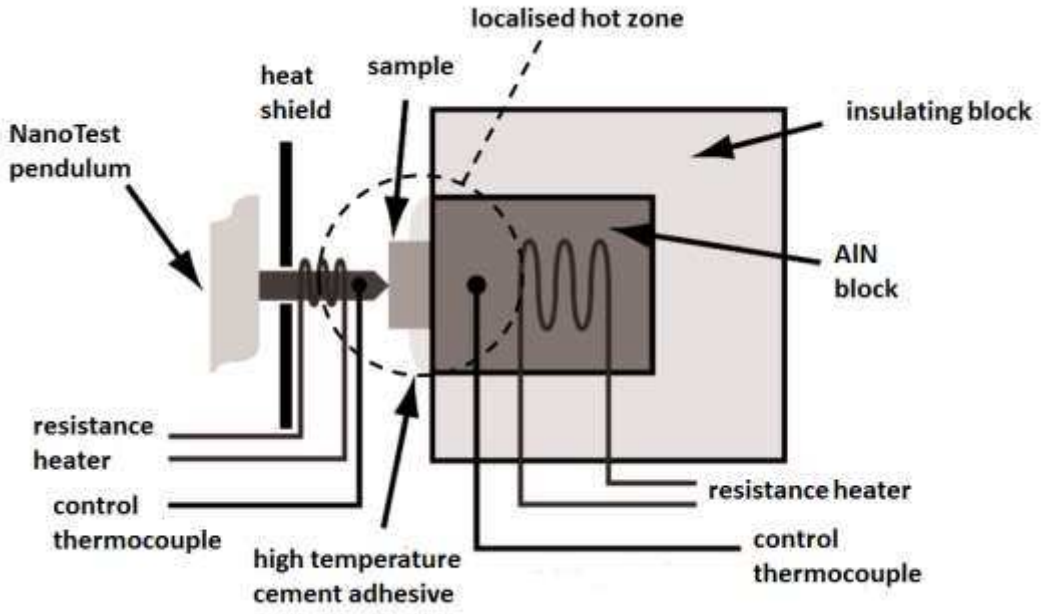

Figure 36: The effect of thermal mismatch between indenter and sample due to poor experimental design

The effectiveness of the method to minimise (or even eliminate) this thermal gradient by heating the indenter and the sample separately to achieve an isothermal contact is improved by precision control. The methodology involves three steps for the indenter heating control side [126]:

i) the indenter is heated to the target temperature by feedback control
ii) once the target temperature is reached the controller measures the average power supplied to maintain the target temperature
iii) the indenter is then supplied with this constant power during indentation

This approach provides more stable temperature control than using PID control for both sample and indenter. Once a suitable indenter has been selected (see below) and the indenter/sample temperatures matched by the above method it is possible to produce measurements of equivalent quality as at room temperature, as illustrated in the following examples. Unless one is familiar with the indentation characteristics of a given sample, it can be difficult to distinguish between high temperature and room temperature load-depth curves. The following example shows indentation data on Si (100) at 500°C and 650°C. This is a critical temperature range for silicon over which appreciable softening occurs.

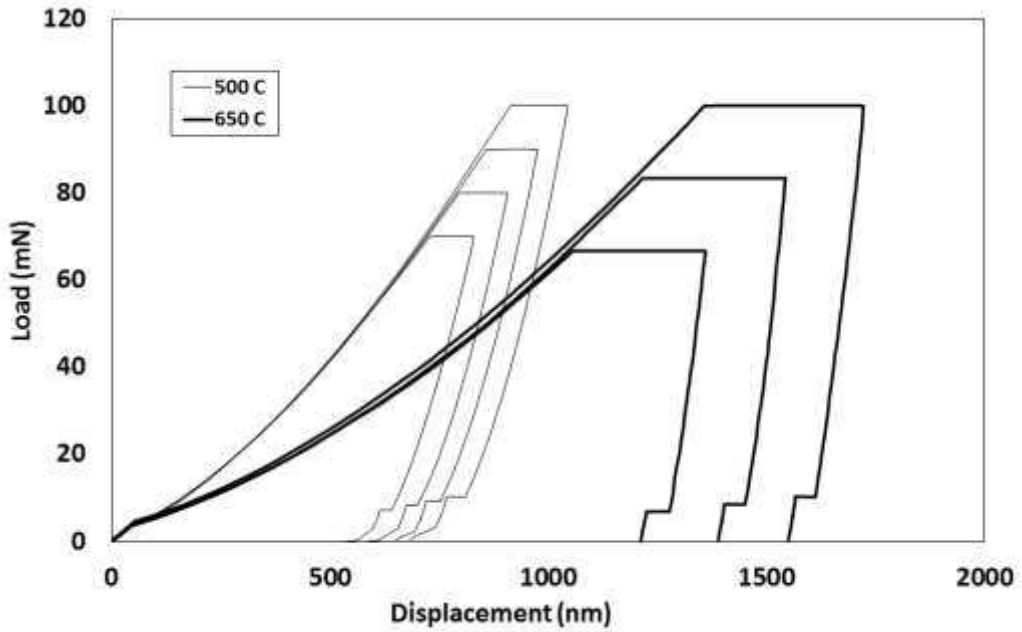

Figure 37: Indentations on silicon at 500°C and 650°C.

The depths achieved at equivalent loads are markedly different as is the degree of displacement which occurs during the maximum load dwell periods.

Materials we consider to be essentially elastic at room temperatures often exhibit increasing visco-plasticity with increasing temperature. This can be highlighted by either applying the indenter load at different rates or by examining the sample deformation under constant load.

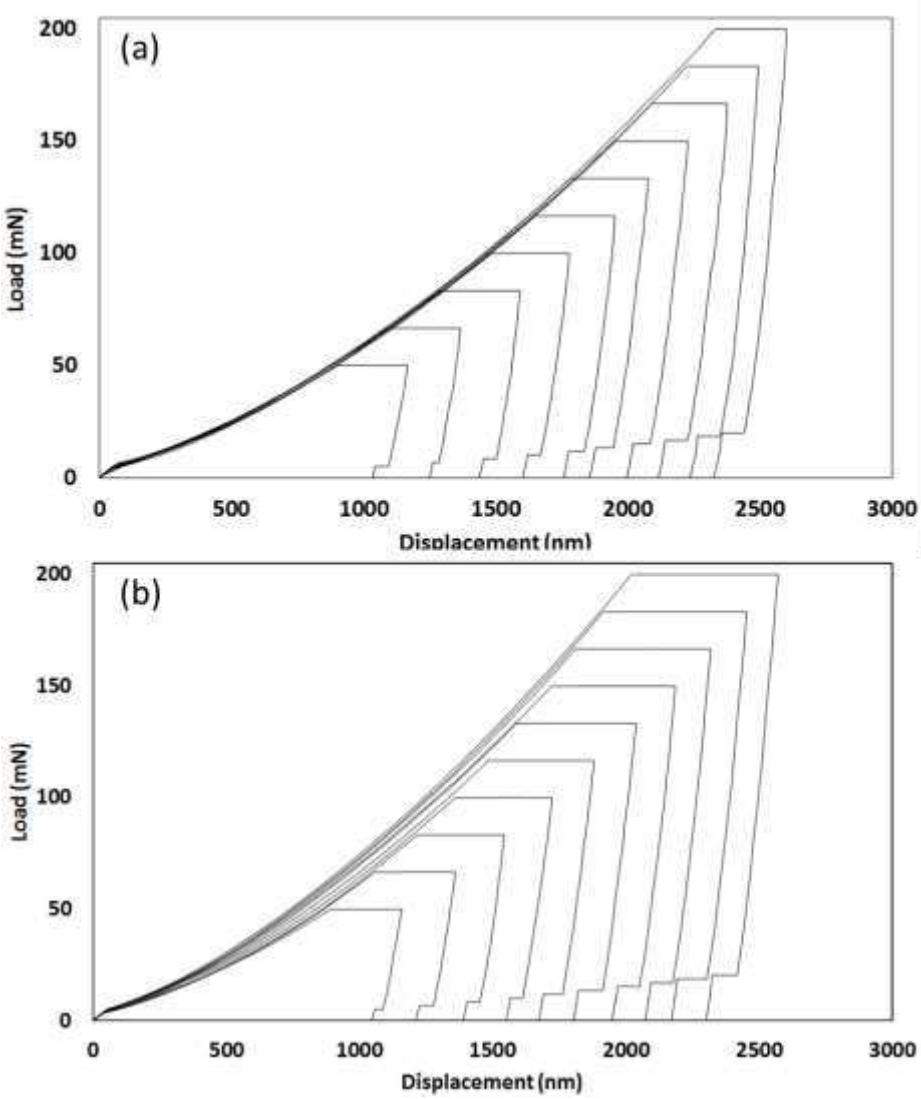

Figure 38: Constant loading time and constant loading rate indentation on Silicon at 650 °C

In this example silicon has been indented under two loading conditions; (a) using a constant loading rate and (b) a constant loading time. In case (b), as the loading time for each indentation was constant the loading rate used increases as a function of the target maximum load, i.e. the highest load (200 mN) indentation was loaded at 40 times the loading rate of the lowest (5 mN) indentation. The effect of this is that the loading curves do not superimpose as the time dependent element of the sample's deformation plays an incrementally smaller role in the overall deformation measured. Contrast this with case (a) where the loading curves are seen to superimpose.

Tribochemical interactions between indenter and sample

Indentation at elevated temperatures can put a greater demand on the indenter material and consequently care must be taken to select the right indenter material for the sample to be measured if premature blunting of the tip is to be avoided. Blunting of the tip can be caused by (i) oxidation of the indenter material (ii) dissolution of the indenter material into the sample (iii) accelerated wear at temperature due to indenter softening. Oxidative degradation can be eliminated by running indentation experiments in a vacuum environment. Suitable apparatus does exist in a number of cases but in addition to cost the integration of nanoindenters into vacuum environments can be challenging as the instruments are susceptible to vibration

from pumps and many electronic components found on such instruments are not vacuum compatible. However, where successful integrations exist they can sustain indenter and sample at extreme temperatures (up to about 800 °C) for extended periods of time with little or no degradation. Purging the instrument environment with and inert gas such as Argon can be effective at maintaining a sample in a measurable state. An example of where this can be effective is when cobalt bonded tungsten carbide samples (coated or bulk) are to be tested at temperatures over 500 °C. In air rapid oxidation of the cobalt binder can occur to such a degree that the sample can expand to several times its starting volume. Whilst a purge does not eliminate completely oxidation of such samples it does provide sufficient working time to gather indentation data at temperatures above 700 °C.

Carbon is soluble in iron and ferrous alloys. The rate at which it will dissolve increases dramatically with increasing temperature. For this reason a diamond indenter should never be used with such samples as it can be completely degraded in a very short period of time. Sapphire or Cubic Boron Nitride (cBN) are suitable alternative materials for ferrous alloys at elevated temperatures. However it should be noted that both of these materials have their own limitations. Sapphire is, relative to diamond (H ~100 GPa) quite soft (about 30 GPa) and indeed in many cases can actually be softer than the sample material – cutting tool coatings for high speed machining applications can often be over 30 GPa hardness at room temperature. Furthermore, sapphire does not retain its hardness sufficiently to be a viable alternative for measurement of hard coatings at elevated temperatures. It does remain a good option though for softer materials such as metals and thermal barrier coatings. cBN is much closer to diamond hardness (about 70 GPa). It also retains this hardness well at temperature. The limitations with this material stem mainly from the form in which it is available and any strength limiting defects which may exist within its microstructure. Typical single crystal cBN sizes are less than 0.5 mm in any dimension. This presents difficulty in manufacturing for the perspectives of securing the crystal in its holder and achieving the preferred orientation. Despite the difficulties this material presents it is possible to produce thermally and chemically stable indenters which are able to undertake measurements not possible with either diamond or sapphire.

(Ti,Al)N coatings for cutting tools – role of annealing at 700-900 °C

Coatings have been successfully applied to cutting tool inserts to prolong tool life in machining applications. Trends currently driving the development of new coatings include (i) cutting faster to increase productivity (ii) “green-machining” - cutting without coolant for environmental reasons and (iii) machining hard-to-cut materials. To achieve long tool life under these conditions coatings need to be multifunctional and display several interlinked characteristics to minimise wear. For applications such as these involving high temperature due to frictional heating the mechanical properties at the operating temperature are more relevant than those measured at room temperature.

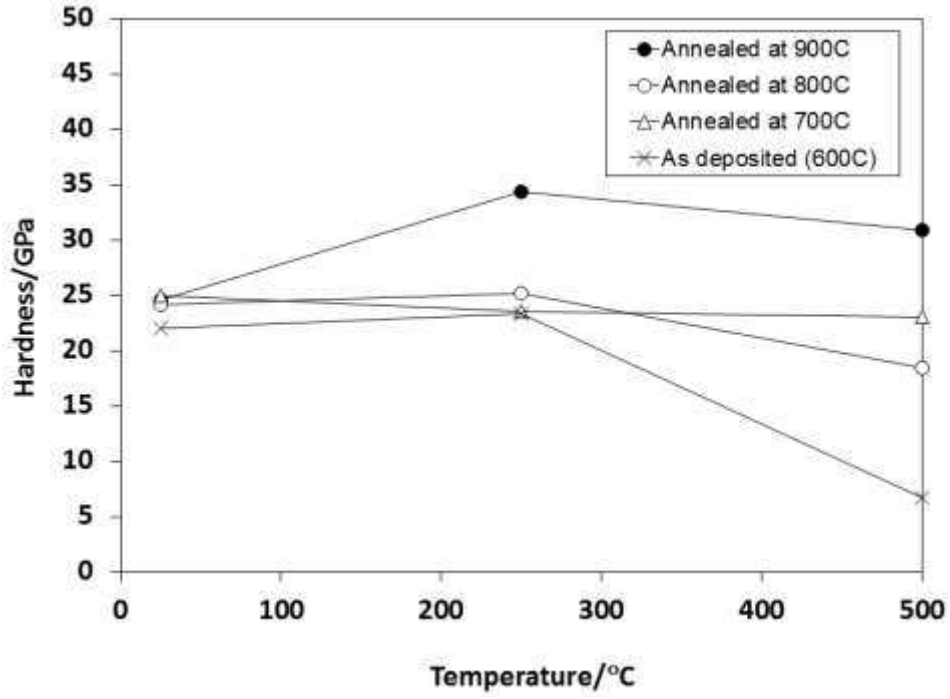

Figure 39: Variation in hardness with temperature of as deposited AlTiN and AlTiN after annealing for 2 hr in vacuum at 700-900 °C

The example below illustrates how annealing coatings can alter their mechanical properties and cutting life. The post-deposition annealing of an Al0.67Ti0.33N (AlTiN) coating, deposited at approximately 600 °C, for 2 hr in vacuum at 700-900 °C has a dramatic effect on its high temperature mechanical properties [127, 128]. Figure 39 shows the variation in high temperature hardness with annealing temperature. Without prior annealing the hardness of AlTiN increases slightly at 250 °C before decreasing at 500 °C. Bouzakis and co-workers also reported a complex dependence of hardness vs. temperature for a (Ti,Al)N coating with similar composition (Ti0.34Al0.66N), with a pronounced increase at 150-200 °C interpreted as dislocation pile up due to strain hardening [129]. Using dual-heating in the NanoTest [129] they recently reported on the high temperature nanoindentation of a 3 µm TiAlN coating on WC-Co with high (0.5 µm) surface roughness. The standard deviation and coefficient of variation versus temperature were determined to assess the reliability of the data. The scatter in the indentation depth at 15 mN was unsurprisingly higher than if the sample had been mirror polished but it increased only minimally as the temperature was increased from 25 to 400 °C.

The influence of the changes of the AlTiN coating mechanical properties from annealing (shown in figure 39) on the relative life of coated cutting tools in different high speed machining applications has been studied. The machining operations were continuous high-speed turning of 1040 structural steel, interrupted turning of 4340 steel and end milling of H13 hardened steel. Annealing at 700 °C was found to improve tool life in all these conditions compared to the as-deposited coating. However when the annealing temperature was increased to 900 °C its effectiveness depended strongly on the cutting conditions. The longer tool life in high-speed turning of 1040 structural steel after annealing AlTiN at 900 °C has been attributed to the combination of high temperature at the tool/workpiece interface and relatively low stresses at the cutting zone. Under these conditions temperature-induced processes dominate on the surface of the tools and tool life is predominantly controlled by its hot hardness. In contrast, in interrupted cutting conditions toughness and plasticity appear more critical. In end milling high hot hardness and yield stress should be combined with improved plasticity and high temperature fracture strength for longer tool life. After annealing at 900 °C the resultant AlTiN coating does not display an optimum balance of these properties. Annealing at 700 °C gives the AlTiN coating optimum combination of properties for the interrupted cutting tests. It shows the best adaptive behavior with a combination of mechanical properties that provide a more stable environment for tribo-films to form and grow in interrupted cutting conditions than the coating after annealing at higher temperatures which display lower plasticity.

Fuel Cell materials

Solid oxide fuel cells (SOFC's) are an increasingly popular high efficiency form of energy conservation. Key to their performance and reliability is an hermetic seal which separates the fuel and air sides of the cell. SOFC's operate at around 800˚C and at this temperature creep of the hermetic seal material can lead to early failure. The following example shows how the rate of deformation under a fixed load (creep) of a glass-ceramic fuel cell seal material increases with increasing temperature [130]. High instrumental stability is required to undertake such measurements reliably.

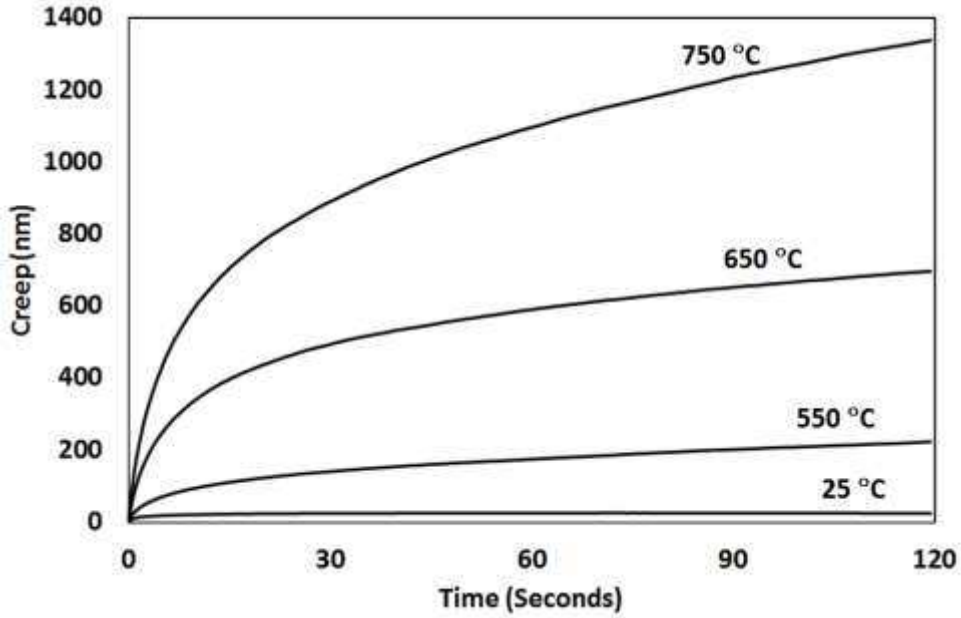

Figure 40: Influence of temperature on indentation creep of a glass-ceramic fuel cell seal material

In the same study, the glass-ceramic seal material was subjected to a thermal "pre-ageing" process with the objective being to improve stability of high temperature mechanical properties. Hardness and elastic modulus measurements were undertaken at 750˚C. The measurements were carried out in an air environment and a cBN indenter was used as it would not oxidise at the testing temperature. 100 hours of thermal ageing results in the glass-ceramic exhibiting a smaller drop in elastic modulus with increasing temperature. As such the ageing process enhances the material's sutability for the SOFC seal application.

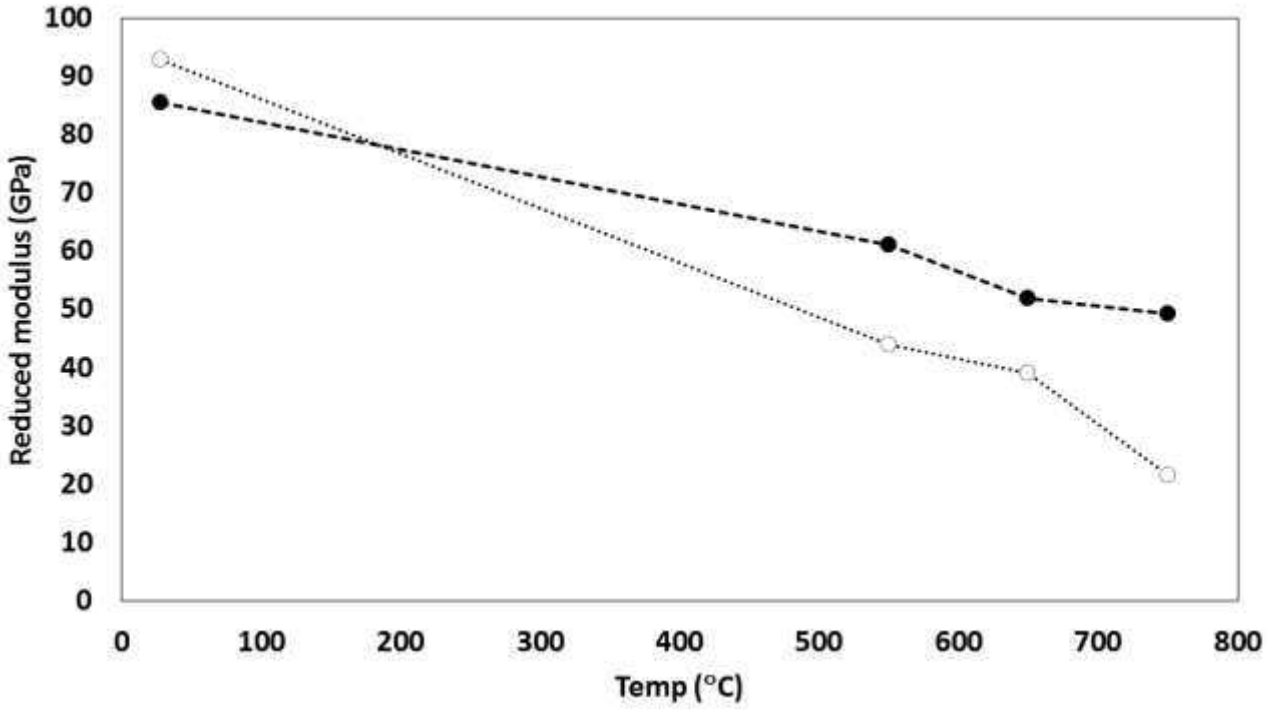

Figure 41: Influence of temperature on the elastic modulus of a glass-ceramic fuel cell seal material previously thermally aged at 800 °C for 4h (open circles) or 100h (closed circles)

6.4 Non-ambient temperature nano-scratch and nano-impact testing

6.4.1 High temperature nano-scratch and friction testing

In many engineering applications frictional heating results in a local increase in the temperature between contacting surfaces and in high speed dry machining temperatures may be 1000 °C or more. For convenience macro-scale scratch and wear testing of coatings is almost always performed at room temperature with unknown heating due to friction. A promising alternative approach is to perform

mechanical and tribological tests with temperature control using heated stages and more moderate loads. Micro-scratch and micro-wear tests on wear-resistant coatings have been performed to 600 °C using R = 25 µm diamond probes to apply loads 0.5-20 N. He and co-workers investigated the low load sliding of silver-bismuth alloys from room temperature to 280 °C [131]. Depending on the alloy composition they observed either (i) a sharp decrease in friction on melting, or (ii) a general increase in friction with increasing temperature.

Diamond oxidises in air above ~500 °C, so the use of alternate indenter materials are required to extend the temperature range for applications such as high temperature solid lubricants, thermal barrier coatings and cutting tool coatings that require higher temperatures. In a more recent study Smith and co-workers used a WC-Co probe was used to study nanoscale friction on a range of TiN-based coatings at 25, 400 and 750 °C [132]. The tests were performed at very low contact pressure so that the ploughing contribution to the total measured friction, usually the dominant term at higher contact pressure, was minimised and the interfacial friction could be measured directly. A maximum in friction coefficient was observed at 400 °C (figure 42). The decrease in friction at 750 °C was associated with formation of lubricating surface oxides and oxidation-associated surface roughening.

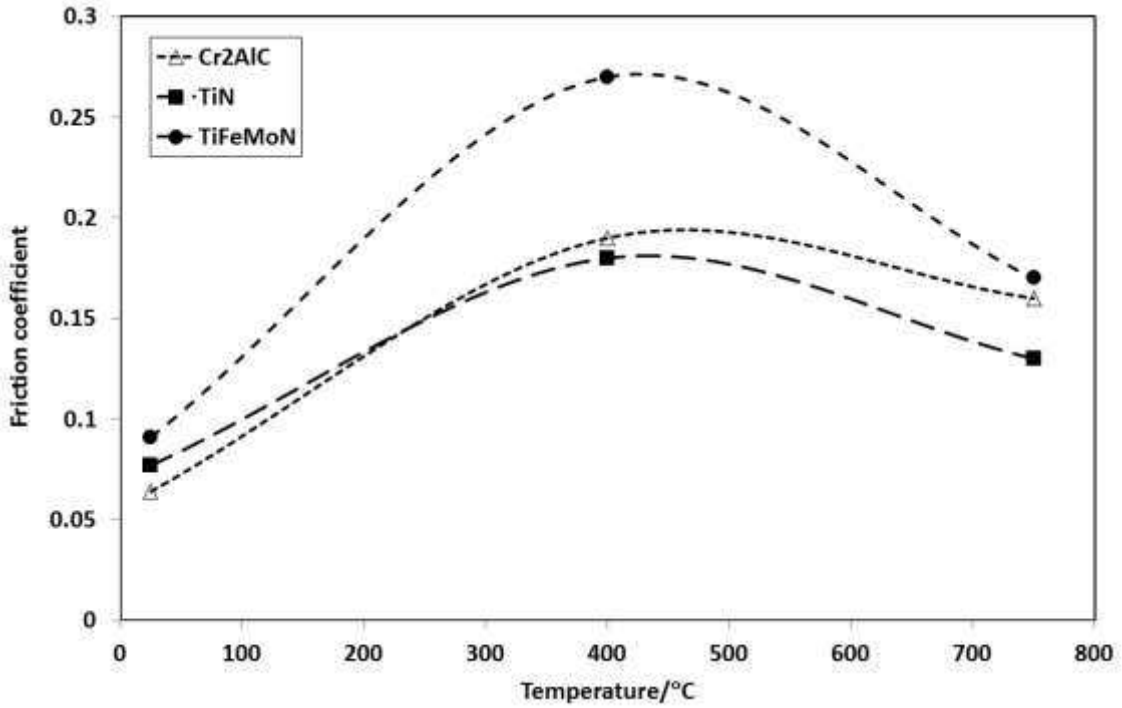

Figure 42: Variation in friction with temperature

In addition to the elevated temperature nanoindentation, scratch and friction testing several other tests can be performed at temperatures of 500 °C using commercial instrumentation (NanoTest) as illustrated by Table 5 below.

Table 5 nanomechanical tests at elevated temperature (after [132])

Technique	Applications	Maximum temperature/°C
Nanoindentation	Fuel cells	750
Micro-pillar compression	Si, Ni-based superalloys	665
Micro-cantilever bending	W and Si beams	770
Nano-friction	TiN-based coatings	750
Micro-scratch and wear	Tool coatings	600
Nano-impact	Tool coatings	500

Micropillar compression at elevated temperature is gaining popularity and is a relatively simple way of understanding how deformation mechanisms are affected by temperature [43, 133-134]. Korte and Clegg [43] have reported micropillar compression of $MgAl_2O_4$ spinel at 25, 200 and 400 ˚C, using a NanoTest

with dual active heating of the diamond flat punch and the spinel sample. At 25 ˚C only a small amount of plastic flow was observed before the pillars break. In contrast, pillars deformed entirely by plastic deformation at 200 and 400 ˚C. The measured yield stresses were consistent with those obtained previously by compressing larger pillars under high confining pressure, implying that the micropillar compression technique may be a useful way to assess plastic flow in brittle materials. Decreasing the sample size has reduced the temperature at which plasticity is normally observed by ~1500 ˚C

As well as mechanical property determination, micro cantilevers can be used for brittle to ductile transition studies. In this case micro cantilevers are produced with a notch at their fixed end to act as a stress raiser for crack initiation. The cantilevers are then loaded at a known distance from their fixed end until a pre-determined deformation has is reached. Individual cantilevers are tested of the relevant temperature range until the transition from a ductile to brittle response is observed.

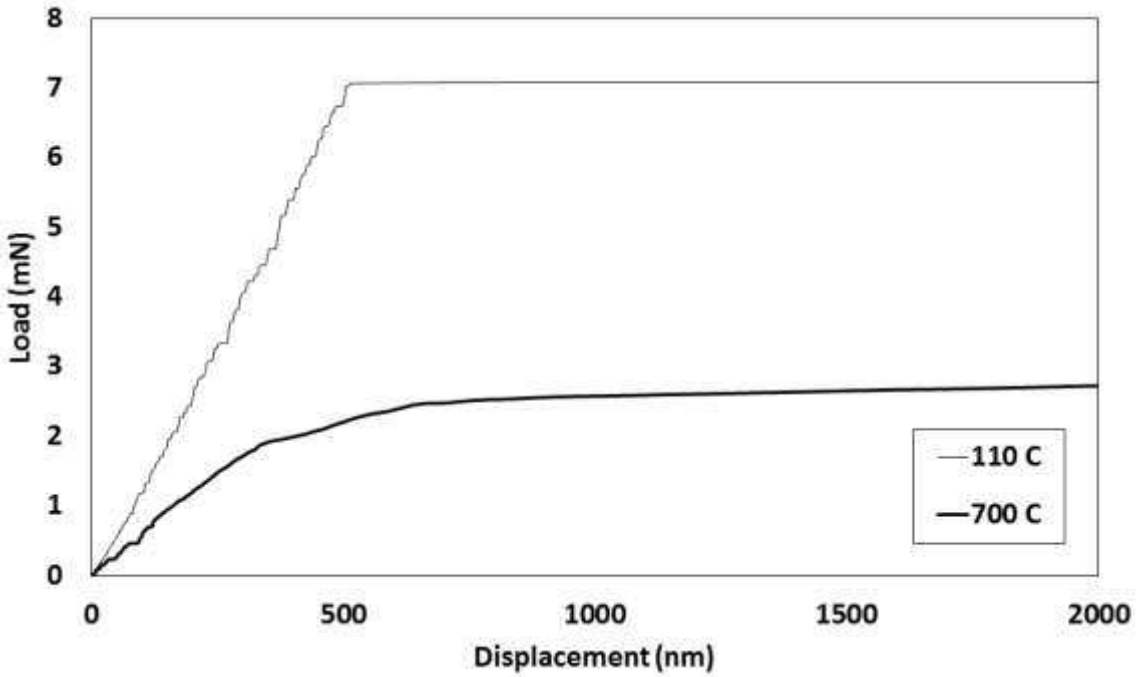

Figure 43: Load-displacement traces from bend tests on silicon cantilevers *at 110 and 700 ˚C*.

At 110 ˚C the loading segment is seen to be essentially linear until brittle fracture occurs at about 0.5 µm displacement. At 700 ˚C the loading is initially linear then the material starts to flow plastically, no fracture occurs. In both cases the experiments were configured to stop applying load once a displacement of 2 µm was reached.

6.4.2 Sub-ambient temperature nanoindentation, nano-scratch and nano-wear testing

When testing mechanical properties below ambient temperature it is just as important that sample and indenter are at the same temperature as it is in elevated temperature testing. Using dual cooling control Chen et al. reported the development of a prototype cold stage accessory for the NanoTest demonstrating its ability to investigate the local mechanical properties and the creep behavior of atactic polypropylene down to -30ºC [135]. The cooling system used incorporated a purging chamber to eliminate condensation during cooling and two Peltier coolers to achieve the isothermal contact. The sub-ambient test capability has also been used to investigate the nanotribological and nanomechanical properties of a functionally graded a-C:H(Ti)/TiCN/TiN/Ti coating from 25 ºC to –30 ºC [136]. The coating failed by cracking and spallation in the room temperature nano-scratch tests. Analysis of fracture sections showed these failures originated from, or close to, the interface between the top a-C:H(Ti) layer and the TiCN layer. Interestingly, decreasing the test temperature improved its properties. Testing at 0 ºC resulted in an increase in H, H/E_r and H^3/E_r^2, consistent with improved crack resistance and wear resistance with further modest improvements when the test temperature was reduced to -30 ºC.

6.4.3 High temperature nano-impact testing

Elevated temperature nano-impact tests have been performed for hard coatings and polymeric materials. Fracture probability data from nano-impact tests at 500 °C on TiAlN and AlTiN coated WC-Co inserts have been shown to correlate with the plasticity index and cutting tool life data [137]. The nano-impact test is sensitive to changes in the viscoelastic behavior of polymers as the test temperature is altered relative to the glass transition temperature. Constantinides and co-workers performed nano-impact testing on PS and PC from well below to well above their glass transition temperature ranges (testing from 20-180 °C) [138]. They found that the coefficient of restitution e decreased only very slightly over the temperature range 0.2-1.0 T/T_g for both polymers. However, for temperatures exceeding the glass transition temperature (i.e. $T/T_g>1$) the capacity of the materials to dissipate the energy of impact greatly (e decreases) increases

7. Summary and Outlook

Technological developments over last few decades have introduced new and powerful techniques into the field of nanomechanical testing of materials enabling the scale of experiments to be drastically decreased in terms of applied loads, relative displacements and contact pressures. Improved resolution, calibration and efficiency of existing techniques and development of new tools have allowed highly localised and accurate mechanical property information to be obtained.

Small scale tribological experiments bring new opportunities to investigate the interaction between surfaces and help to build fundamental understanding of friction, lubrication and wear of materials at the single asperity contact. This type of experiments requires specific, high resolution equipment and methods with good stability and ultra-low drift. The range of available nanomechanical testing techniques has drastically expanded beyond simple nanoindentation, including more complex mechanical testing scenarios including nano-scratch and nano-wear experiments. This has been driven by novel materials development and new application challenges but also by further expansion of commercial testing platforms capability.

As a result of expanded nanomechanical testing landscape, novel applications and methods have emerged. This includes improved tribological techniques as experiments at smaller length scales allow tribologists to build fundamental understanding of frictional processes. Accelerated wear-testing and thin-film applications small scale fretting experiments are some of these areas as discussed earlier in this chapter.

Future challenges for nanomechanical testing require experiments in more severe test environments, including extreme low and high temperatures, various liquids, vacuum conditions and ability to handle increased energy densities. There will be also a constant pressure on equipment manufacturers to innovate with novel solutions allowing closer simulations of the real contact conditions in applications like MEMS and responding adequately to evolving miniaturisation of mechanical systems and emerging areas such as bio-engineering. Improved integration of measurement data obtained from mechanical testing seems to be increasingly a key part in providing reliable inputs for predictive surface damage models. Enhanced numerical models based on reliable mechanical data should not only allow better analysis of tribological experiments but also to forward simulate such tests and provide hints for better component life-time predictions.

8. References

1. ISO 14577: Metallic Materials – Instrumented Indentation Test for Hardness and Materials Parameters, Part 4 - Test Method for metallic and non-metallic coatings.
2. Fischer-Cripps, A.J. (2011) Nanoindentation 3rd Edition (Springer, USA).
3. Fischer-Cripps, A.J. (2000) Introduction to contact mechanics (Springer, USA).
4. Beake, B.D., Bell, G.A., Goodes, S.R., Pickford N.J. and Smith, J.F. (2010) Improved nanomechanical test techniques for surface engineered materials, Surf. Eng., 26, 37.
5. Chudoba, T., (2006) Nanostructured coatings Cavaleiro, A. and De Hosson, J.Th.M. eds. Chapter 6, "Measurement of hardness and Young's modulus of coatings by nanoindentation" (Springer, New York) pp216-260.
6. Kermouche, G., Barthel, E., Vamdembroucq, D. and Dubujet, Ph. (2008) Mechanical modelling of indentation-induced densification in amorphous silica, Acta Mater., 56, 3222-3228.
7. Beake B.D. and Smith J.F. (2002) High-temperature nanoindentation testing of fused silica and other materials, Philos. Mag. A, 82, 2179-2186.

8. Chudoba, T. and Jennett, N.M., (2008) Higher accuracy analysis of instrumented indentation data obtained with pointed indenters, J. Phys. D: Appl. Phys., 41, 215407.
9. Morris, D.J., Myers, S.G. and Cook, R.F. (2004) Sharp probes of varying acuity: instrumented indentation and fracture behaviour, J. Mater. Res., 19, 165-175.
10. Gan, B. and Tin, S. (2010) Assessment of effectiveness of transition metal solutes in hardening of Ni solid solutions, Mater. Sci. Eng. A, 527, 6809-6815.
11. Chudoba, T. and Richter, F. (2001) Investigation of creep behaviour under load during indentation experiments and its influence on hardness and modulus results, Surf. Coat. Technol., 148, 191-198.
12. Young, T.J., Monclus, M.A., Burnett, T.L., Broughton, W.R., Ogin, S.L. and Smith, P.A. (2011) The use of PeakForceTM quantitative nanomechanical mapping AFM-based method for high-resolution Young's modulus measurement of polymers, Meas. Sci. Technol., 22, 125703.
13. Dub, S.N., Lim, Y.Y. and Chaudhri, M.M. (2010) Nanohardness of high purity Cu (111) single crystals: the effect of indenter load and prior plastic strain, J. Appl. Phys., 107, 043510.
14. Schwarzer, N., Duong, Q.-H., Bierwisch, N. et al (2011) Optimisation of the scratch test for specific coating designs, Surface Coat. Technol., 206.
15. Van Vliet, K.J., Prchlik, L. and Smith, J.F. (2004) Direct measurement of indentation frame compliance, J. Mater. Res., 19, 325-331.
16. Moseson, A.J., Basu, S. and Barsoum, M.W. (2008) Determination of the effective zero point for spherical nanoindentation, J. Mater. Res., 23, 204-209.
17. Chiang, C.-J., Bull, S.J., Winscom, C. and Monkman, A. (2010) A nano-indentation study of the reduced elastic modulus of Alq3 and NPB thin-film used in OLED devices, Organic Electronics, 11, 450-455.
18. Juliano T, Gogotsi Y and Domnich V (2003) J. Mater. Res. 18, 1192
19. Lu, C., Mai, Y.-W., Tam, P.L. and Shen, Y.G. (2007) Nanoindentation-induced elastic-plastic transition and size effect in α-Al2O3(0001), Philos. Mag. Lett., 87, 409-415.
20. Nix, W.D. and Gao, H. (1998) J. Mech. Phys. Solids, 46, 411.
21. Qiao, X.G., Starink, M.J. and Gao N., (2010) The influence of indenter tip rounding on the indentation size effect, Acta Mater., 58, 3690-3700.
22. Milman, Yu.V., Golubenko, A.A. and Dub, S.N. (2011) Indentation size effect in nanohardness, Acta Mater., 59, 7480-7487.
23. Cheng, Y.-T. and Cheng, C.-M., (1998) Relationships between hardness, elastic modulus, and the work of indentation. Appl. Phys. Lett., 73, 614.
24. Cheng, Y.-T. and Cheng, C.-M. (2004) Mater. Sci. Eng. R, 44, 91.
25. Greenwood, J. and Williamson, J. (1960) Proc. Royal Soc. A, 295, 300.
26. Beake, B.D., Fox-Rabinovich, G.S., Veldhuis S.C. and Goodes, S.R. (2009) Coating optimisation for high-speed machining with advanced nanomechanical test methods, Surf. Coat. Technol. 203, 1919-1925.
27. Beake, B.D, Goodes, S.R., Smith, J.F., Fox-Rabinovich G.S. and Veldhuis, S.C. (2010) Using nanomechanics to optimise coatings for cutting tools in Handbook of Nanostructured Thin Films and Coatings, Mechanical Properties, Chapter 6, pp205-244, Ed. S Zhang, CRC Press.
28. Leyland, A. and Matthews, A. (2000) On the significance of the H/E ratio in wear control: a nanocomposite coating approach to optimised tribological behaviour Wear, 246, 1.
29. Leyland, A. and Matthews, A. (2004) Design criteria for wear-resistant nanostructured and glassy-metal coatings. Surf. Coat. Technol., 177-178, 317.
30. Beake, B.D., Vishnyakov, V.M., Valizadeh, R. and Colligon, J.S. (2006) Influence of mechanical properties on the nanoscratch behaviour of hard nanocomposite TiN/Si_3N_4 coatings on Si. J. Phys. D: Appl. Phys., 39, 1392.
31. Bull, S.J. (2006) Using work of indentation to predict erosion behaviour in bulk materials and coatings J. Phys. D: Appl. Phys., 39, 1624.
32. Beake, B.D., Vishnyakov V.M. and Colligon J.S. (2011) Nano-impact testing of TiFeN and TiFeMoN films for dynamic toughness evaluation, J. Phys. D: Appl. Phys., 44, 085301.
33. Korunsky, A.M. and Constantinescu, A. (2006) Work of indentation approach to the analysis of hardness and modulus of thin coatings, Mater. Sci. Eng. A, 423, 28-35.
34. Veprek, S., Niederhofer, A., Moto, K., Bolom, T., Männling, H-D., Nesladek, P. et al. (2000) Composition, nanostructure and origin of the ultrahardness in nc-TiN/a-Si3N4 and nc-TiSi2 nanocomposites with Hv = 80 GPa to ≥105 GPa. Surf. Coat. Technol., 133-134, 152-159.

35. Fischer-Cripps, A.C., Bull, S.J. and Schwarzer, N. (2012) Critical review of claims for ultra-hardness in nanocomposite coatings, Philos. Mag., 92, 1601-1630.
36. Cordill M.J., Lund, M.S., Parker, J., Leighton, C., Nair, A.K., Farkas, D., Moody, N.R. and Gerberich, W.W. (2009) The nano-jackhammer effect in probing near-surface mechanical properties Int. J. Plasticity, 25, 2045-2058.
37. Cook, R.F. and Pharr, G.H. (1990) Direct observation and analysis of indentation cracking in glasses and ceramics, J. Am. Ceram. Soc., 73, 787.
38. Chen, J. (2012) Indentation-based methods to assess fracture toughness for thin coatings, J. Phys. D: Appl. Phys., 45, 203001.
39. Anstis, G.R., Chantikul, P., Lawn, B.R. and Marshall, D.B. (1981) A critical evaluation of indentation techniques for measuring fracture toughness: I. Direct crack measurements, J. Am. Ceram. Soc., 64, 533.
40. Chen, J. and Bull, S.J. (2007) Indentation fracture and toughness assessment for thin optical coatings on glass, J. Phys. D: Appl. Phys., 40, 5401.
41. Uchic, M.D., Dimiduk, D.M., Florando, J.N. and Nix, W.D. (2004) Science, 305, 986.
42. Greer, J.R., Oliver, W.C. and Nix, W.D. (2005) Acta Mater. 53, 1821.
43. Korte, S.K., and Clegg, W.J. (2009) Micropillar compression of ceramics at elevated temperature, Scr. Mater., 60,807.
44. Jennett, N.M., Ghisleni, R. and Michler, J. (2009) Enhanced yield strength of materials: the thinness effect, Appl. Phys. Lett., 95, 123102.
45. Armstrong, D.E.J., Wilkinson A.J. and Roberts, S.G. (2009) Measuring anisotropy in Young's modulus of copper using microcantilever testing, J. Mater. Res., 24, 3268.
46. Rollin, M., Jouannigot, S., Lamon, J. and Pailler, R. (2009) Characterization of fibre/matrix interfaces in carbon/carbon composites, Composites Science and Technology, 69, 1442-1446.
47. Steinmann, PA., Tardy Y. and Hintermann, H.E. (1987) Thin Solid Films, 154, 333.
48. Beake, B.D., Ogwu A.A. and Wagner, T. (2006) Influence of experimental factors and film thickness on the measured critical load in the nanoscratch test, Mater. Sci. Eng. A 423 (2006) 70-73.
49. Beake B.D., Davies M.I., Liskiewicz T.W., Vishnyakov V.M., Goodes S.R., Nano-scratch, nanoindentation and fretting tests of 5–80nm ta-C films on Si(100), Wear, Available online 4 February 2013, 10.1016/j.wear.2013.01.073.
50. Wu, T.W. (1991) J. Mater. Res., 6, 407.
51. Beake, B.D., Vishnyakov, V.M. and Harris, A.J. (2006) Relationship between mechanical properties of thin nitride-based films and their behaviour in nano-scratch tests, Tribol. Int., 44 (2011) 468.
52. Klocke, F., Bouzakis, K.-D., Georgiadis, K., Geradis. S., Skordaris, G. and Pappa, M. (2011) Adhesive interlayers' effect on the entire structure strength of glass modling tools' Pt-Ir coatings by nano-tests determined, Surface Coat. Technol., 206, 1867-1872.
53. Beake, B.D., Shi B. and Sullivan, J.L. (2011) Nanoscratch and nanowear testing of TiN coatings on M42 steel, Tribology 5, 141-147.
54. Beake, B.D., Goodes, S.R. and Shi B. (2009) Nanomechanical and nanotribological testing of ultra-thin carbon-based and MoST films for increased MEMS durability, J. Phys. D: Appl. Phys., 42, 065301.
55. Beake B.D., Liskiewicz T.W., Smith J.F. (2011) Deformation of Si(100) in spherical contacts – Comparison of nano-fretting and nano-scratch tests with nano-indentation, Surf. & Coat. Technol. 206, 1921-1926.
56. B.D. Beake, S.P. Lau, (2005) Nanotribological and nanomechanical properties of 5-80 nm tetrahedral amorphous carbon films on silicon, Diam. Relat. Mater., 14, 1535-1542.
57. Shi, B., Sullivan, J.L. and Beake, B.D. (2008) An investigation into which factors control the nanotribological behaviour of thin sputtered carbon films J. Phys. D: Appl. Phys., 41, 045303.
58. Bull, S.J. and Rickerby, D.S. (1989) Thin Solid Films, 181, 545.
59. Beake, B.D. and Ranganathan, N. (2006) An investigation of the nanoindentation and nano/micro-tribological behaviour of monolayer, bilayer and trilayer coatings on cemented carbide, Mater. Sci. Eng. A 423, 46.
60. Collins J.A., Failure of Materials in Mechanical Design, New York, J.Wiley (1981).
61. Sato K., Stolarski T.A., Iida Y., The effect of magnetic field on fretting wear, Wear 241 (2000), p. 99-108.
62. Mohrbacher H., Celis J.-P., Roos J.R., Laboratory testing of displacement and load induced fretting, Tribology International 28 (1995), p. 269-278.

63. Halliday J.S., Hirst W., The fretting corrosion of mild steel, Proc. Roy. Soc. A 236 (1956), p. 411-425.
64. Vaessen G.H.G., Commissaris C.P.L., De Gee A.W.J., Proc. Inst. Mech. Eng. 183, London (1968-1969), p. 125.
65. Ohmae N., Tzukizoe T., The effect of slip amplitude on fretting, Wear 27 (1974), p. 281-293.
66. Gordelier S.C., Chivers T.C., A literature review of palliatives for fretting fatigue, Wear 56 (1979), p. 177-190.
67. Gordelieen S.C., Stallings L., ASTM Spec. Tech. Publ. 780 (1982), p. 30-48.
68. Kennedy P.J., Stallings L., Petersen M.B., A study of surface damage at low amplitude slip, Proc. of Conf. "ASLE-ASME Lubrication Conf.", Hartford (1983).
69. Fouvry S., Kapsa Ph., Vincent L., Quantification of fretting damage, Wear 200 (1996), p. 186-205.
70. Williams J. and, Le H.: J. Phys. D., 2006, 39D, R201.
71. Drees D., Celis J.-P. and Achanta S., Friction of thin coatings on three length scales under reciprocating sliding, Surf. Coat. Technol., 2004, 188–189, p. 511–518.
72. Varenberg M., Etsion I., Halperin G., Nanoscale fretting wear study by scanning probe microscopy, Tribol. Lett., Vol. 18, No. 4, 2005, p. 493-498.
73. Yoon Y., Etsion I., Talke F.E., The evolution of fretting wear in a micro-spherical contact, Wear 270, 2011, p. 567-575.
74. Yu J.X., Qian L.M., Yu B.J., Zhou Z.R., Nanofretting behaviours of monocrystalline silicon (100) against diamond tips in atmosphere and vacuum, Wear 267, 2009, p. 322-329.
75. Yu J., Qian L., Yu B., Zhou Z., Nanofretting behaviour of monocrystallinr silicon (100) against SiO2 microsphere in vacuum, Tribol. Lett., Vol. 34, 2009, p. 31-40.
76. Chen L., Yang M., Yu J., Qian L., Zhou Z., Nanofretting behaviours of ultrathin DLC coating on Si(100) substrate, Wear 271, 2011, p. 1980-1986.
77. Wilson G.M., Smith J.F., Sullivan J.L., A nanotribological study of thin amorphous C and Cr doped amorphous C coatings, Wear 265, 2008, p. 1633-1641.
78. Wilson G.M., Smith J.F., Sullivan J.L.,A DOE nano-tribological study of thin amorphous carbon-based films, Tribol. Int. 42, 2009, p. 220-228.
79. Wilson G.M., Sullivan J.L., An investigation into the effect of film thickness on nanowear with amorphous carbon-based coatings, Wear 266, 2009, p. 1039-1043.
80. Achanta S., Drees D., Celis J.-P., Friction and nanowear of hard coatings in reciprocating sliding at milli-Newton loads, Wear 259, 2005, p. 719-729.
81. Achanta S., Drees D., Celis J.-P., Investigation of friction on hard homogeneous coatings during reciprocatings tests at micro-Newton normal forces, Wear 263, 2007, p. 1390-1396.
82. Weppelmann E.R., Field J.S., Swain M.V., Influence of spherical indentor radius on the indentation-induced transformation behavior of silicon, J. Mater. Sci. 30 (1995) 2455.
83. Bradby J.E., Williams J.S., Wong-Leung J., Swain M.V., Munroe P., Mechanical deformation in silicon by micro-indentation, J. Mater. Res. 16, 2001, p. 1500-1507.
84. Juliano T., Domnich V., Gogotsi Y., Examining pressure-induced phase transformations in silicon by spherical indentation and Raman spectroscopy: A statistical study, J. Mater. Res. 19, 2004, 3099-3108.
85. Chang L., Zhang L., Deformation mechanisms at pop-out in monocrystalline silicon under nanoindentation, Acta Mater. 57, 2009, p. 2148-2153.
86. Mitchell, A. and P. Shrotriya, Onset of nanoscale wear of metallic implant materials: Influence of surface residual stresses and contact loads. Wear, 2007. 263: p. 1117-1123.
87. Corbella C., Rubio-Roy M., Bertran E., Polo M.C., Pascual E., Andújar J.L., Low friction and protective diamond-like carbon coatings deposited by asymmetric bipolar pulsed plasma, Diamond and Related Materials 18, 2009, p. 1035-1038.
88. Liskiewicz T.W., Beake B.D., Smith J.F., In situ accelerated micro-wear – A new technique to fill the measurement gap, Surf. & Coat. Technol. 205, 2010, p. 1455-1459.
89. Ku I.S.Y., Reddyhoff T., Wayte R., Choo J.H., Holmes A. S., Spikes H.A., Lubrication of microelectromechanical devices using liquids of different viscosities, J. Tribol. 134 (2012) 012002-1.
90. Maboudian R., Ashhurst W.R., Carraro C., Self-assembled monolayers as anti-stiction coatings for MEMS: characterisation and recent developments, Sensors Actuators, 82, 2000, p. 219-223.
91. Smallwood S.A., Eapen K.C., Patton S.T., Zabinski J.S., Performance results of MEMS coated with a conformal DLC, Wear 260, 2006, p. 1179-1189.
92. Akita N., Konishi Y., Ogura S., Imamura M., Hu Y.H., Shi X., Comparison of deposition methods for ultra thin DLC overcoat film for MR head, Diamond Relat. Mater. 10, 2001, p. 1017-1023.

93. Chan C.Y., Lai K.H., Fung M.K., Wong W.K., Bello I., Huang R.F., Lee C.S., Lee S.T., Wong S.P., Deposition and properties of tetrahedral amorphous carbon films prepared on magnetic disks, J. Vac. Sci. Technol. A 19, 2001, p. 1606.
94. Wang F.C., Jin Z.M., McEwen H.M.J., Fisher J., Microscopic asperity contact and deformation of ultrahigh molecular weight polyethylene bearing surfaces, Proc. IMechE, Part H: J. Eng. In Med. 2003, 217, p. 477-490.
95. Raimondi M.T., Vena P., Pietrabissa R., Quantitative evaluation of the prosthetic head damage induced by microscopic third-body particles in total hip replacement, J. of Biomed. Mat. Res. Part B 58, 2001, p. 436-448.
96. Beake B.D., Liskiewicz T.W., Comparison of nano-fretting and nano-scratch tests on biomedical materials, Tribology International, Available online 24 August 2012, 10.1016/j.triboint.2012.08.007.
97. Fox-Rabinovich, G.S., Yamamoto, K., Beake, B.D., Kovalev, A.I., Aguirre, M.H., Veldhuis, S.C., Dosbaeva, G., Wainstein, D.L., Biksa, A., and Rashkovskiy, A.Y. (2010) Emergent behavior of nano-multilayered coatings during dry high speed machining of hardened tool steels Surf. Coat. Technol., 204, 3425.
98. Fox-Rabinovich, G.S., Beake, B.D., Veldhuis, S.C., Endrino, J.L., Parkinson, R., Shuster, L.S. and Migranov M.S. (2006) Impact of mechanical properties measured at room and elevated temperatures on wear resistance of cutting tools with TiAlN and AlCrN coatings Surf. Coat. Technol., 200, 5738.
99. Chen, J., Beake, B.D., Wellman, R., Nicholls, J.R. and Dong, H. (2012) An investigation into the correlation between nano-impact resistance and erosion performance of EB-PVD thermal barrier coatings on thermal ageing, Surf. Coat. Technol., 206, 4992–4998
100. Trelewicz, J.R. and Schuh, C.A. (2008) The Hall–Petch breakdown at high strain rates: Optimizing nanocrystalline grain size for impact applications, Appl. Phys. Lett. 93, 171916.
101. Quantitative Impact Testing of Energy Dissipation at Surfaces, Constantinides, G., Tweedie, C.A., Savva, N., Smith, J.F. and Van Vliet, K.J. Experimental Mechanics DOI 10.1007/s11340-008-9198-1
102. Jennett, N.M. and Nunn, J. (2010) High resolution measurement of dynamic (nano) indentation impact energy: a step towards the determination of indentation fracture resistance, Philos. Mag.
103. Beake, B.D. and Smith, J.F. (2004) Nano-impact testing – an effective tool for assessing the resistance of advanced wear-resistant coatings to fatigue failure and delamination, Surf. Coat. Technol., 188-189C, 594.
104. Bouzakis, K.-D., Gerardis, S., Skordaris, G. and Bouzakis, E. (2011) Nano-impact tests on a TiAlN PVD coating and correlation between experimental and FEM results, Surf. Coat. Technol., 206, 1936-1940.
105. Faisal, N.H., Ahmed, R. and Fu, Y. (2011) Nano-impact testing and failure mechanism of solar panel DLC film, Proc. ATMC 2011, KACST, Saudi Arabia, 2011, 36-44.
106. Faisal, N.H., Ahmed, R. and Fu, Y. (2012) Nano-impact (fatigue) characterisation of as-deposited amorphous nitinol thin film, Coatings, 2, 195-209.
107. Bouzakis, K.-D., Skordaris, G., Bouzakis, E., Tsouknidas, A., Makrimallakis, S. et al, (2011) Optimisation of wet micro-blasting on PVD films with various grain materials for improving the coated tools' cutting performance, CIRP Annals – Manufacturing Technology, 60, 587-590.
108. Bouzakis, K.-D., Klocke, F., Skordaris, G., Bouzakis, E., Geradis. S. et al. (2011) Influence of dry micro-blasting grain quality on wear behaviour of TiAlN coated tools, Wear, 271, 783-791.
109. Bouzakis, K.-D., Bouzakis, E., Skordaris, G., Makrimallakis, S., Tsouknidas, A. et al, (2011) Effect of PVD films wet micro-blasting by various Al2O3 grain sizes on the wear behaviour of coated tools, Surface Coat. Technol., 205, S128-S132.
110. Chen, J., Ji, R., Khan, R.H.U., Li, X., Beake B.D. and Dong, H. (2011) Effects of mechanical properties and layer structure on the cyclic loading of TiN-based coatings, Surf. Coat. Technol., 206, 522.
111. Altaf, K., Ashcroft, I.A. and Hague, R. (2012) Modelling the effect of moisture on the depth sensing indentation response of a stereolithography polymer, Comput. Mater. Sci., 52. 112-117
112. Bushby, A.J., Ferguson, V.L. and Boyde, A. (2004) Nanoindentation of bone: comparison of specimens tested in liquid and embedded in polymethylmethacrylate, J. Mater. Res., 19, 249-259.
113. Bell, G.A., Bielinski, D.M. and Beake, B.D. (2008) Influence of water on the nanoindentation creep response of nylon 6, J. Appl. Polym. Sci., 107, 577-582.
114. Constantinides G., Kalcioglu Z.I., McFarland M. et al. (2008) Probing mechanical properties of fully hydrated gels and biological tissues, J. Biomechanics, 41, 3285-3289.

115. Harris, A.J., Beake, B.D. and Davies M.I. (2013) in preparation.
116. Schmidt, D.J., Cebeci. F.C., Kalcioglu, Z.I. et al. (2009) Electrochemically controlled swelling and mechanical properties of a polymer nanocomposite, ACS Nano, 3, 2207-2216.
117. Sun, D., Wharton, J.A. and Wood, R.J.K. (2009) Micro-abrasion mechanisms of cast CoCrMo in simulated body fluids, Wear, 267, 1845-1855.
118. Kalcioglu, Z.I., Qu, M., Strawhecker, K.E., Shazly, T., Edelman, E., VanLandingham, M.R., Smith, J.F. and Van Vliet, K.J. (2010) Dynamic impact indentation of hydrated biological tissues and tissue surrogate gels, Philos. Mag., 91, 1339-1355.
119. Everitt, N.M., Davies, M.J. and Smith, J.F. (2011) High temperature nanoindentation – the importance of isothermal contact, Philos. Mag., 91, 1221-1244.
120. Tang, F. and Zhang, L.C. (2011) On the reliability of nanoindentation on Si wafer at elevated temperatures, Adv. Mater. Res., 325, 684.
121. Zarnetta, R., Kneip, S., Somsen, Ch. And Ludwig, A. (2011) High-throughput characterization of mechanical properties of Ti-Ni-Cu shape memory thin films at elevated temperature, Mater. Sci. Eng. A, 528, 6552-6557.
122. Schuh, C.A., Packard, C.E. and Lund, A.C. (2006) Nanoindentation and contact-mode imaging at high temperatures, J. Mater. Res., 21, 725-736.
123. Trenkle, J.C., Packard, C.E. and Schuh, C.A. (2010) Hot nanoindentation in inert environments, Rev. Sci. Instr., 81, 073901.
124. Franke, O., Trenkle, J.C. and Schuh, C.A. (2010) Temperature dependence of the indentation size effect, J. Mater. Res., 25, 1225-1229.
125. Smith, J.F. and Zheng, S. (2000) High temperature nanoscale mechanical property measurements, Surf. Eng., 6, 143.
126. UK Patent GB2478134B and Int Pat App WO2011/104529.
127. Fox-Rabinovich, G.S., Endrino, J.L., Beake, B.D., Kovalev, A.I., Veldhuis, S.C., Ning, L., Fotaine F. and Gray, A. (2006) Impact of annealing on the microstructure, properties, and cutting performance of AlTiN coating, Surf. Coat. Technol., 201, 3524.
128. Fox-Rabinovich, G.S. Endrino, J.L. Beake, B.D. Aguirre, M.H. Veldhuis, S.C Quinto, D.H., Bauer, C.E., Kovalev A.I. and Gray, A. (2008) Effect of annealing below 900C on structure, properties and tool life of an AlTiN coating under various cutting conditions, Surf Coat Technol 202, 2985.
129. Bouzakis, K.-D., Pappa, M., Geradis. S., Skordaris, G. and Bouzakis, E. (2012) PVD coatings' strength at various temperatures by nanoindentations and FEM calculations determined, Tribology in Industry, 34, 29-35.
130. Milhans, J., Li, D.S., Khaleel, M., Sun, X. Al-Haik, M.S., Harris, A. and Garmenstani, H. (2011) Mechanical properties of solid oxide fuel cell glass-ceramic seal at high temperatures, J. Power Sources, 196, 5599.
131. He, B., Ghosh, G., Chung, Y.-W. and Wang, Q. (2010) Effect of Melting and Microstructure on the Microscale Friction of Silver–Bismuth Alloys Tribol. Lett., 38, 275-282.
132. Smith, J.F., Vishnyakov, V.M., Davies, M.I. and Beake, B.D. (2013) Nanoscale Friction Measurements Up to 750 C, Tribol. Lett. DOI 10.1007/s11249-013-0102-5
133. Korte, S.K., Banard, J.S., Stearn, R.J. and Clegg, W.J. (2011) Deformation of silicon, insights from microcompression testing at 25-500 °C, Int. J. Plasticity, 27, 1853.
134. Korte, S.K., Stearn, R.J., Wheeler, J.M. and Clegg, W.J. (2012) High temperature microcompression and nanoindentation in vacuum, J. Mater. Res. 27, 167-176.
135. Chen, J., Bell, G.A., Dong, H., Smith, J.F. and Beake, B.D. (2010) A study of low temperature mechanical properties and creep behaviour of polypropylene using a new sub-ambient temperature nanoindentation test platform, J. Phys. D: Appl. Phys., 43, 425404.
136. Chen, J. Bell, G.A., Beake B.D. and Dong, H. (2011) Low Temperature Nano-Tribological Study on a Functionally Graded Tribological Coating Using Nanoscratch Tests, Tribol. Lett., 43, 351.
137. Beake, B.D., Smith, J.F., Gray, A, Fox-Rabinovich, G.S., Veldhuis, S.C. and Endrino, J.L., (2007) Investigating the correlation between nano-impact fracture resistance and hardness/modulus ratio from nanoindentation at 25-500 °C and the fracture resistance and lifetime of cutting tools with Ti1-xAlxN (x=0.5 and 0.67) PVD coatings in milling operations Surf. Coat. Technol., 201, 4585.
138. Quantifying deformation and energy dissipation of polymeric surfaces under localized impact Constantinides, G., Tweedie, C.A., Holbrook, D.M., Barragan, P., Smith, J.F. and Van Vliet, K.J. (2008) Mater. Sci. Eng. A 489, 403–412.

List of figures

1. Contact geometries
2. Environmental conditions (adapt from visco? Or use impact/temp)
3. A typical nanoindentation curve
4. (a) load history for a soft metal (b) Aluminium example
5. W – compliance
6. W - H vs depth, maybe with E insert
7. DLC on Si
8. 400 indentations into Ti6Al4V alloy programmed in a single experiment as a 20 x 20 grid, pitch 20 μm
9. Micro-mapping around inclusions of Al7Cu2Fe intermetallics in a 7000 series Al alloy
10. microcompression, l-d trace
11. SEM of cantilever
12. 3D SPM image
13. AH – fibre-push-out x2
14. Si loading comparison
15. Klocke bar chart
16. Lc vs thickness 5-80 nm
17. redraw 2N comp from 2006 paper
18. friction vs. cycles
19. Fretting test configurations
20. Three basic fretting modes with representative displacement tracks
21. Definition of sliding ratio "e" and identification of transition between fretting regime and reciprocating sliding motion (contact sphere/plane)
22. Measurement gap between conventional tribometers and AFM techniques as function of normal force, displacement amplitude and contact pressure
23. Comparison of loading curves in small scale (a) indentation and scratch, (b) indentation and fretting experiments. Test configuration: 4.6□m sphero-conical diamond indenter against Si(100)
24. On-load probe depth evolution as a function of 30mN small scale fretting test. [Adapted from 39].
25. SEM images of small scale fretting scars …loads… materials.
26. Ti6Al4V dynamic hardness
27. after SCT 2009
28. after Jennett/Nunn
29. Saudi impact
30. Bouzakis Klocke impact
31. TBC impact
32. NT liquid cell
33. Humidity nylon
34. Jilin
35. Thermal mismatch
36. HS schematic
37. Si at 500 and 600C
38. Si loading rate vs time
39. HT hardness AlTiN
40. GA creep
41. E vs T for SOFC
42. 750C friction
43. Si at 110 and 700C